Durham E-Theses

Photonic Spectroscopy in Astronomy

HARRIS, ROBERT,JAMES

How to cite:

HARRIS, ROBERT,JAMES (2015) *Photonic Spectroscopy in Astronomy*, Durham theses, Durham University. Available at Durham E-Theses Online: http://etheses.dur.ac.uk/10975/

Use policy

Photonic Spectroscopy in Astronomy

Robert J. Harris

A Thesis presented for the degree of

Doctor of Philosophy

Centre for Advanced Instrumentation
Department of Physics
Durham University
England

September 2014

Abstract

This thesis investigates photonic spectroscopy and its use in astronomy.

In chapter two the theory associated with both astronomical spectroscopy and photonic spectroscopy is shown. The convergence of the two in the field of astrophotonics is discussed along with existing work in the field.

In chapter three models of the Integrated Photonic Spectrograph are created and compared like-for-like with existing instruments. The results suggest that the Integrated Photonic Spectrograph will be similar to existing instruments in terms of size and will require more detector pixels for a full instrument.

In chapter four the modelling is extended, examining the areas where photonic spectroscopy could show advatanges over conventional instrumentation. This is done by varying spectral resolution, telescope diameter, seeing and number of objects sampled. The results show that the Integrated Photonic Spectrograph will perform best when the telescope is close to the diffraction-limit, both in terms of size and number of detector pixels required. Science cases are presented for these areas.

In chapter five different concepts for a redesigned Integrated Photonic Spectrograph are presented and the advantages and disadvatanges of the variations are commented upon. The two that are chosen for development require the telescope Point Spread Function to be reformatted to a long slit.

This device, which we have named the photonic-dicer is presented in chapter six. Its design, manufacture and testing is discussed both in the laboratory and on sky in conjunction with the CANARY adaptive optics system.

Finally chapter seven presents our concluding remarks and discussions for future work.

Declaration

The work in this thesis is based on research carried out at the Centre for Advanced Instrumentation, the Department of Physics, University of Durham, England. No part of this thesis has been submitted elsewhere for any other degree or qualification and it is the sole work of the author unless referenced to the contrary in the text.

Publications

Thomson, R. R., **Harris, R. J.** Birks, T. A., Brown, G., Allington-Smith, J. R. and Bland-Hawthorn, J. (2012). Ultrafast laser inscription of a 121-waveguide fan-out for astrophotonics. *Optics Letters*, 37(12): 2331-2333.

Harris, R. J. and Allington-Smith J. R. (2012). Modelling the application of integrated photonic spectrographs to astronomy. *Ground-based and Airborne Instrumentation for Astronomy IV 8446: Amsterdam*, Proc. SPIE, 84467J.

Harris, R. J and Allington-Smith, J. R. (2013). Applications of Integrated Photonic Spectrographs in astronomy. *Monthly Notices of the Royal Astronomical Society* 428(4): 3139.

Harris, R. J., Allington-Smith, J. R., MacLachlan, D., and Thomson, R. R. (2014, July). A comparison of concepts for a photonic spectrograph. In SPIE Astronomical Telescopes+ Instrumentation (pp. 91474C-91474C). International Society for Optics and Photonics.

MacLachlan, D. G., **Harris, R.J.**, Choudhury, D., Arriola, A., Brown, G., Allington-Smith, J., and Thomson, R. R. (2014, July). Development of integrated photonic-dicers for reformatting the point-spread-function of a telescope. In SPIE Astronomical Telescopes+ Instrumentation (pp. 91511W-91511W). International Society for Optics and Photonics.

Harris, R. J., MacLachlan, D. G., Choudhury, D., Morris, T. J., Gendron, E., Basden, A. G., Brown G., Allington-Smith, J. R., and Thomson, R. R. (2014). Photonic spatial reformatting of stellar light for diffraction-limited spectroscopy. *in prep*

Acknowledgements

Sometimes I feel my thanks page should be the longest part of my thesis and for anybody I end up missing I am truly sorry. My supervisor Jeremy Allington-Smith for many long hours of meetings, frequent sanity checks, patience in repeating advice (I really should learn to listen) and many many re-drafts of all of my writing. Robert Thomson for advice, help and many discussions about my crazy ideas. Tim Morris who not only gave me the chance to use CANARY, but spent many hours in GHRIL trying to teach me how to align optics and use them. David MacLachlan, without whom none of chapter 6 would have happened, whilst I intend never to work as hard as last summer again, I will miss Bonnie time. Adi for putting up with David and I. Graham Murray, Chris Saunter and Tim Butterly who have tried repeatedly to give me good advice throughout my PhD and have been relaxed no matter what the results. To all of the CANARY team (particularly Eric and Ali) for allowing us to use their system. To the various inhabitants of the PhD and postdoc offices, I wouldn't have made it through without you all. My friends and family for their constant support and finally to anybody I've missed, please forgive me.

Contents

List of Figures

List of Tables

AWG   Arrayed Waveguide Grating

AO   Adaptive Optics

PL   photonic lantern

SM   Single Mode

MM   Multi Mode

FPZ   Free Propagation Zone

ELT   Extremely Large Telescope

AW   Arrayed Waveguides

ULI   Ultrafast Laser Inscription

AAT   Anglo-Australian Telescope

AAO   Australian Astronomical Observatory

FSR   Free Spectral Range

IFU   Integral Field Unit

IFS   Integral Field Spectrscopy

PSF   Point Spread Function

IPS   Integrated Photonic Spectrograph

MOS   Multi Object Spectrograph

DFS   Diverse Field Spectroscopy

FOV   Field of View

FWHM Full Width Half Maximum

PEG Phased Echelle Grating

ND Neutral Density

TE Transverse Electrical

TM Transverse Magnetic

CCD Charge-Coupled Device

InGaAs Indium Gallium Arsenide

WHT William Herschel Telescope

FBG Fibre Bragg Grating

Chapter 1

Introduction

1.1 Motivation

For a given set of parameters the size of a seeing limited astronomical spectrograph is related to the diameter of the telescope it sits behind [1]. As we enter the era of the Extremely Large Telescope (ELT), difficulties in manufacture are leading to spiralling costs and forcing instrument designers to look at alternatives to conventional designs. At the same time the accuracies demanded of the instruments are becoming more difficult to achieve.

One proposed alternative is the use of (photonic) technologies developed for the telecommunications industry. These technologies can be used to modularise the instruments through image slicing, potentially reducing costs and increasing stability. This thesis will compare these technologies to existing instrumentation and techniques and examine their use within astronomy, through both modelling and experiment.

1.1.1   Spectra and Spectroscopy

Whilst spectra have been know about for millennia and are a common occurrence in everyday life, from the rainbow after the storm, to the multicoloured light reflecting from a DVD, the analysis of them is relatively recent. The name spectrum first appeared in 1666 when Newton allowed sunlight from a small round hole to pass through a triangular prism. He observed that this white light was split into its constituent colours, producing what Newton thought was an infinity of colours. He published this result in his book [2], calling the colours in the white light 'spectrum', meaning window to the soul.

In 1800, William Herschell discovered different amounts of heat were produced when he used coloured filters to block white light. To test this further he used thermometers to measure the temperature at different points in the spectrum, including some outside the range of the visible light. He found that the temperature rose in these thermometers as well when compared to control thermometers in the room. This was the discovery of infra-red light, the first example of light with a wavelength beyond the range of human vision.

The two experiments described above used refraction through a prism to split the light. This provides a relatively low dispersion unless the prism is large, so modern spectroscopy usually uses a diffraction grating to disperse the light more widely.

Diffraction is a consequence of the wave nature of light and was discovered shortly after Newton's early work by James Gregory (the inventor of the Gregorian telescope). He used natural objects such as bird feathers in place of a prism. Their fine structure caused interference in the light. However, it was another hundred years (1785) before the first man-made diffraction grating was produced by David Rittenhouse. He strung hairs between two screws, creating the same fine structure as bird feathers had.

It was not until Joseph von Fraunhoffer's invention of the spectroscope that quantative spectroscopy was born. He used a wire diffraction grating, increasing the spectral resolution of his spectroscope and allowing him to observe absorption lines of the solar spectra. These observations were the beginnings of solar spectroscopy and paved the way for modern astronomical spectroscopy.

1.1.2 Astronomical spectroscopy

After studying the solar spectrum Fraunhoffer placed his spectrograph behind a telescope and observed the Moon, Venus and Mars, along with Betelegeuse and other bright stars. In particular he examined the spectra of several stars of the same brightness. He found these spectra contained different absorption and emission lines. For the first time this showed that not all stars were the same, beginning the system of spectral classification.

Spectroscopy now occupies a major place in astronomy and is regularly used to classify objects of all sizes within the universe. This is due to its ability to identify temperatures, component elements, densities and the velocities at which objects are moving. It has been key in many discoveries including the identification of Helium (named after the Greek personification of the Sun, Helios) on the Sun and the first planet around another Sun-like star.

Whilst spectroscopy is a mainstay of astronomy it is reaching its limit on modern telescopes. As telescopes increase in size the image scale increases. As a result the instruments behind them also have to increase in size. In addition, these larger telescopes are far more costly to build, so fewer are built. This results in a hard limit on the amount of time that can be spent observing and so each instrument is required to observe more objects and to perform different types of observations (sometimes simultaneously). Combined this means the associated instruments become more complex, more difficult to design and more

costly to build.

Instrument designers have several solutions to these problems. Firstly, flecture in the telescope can be corrected by Active Optics and turbulence in the atmosphere can be corrected by Adaptive Optics (AO). This sharpens up the image produced by the telescope, reducing the size of the input to the spectrograph. Secondly, the input can be split up into many smaller sections (image slicing). These sections can then be sent to many replicated instruments, each of which is individually smaller than an unsliced instrument.

Despite these innovations, instruments are still becoming more complex and the ones on the next generation of telescopes will cost many millions of Euros to design and build. At the same time the current generation of telescopes are facing an uncertain future. Whilst still useful in terms of the science they produce, they are facing funding cuts to pay for the newer, larger telescopes. As such any new instrumentation needs to be designed to be cheaper and easier to replace, whilst still producing the same, or better science.

1.1.3 Photonics

In this thesis we shall use the term photonics to describe anything that has been developed, or has branched from, developments for the telecommunications world. This area has developed rapidly since the invention of the laser and fibre optic cable fifty years ago. The combination of laser signals in fibres allowed larger amounts of data to be transmitted than using copper cables, although routing signals still had to be done electronically. In more recent years this has been overcome by the invention of devices that can easily transfer signals between the two systems. This is done either in the time or wavelength domain. Wavelength has the advantage that no moving parts are required.

Since their inception, billions of dollars have been spent on research and

development of telecommunications devices. This has lead to robust modular devices that are easily integrated into the networks. They are also manufactured in great numbers in order to satisfy the ever increasing demands upon the telecoms world.

1.1.4 Astrophotonics

In the last ten years interest has been growing in using the small integrated components developed for the telecommunications industry. These devices have potential in many areas, with benefits including reduction of size and cost, efficient OH suppression and low mode noise fibres being proposed. Devices have been proposed in many different areas including spectrographs [3, 4, 5, 6]), interferometers, [7], wavelength filters [8, 9], chronographs [10] and spatial reformatters [11, 12, 13]. In 2003 this new field was christened Astrophotonics.

Development of photonic dispersive spectrometers for astronomy was first proposed in 1995 [14], though it was not until a decade later that the technology was deemed to be useful to astronomy [15]. This paper investigated the use of Phased Echelle Grating (PEG)s and AWGs for astronomical instruments and concluded they had potential use in astronomy. Whilst the PEG was later abandoned, the AWG went on to be tested.

The first devices were tested by groups in Australia on the Anglo-Australian Telescope (AAT) [3, 5]. They were not full instruments in their own right, as they used conventional instruments to produce complete spectra. This drove up the size and reduced the efficiency. As such whilst they worked as demonstrators it was not shown if they could compete with conventional instrumentation.

1.2   Synopsis

This thesis aims to describe and characterise the place of photonic spectroscopy within astronomy. This is done by comparing conventional and photonic spectroscopy. We begin by modelling both on a like-for-like basis using existing examples of instrumentation. We then extrapolate our models to hypothetical instruments and examine the science cases where a photonic spectrograph could be used effectively. We look at various options for redesigning the photonic spectrograph so it is more suitable for astronomy. We conclude with two options that we believe are most appropriate. Finally we describe designing, building and testing a photonic-dicer. This takes the light from the telescope and reformats it into a long slit and is essential to our redesigned photonic spectrograph.

Chaper 2 describes the theory behind spectroscopy, both from the point of view of photonics and astronomy. It also describes the major current instrumental techniques in the astronomical community and examines photonic instruments that have been developed as demonstrators. This chapter is mostly based upon the work of others, though contains some original work.

Chapter 3 takes the initial attempts to make photonic spectrographs and compares them with existing instrumentation. It looks at areas where these devices could compete with conventional instrumentation. It is largely drawn from [16].

Chapter 4 takes the results from the previous chapter and extrapolates them to conceptual instrumentation. It look at areas where photonic devices could show advatanges over conventional instrumentation. It then looks at the science cases that would be benefited by photonic instruments, comparing it to similar studies in the astronomical world. It is drawn from the work in [17] and in a summer school poster created for the Astrophotonic summer school in Potsdam 2012.

Chapter 5 takes the results from the previous chapters and looks at how the IPS could be redesigned to better suit astronomical needs. This includes concepts proposed by other groups and examines the relative strengths and weaknesses of the concepts. It then identifies two potential concepts we believe are most appropriate to the astronomical community and identifies the components that would be required to make them work. It is based on [18].

Chapter 6 draws on the results of the previous chapters. It describes the design, manufacture and testing of a photonic-dicer chip. This chip reformats the input from a telescope into a long slit. It was designed and built at Heriot-Watt university and was taken to the William Herschel Telescope (WHT) in 2013 to be used on the CANARY Adaptive Optics system. The contents of this chapter are drawn from and expansions of [19].

Finally Chapter 7 concludes by summarising the results from the previous chapters and identifies further work that could be undertaken in the area of photonic spectroscopy.

Chapter 2

Spectroscopy Theory

2.1 Introduction

In this chapter we shall introduce the theory of spectroscopy in two differing areas. Photonics, which here refers to instruments and practises developed for the telecommunications industry, as well as astronomical spectroscopy. We shall then deal with their convergence in the field of astrophotonics.

We shall concentrate on instruments that use a dispersive element such as a prism or a diffraction grating to examine light at different wavelengths, concentrating on those that use interference rather than refraction to achieve their goals. Whilst there are other types of spectroscopic instrument within astronomy, these are less common and are outside the scope of this thesis. For further information on such instruments see [20].

We will discuss the differing types of dispersive instruments in modern spectroscopy and the problems associated with them, particularly with respect to instruments on larger telescopes. We shall then discuss spectroscopy in the world of photonics, paying particular attention to the rising use of the AWG.

We close by discussing the possibility of combining the two different areas and the potential obstacles that need to be overcome if this is to provide useful benefits within astronomy.

2.2 Astronomical Spectroscopy

Spectroscopy has been a mainstay of modern astronomical observations for many years. It allows examination of many types of objects on all physical scales, from detection and studies of small objects such as exoplanets right up to measuring properties of the oldest galaxies on the largest cosmological scales.

By separating the light into its constituent wavelengths and looking at the relative fluxes and positions of spectral lines, properties such as temperature, relative velocity and distance and elemental composition can be inferred.

This is spectroscopy's strength, and whilst the results are less attractive than imaging, it can give us a lot more information about the physics of our universe. Armed with this astronomers can infer the laws that govern the smallest to largest scales.

2.2.1 Conventional Spectrograph Theory

Even though modern spectrographs are hugely complex instruments their operation can be explained by a basic model. This model consists of a slit, which isolates the spatial area to be dispersed, a collimating optic which collimates the light from the slit, a dispersive element such as a grating or prism, a camera optic which refocuses the light from the collimator and then a detector to collect the light. For an illustration of this see figure 2.1. This section and the following one on Free Spectral Range (FSR) are heavily influenced by [21], [22] and [1].

We begin with the standard grating equation (e.g. [21]), which describes how collimated light incident on the diffraction grating behaves. This equation
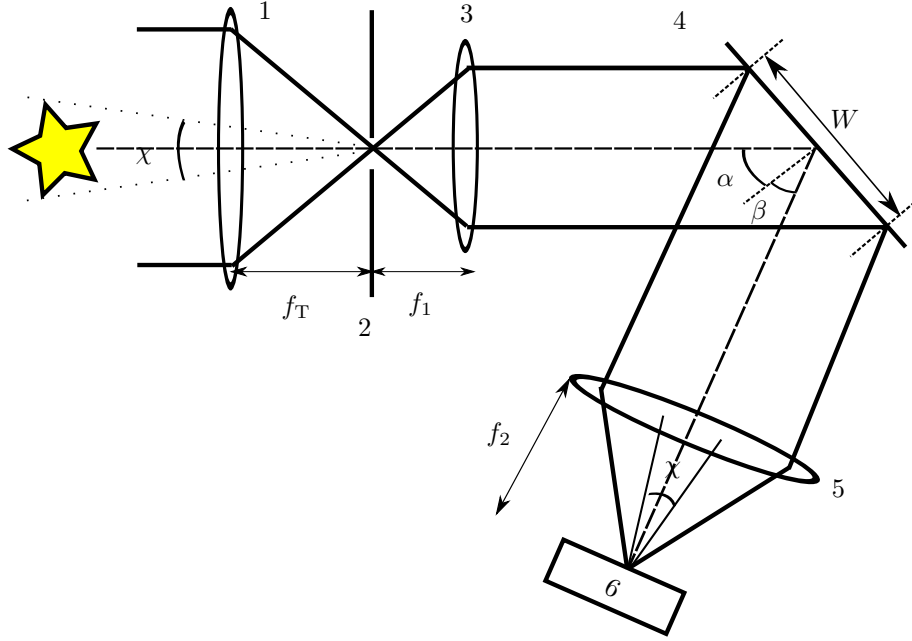
Figure 2.1: A simplified diagram of a conventional dispersive spectrograph setup. This consists of the following numbered components. 1) The input telescope optics (here a single lens). 2) A slit to isolate the area to be dispersed. 3) A collimating lens to collimate the light from the telescope. 4) A diffraction grating to disperse the light. 5) A camera lens to reimage the light from the telescope onto the detector. 6) A detector, to collect the light. The lenses at 3) and 5) are commonly replaced with mirrors to reduce chromatic aberrations.

is

$$m\rho\lambda_{\mathrm{c}} = (\sin\alpha + \sin\beta)\,n. \tag{2.1}$$

Here m is the diffraction order, ρ is the grating ruling density (which is usually given in mm^{-1}), λ_{c} is the central wavelength of operation, α the angle of incidence on the grating, β the angle away from the grating and n is the refractive index of the medium. For most spectrographs the medium is air so $n \approx 1$. Also note the sign is positive for a reflective grating and negative for a

transmissive grating.

In order to obtain the angular dispersion due to the grating we differentiate with respect to β, yielding

$$\frac{d\lambda}{d\beta} = \frac{\cos\beta}{m\rho}.$$

(2.2)

We note that $f_2 d\beta = dx$, where f_2 is the focal length of the camera and dx is the physical displacement in the spectral direction. Combining this with equation 2.2 we can calculate the linear dispersion at the detector

$$\frac{d\lambda}{dx} = \frac{d\lambda}{d\beta}\frac{d\beta}{dx} = \frac{\cos\beta}{m\rho f_2}.$$

(2.3)

This is useful for calculating the spatial separation of different wavelengths, though we also wish to know the smallest difference in wavelength that can be resolved. This is called the spectral resolving power and is defined as $R = \lambda/\delta\lambda$. To begin we consider a spectrograph with an infintiessimally narrow slit. Whilst the slit itself is infinitesimally narrow the output line will not be, due to instrumental broadening [21]. Due to this effect the angular half width (the distance between the maxima and first minima) of the line will be

$$\Delta\beta = \frac{\lambda}{W\cos\beta}.$$

(2.4)

where W is the intersection of the collimated beam and the grating. Rearranging and combining equations 2.2 and 2.4 we can now calculate the spectral resolving power using the Rayleigh criterion. This theoretical maximum is then given by

$$R^* = \frac{\lambda}{d\lambda} = \frac{d\beta}{d\lambda}\frac{\lambda}{\Delta\beta} = m\rho W.$$

(2.5)

As stated above this is only true for an infinitesimally small slit. Often, astronomical spectrographs do not fall into this category due to turbulence in the atmosphere blurring out the source. This is known as the seeing limited regime. In order to allow a significant amount of light to enter the spectrograph we need to increase the width of our entrance slit. In doing so we trade-off increased throughput with decreased spectral resolution. To calculate this factor we need to consider the width of the image of slit within the system, projected onto the detector. We use conversation of etendue, which holds for conventional optics with no aberrations. This can be for optics such as lenses and mirrors, or idealised fibres. This can be stated as

$$n\Omega A = \text{constant.} \tag{2.6}$$
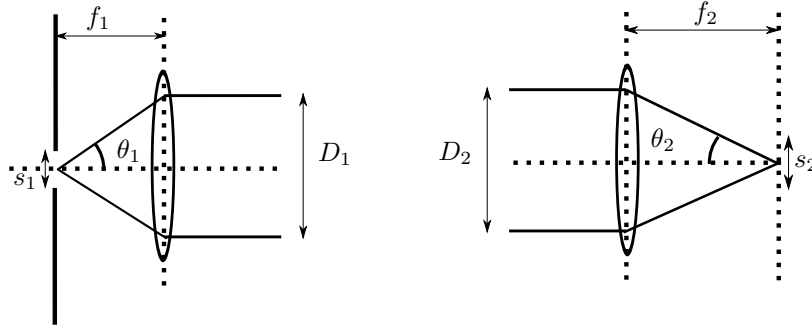
Figure 2.2: Diagram illustrating conservation of etendue in one dimension. Here the focal length of the camera f_2 is greater than that of the collimator f_1. The diameter of both beams are the same ($D_1 = D_2$).Thus the image of the slit s_2 must be greater in size than s_1.

Where Ω is the solid angle of radiation incident on the surface area A. For our system we only consider one dimension so we can state $s_1\theta_1 = s_2\theta_2$ where $\theta_i = D_i/f_1$ and $F_i = f_i/D_i$ for i= 1,2 (see figure 2.2). This yields

$$s_2 = s_1 \frac{\theta_1}{\theta_2} = s_1 \frac{F_2}{F_1}. \tag{2.7}$$

We now know the width of our slit at the detector. In order to spectrally resolve two wavelengths they will have to be separated by this distance. We can now express this as the spectral resolution; to do this we express width of the slit in wavelength units.

$$\delta\lambda = \left(\frac{d\lambda}{dx}\right) s_2 = \frac{\cos\beta}{m\rho f_2} s_1 \frac{F_2}{F_1} = \frac{s_1 D_1 \cos\beta}{m\rho D_2 f_1} \tag{2.8}$$

From figure 2.1 we can see that $W = D_2/\cos\beta$, meaning $\delta\lambda = s_1/m\rho F_1 W$. We can then express the resolving power as

$$R = \frac{\lambda}{\delta\lambda} = \frac{m\rho\lambda F_1 W}{s_1}. \tag{2.9}$$

For astronomy we want to relate this to the angular slit width (χ) as projected on the sky and the telescope aperture (D_T). For this it can be noted that

$$s_1 = \chi f_T \tag{2.10}$$

and if the spectrograph is fed directly from the telescope (e.g. conservation of etendue holds)

$$\frac{f_T}{D_T} = \frac{f_1}{D_1} = F_T = F_1. \tag{2.11}$$

We can then express the resolving power as

$$R = \frac{m\rho\lambda W}{\chi D_T}. \tag{2.12}$$

You can see that contained within the nominator is the spectral resolving power for an ideal spectrograph. Thus if $\chi D_{\mathrm{T}} = \lambda$ we can say we are diffraction-limited and if $\chi D_{\mathrm{T}} > \lambda$ we shall obtain a resolving power lower than the theoretical maximum.

In practise this happens frequently on larger astronomical telescopes due to turbulence in the atmosphere. From equation 2.12, if χ stays constant the spectral resolving power drops inversely with the diameter of the telescope. This means that to maintain the same throughput (e.g. the same angular slit width) the collimated beam and diffraction grating must become larger.

Manufacturing such large gratings is difficult with resulting wavefront (e.g. diffuse stray light caused by micro roughness) and ruling error (e.g. ghost lines) limiting the final spectral resolution (e.g. [23, 24, 25] and references therein). In addition exotic materials are required to minimise flexure, driving up costs.

Free Spectral Range

Another important consideration for instruments with a diffraction grating is the FSR of the system. The FSR is defined by the point where two wavelengths in different spectral orders occupy the same physical position at the detector (see figure 2.3). As most detectors (e.g. Charge-Coupled Device (CCD)s [26, 27] and Indium Gallium Arsenide (InGaAs) [28] cameras) cannot measure wavelength any spectral overlap will produce errors in the output measurement. There are four main alternatives

- Use dispersion instead of multi-beam interference (e.g. a prism instead of a diffraction grating) as these do not suffer overlapping spectral orders.

- A subset of detectors (e.g Microwave Kinetic Inductance Detectors [29], Superconducting Tunnel Junctions [30] and Transition Edge Sensors [31]) allow energy resolution, which would mean this overlap is not a problem.

Whilst this could be a revolution for astronomical instrumentation, these devices are currently in the early stages of development and are only just beginning to be used in near-infrared astronomy [32].

- The system can be cross dispersed. This will be discussed in section 2.2.2.

- Use a filter to block portions of the light. This has the disadvatange that light is lost from the instrument, although it is a relatively cheap solution.
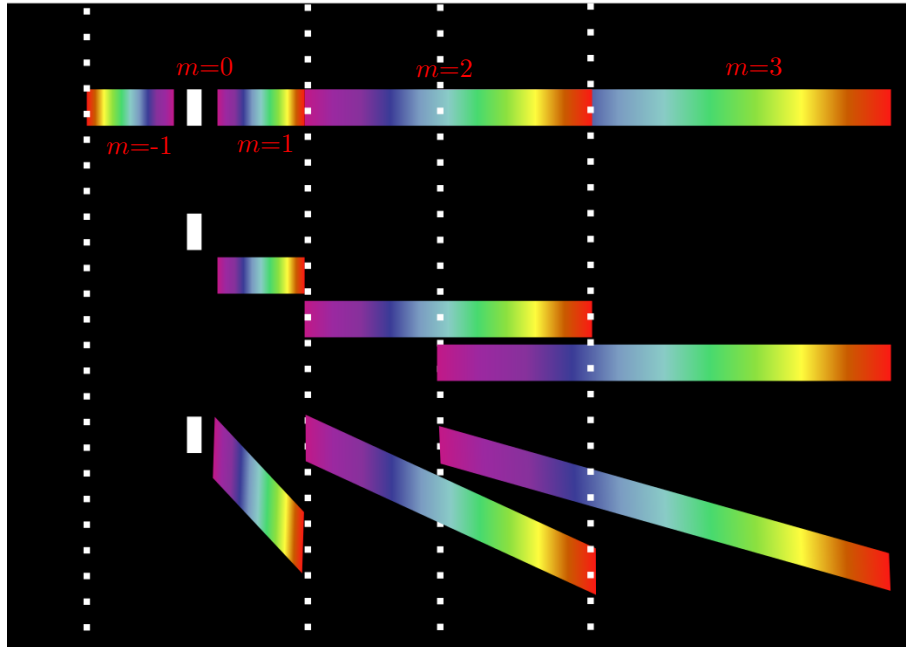
Figure 2.3: Illustration of Free Spectral Range. The top illustrates how a spectrum would appear in a conventional spectrograph with no blocking filters. You can see that m=2 and m=3 overlap for this spectral range, thus if being observed would not be able to resolve some of the wavelengths. The middle shows the different orders separated in order to illustrate free spectral range. The bottom shows a simplified echelle spectrograph. Here the orders are cross dispersed using another dispersive element. This allows a much greater Free Spectral Range.

For the final two solutions we still need to know how to calculate the FSR. To do this we re-arrange equation 2.1 for the two overlapping wavelengths, λ at spectral order m and $\lambda + \Delta\lambda$ at spectral order m. Noting that they lie at the same position equation 2.1 becomes

$$\frac{1}{\rho}\left(\sin\alpha + \sin\beta\right) = \left(m+1\right)\lambda = m\left(\lambda + \Delta\lambda\right). \tag{2.13}$$

Rearranging for $\Delta\lambda$ gives the FSR

$$\Delta\lambda_{FSR} = \frac{\lambda}{m}. \tag{2.14}$$

From equation 2.14 we can see as the spectral order increases the FSR decreases. This is the inverse of the equation for resolution which increases as the spectral order is increased. Hence we have another tradeoff, spectral resolution and FSR.

2.2.2 Differing inputs for dispersive spectroscopy

So far we have discussed a simplified spectrograph, with the telescope focussed into a long slit, which feeds the spectrograph. We have already discussed the limits of these spectrographs in terms of size, spectral resolution and FSR, but they are also limited in the number of objects they can observe simultaneously.

The intuitive way to solve this problem of spectral resolution is to try to increase the ruling density (the number of rulings per mm on the grating) or simply expand the collimated beam onto a larger grating. These are expensive options however; high ruling density gratings (greater than around 1000 lines per mm) and large gratings (bigger than 300mm) are difficult to produce, prone to flexure and easily broken.

A common solution to keep component sizes and instrument complexity

manageable is to cross disperse the spectra. This involves using a grating in a high spectral order in order to obtain the high spectral resolution, although with limited FSR. A second disperser (commonly a prism) is then employed perpendicular to the original in order to cross-disperse the output, sorting the different spectral orders (see figure 2.14).

These spectrographs do not however, solve the problem of limiting numbers of objects and you can usually only observe a single object at a time (as they still require a slit). They also restrict your ability to observe extended objects efficiently (to do so requires taking many observations, moving the slit accurately across the object). Since telescope time is limited, ways of increasing the number of observable objects is an active area of research.

Alternatives have been developed and these can be loosely classed into Multi Object Spectrograph (MOS) and Integral Field Spectrscopy (IFS). A MOS allow observations of multiple objects in the field of view [33] whist IFS allows small patches of sky to be spatially resolved by an Integral Field Unit (IFU) (e.g. for observation of extended or spatially adjacent objects) [34]. To further increase the number and type of object that can be observed there is a combination of the two (using multiple IFUs) which is called Diverse Field Spectroscopy (DFS) [35].

MOS has been around for longer than IFS. Early examples include slitless spectroscopy, which removes the slit from the spectrograph, allowing the objects to be dispersed using a prism onto a photographic plate or CCD (e.g. [36]). This has the advantage that multiple objects can now be observed, but suffers from problems with crowded fields and extended objects due to overlapping spectra. This means the technique is still in use today, though is less common. Multi slit spectroscopy can solve the problems of slitless spectroscopy, using a cut mask with many smaller slits (e.g. IRIS 2 [37] and VIMOS [38]) This removes

the unwanted stars, although requires accurate manufacture. Modern systems normally now rely on reconfigurable fibre optics, which allowing much greater versatility, allowing easy placement in crowded fields and rearrangement of the fibres to stop resulting spectral overlap on the detector (e.g. AAOmega [39] and FMOS [40]). This technique also allows the light to be brought to a spectrograph on a stable platform further from the telescope. Whilst this introduces extra optics (such as the addition of a de-rotator on the Naysmyth focus), it means the instrument can remain fixed with respect to the gravity field, increasing stability [41]. Such instruments are now allowing huge surveys on smaller research grade telescopes (e.g. BOSS [42]).

IFS is a more recent development, although it has rapidly expanded to become a mainstay within astronomy. It is achieved through four main methods: image slicers (e.g. GMOS [43] and NIFS [44]), lenslet arrays (e.g. SAURON [45]), fibre slicers (e.g. [46]) and microslicers (e.g. [47]), these are shown and described in figure 2.4. It must be noted that although these all use novel inputs, the spectrograph behind is very similar to the long slit analogue.

DFS is also a rapidly expanding field, with instruments such as KMOS [48] paving the way for instruments planned for the next generation of ELTs (e.g. IRIS [49].)

Image slicing can also be used to improve the spectral resolution of a spectrograph (by reducing the width of the slit) (e.g. CYCLOPS [50] and [51]) and using the technologies developed for MOS and IFS allows the output from the telescope to be split into multiple replicated spectrographs (e.g. VIRUS [52]).

2.3 Spectroscopy in the photonic world

Ground-based, seeing-limited astronomical instruments increase in size, complexity and cost as telescopes become larger. At the same time instruments
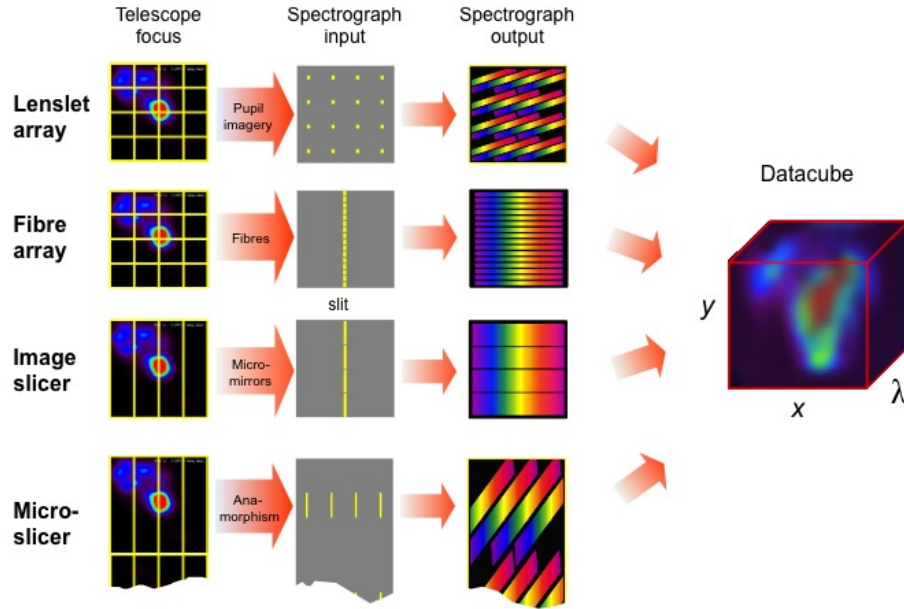
Figure 2.4: The different types of IFU reproduced with permission from Jeremy Allington-Smith. The first type uses a lenslet array placed at the telescope focal plane. This then focusses the light and is dispersed onto a detector; care must be taken to avoid spectra overlapping. The second uses a fibre to sample the telescope focal plane, this is then fed to a conventional slit spectrograph. Image slicers use mirrors to slice and reformat the image, which again is fed to a spectrograph. Micro-slicers are arranged similarly to image slicers whilst having multiple shorter slits. All four methods produce a datacube of axes x,y and λ

developed for the telecommunications industry are getting smaller with the aim of becoming mass producible and robust. As with the previous section we shall concentrate on those instruments that are dispersive, in particular the AWG.

2.3.1   The Arrayed Waveguide Gratings in photonics

Recent years have seen a huge growth in the amount of traffic in the telecommunications network. In order to allow for this expansion optical technologies have been used to replace slower electronic components. Most noticeable is the adoption of fibre optic cables transporting data over long distances, but there has also been development in the use of optical switches to allow multiple signals (multiplex) to be input into these fibres. These signals can be multiplexed in the time domain, although this is dependent upon electronic components, so is limited by the speed of these components. They can also be multiplexed in the wavelength domain, allowing multiple signals to be separated by wavelength selective components, allowing a greater increase in speed. Here we describe the AWG, a commonly used wavelength multiplexing device.

The AWG is a planar device, with a guiding core layer surrounded by two cladding layers. The input to the AWG consists of a single mode waveguide, which accepts light from a single mode fibre. The light from this waveguide then enters a Free Propagation Zone (FPZ), which allows the light from the fibre to propagate freely. A set of single mode Arrayed Waveguides (AW)s then accepts the light. Each subsequent waveguide has a length increase relative to its neighbour. This adds a phase delay between the waveguides in a similar manner to tilting a diffraction grating. A second FPZ then allows the light from the AW to interfere, resulting in a spectrum. This is then separated by output fibres placed at the output of the FPZ. For an illustration see figure 2.5.

Although material composition varies between device, the devices themselves
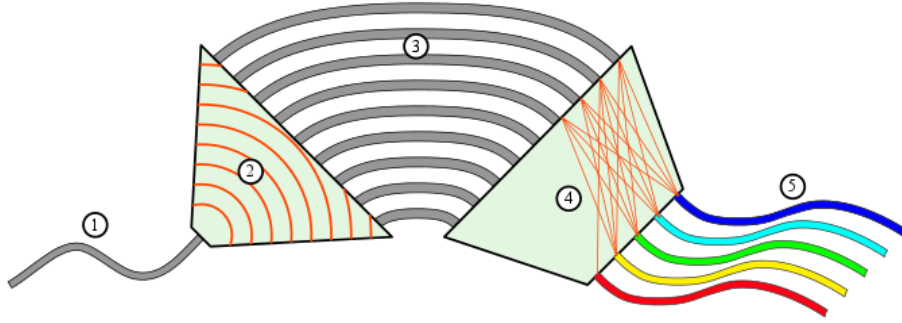
Figure 2.5: A simple diagram of an Arrayed Waveguide Grating reproduced from [55]. 1) The input fibre. 2) The first Free Propagation Zone showing the wavefronts of the light. 3) The Arrayed Waveguides, note the incremental length increase which causes the phase shift between adjacent guides. 4) The second Free Progagation Zone, showing the interference of light. 5) The output waveguides with different wavelengths.

are usually of silicon or silica construction (e.g. [53], pg 418). First a cladding layer is deposited upon a substrate, usually by flame hydrolysis deposition or photolithography [53]. The core layer (which has a higher refractive index) is then deposited onto this and the chip consolidated by heating to a high temperature. Reactive ion etching is then used to remove unwanted areas of the core to leave the AWG pattern [53]. A further layer of cladding is then deposited and the whole chip consoliated. The chip is tested and if errors are discovered in the positioning of the output wavelengths with respect to the desired wavelengths this can be corrected by modifying the core index in the AW channels (e.g. by using a carbon-dioxide laser [54]).

2.3.2   Modelling the AWG

There are various methods for modelling the AWG (see [53] for more details). Here we examine two models which concentrate on light propagation in the FPZ of the AWG. The first is based on Fresnel propagation, which is computationally
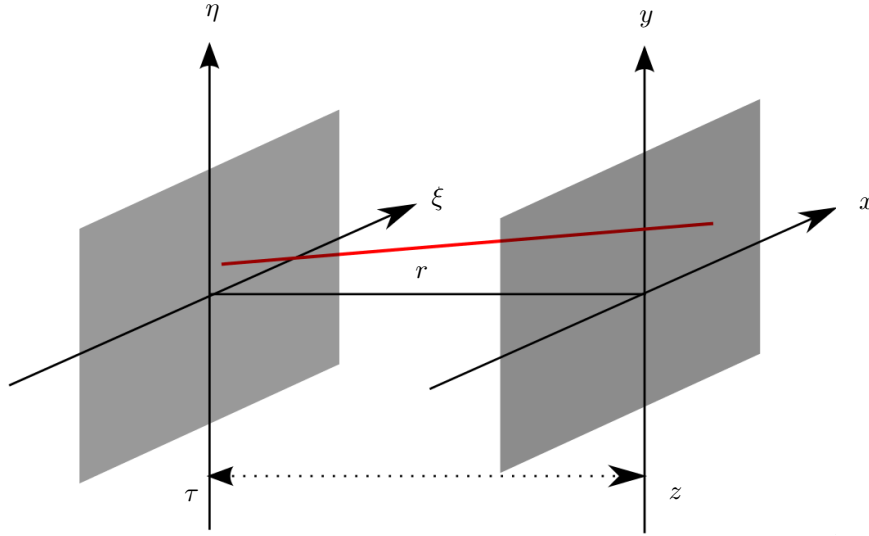
Figure 2.6: Diagram of the planes in transfer equation. For our purposes the input plane is ξ, η, τ and the output plane x, y, z. By allowing τ and z to vary with ξ, η, or x and y differing geometries can be produced (not just flat planes illustrated). Modified from an illustration in [56].

intensive, but allows modelling of arbitrary FPZ geometry and is accurate over small scales. The second assumes the FPZ is a perfect lens, allowing Fourier transforms to be used, greatly decreasing the time taken for the modelling. Note that both models assume the material is homogenous, with no surface roughness or birefringence. It also assumes the devices are manufactured to specification, with no defects.

Fresnel Model

In our model we will utilise equations for Fresnel light propagation in one dimension. This is based upon that developed in [57].

We use the approximation for Fresnel diffraction using the Helmotlz equation (e.g. [56] pg. 58) to obtain the electric field at our propagated plane. This is

$$\Psi(x, y) = -\frac{i}{2\lambda} \int \int \Psi(\xi, \eta) \cos \theta_p \frac{e^{ikr}}{r} d\xi d\eta. \tag{2.15}$$

Where k is the wavenumber, defined as $k = 2\pi n/\lambda$, Ψ is the field at the input and propagated planes, r is the distance between two points in the initial and propagated plane (see figure 2.6), we define

$$\cos \theta_p = \frac{z - \tau}{r} = \frac{(z - \tau)}{\sqrt{(x - \xi)^2 + (y - \eta)^2 + (z - \tau)^2}}. \tag{2.16}$$

Substituting this back into 2.15 in leaves

$$\Psi(x, y) = -\frac{i}{2\lambda} \int \int \Psi(\xi, \eta)(z - \tau) \frac{e^{ikr}}{r^2} d\xi d\eta. \tag{2.17}$$

As we only require one dimension for our planar device we set $y=0$, this yields the one dimensional Fresnel transfer function, which is what we require for our planar AWG. This is

$$\Psi(x) = -\frac{i}{2\lambda} \int \Psi(\xi)(z - \tau) \frac{e^{ikr}}{r^2} d\xi. \tag{2.18}$$

This method is highly accurate, as it allows the user to specify the geometry for each end of the FPZ of the AWG, though it is a very slow and computationally expensive method. A much less computationally intensive method version assumes that the FPZ is an analogue of a perfect lens. This however does not account for any errors in the design or manufacture and care must also be taken to ensure that the Fourier approximations hold. It also does not allow the modelling of other variables, such as multiple inputs to the AWG, which has been used in one of the IPS demonstrators [5]. This model was developed by [58] and an adapted version that allows for our purposes is detailed below.

Modified Munoz model

Firstly we relax the free geometry in equation 2.18 and consider light focussed from a perfect lens (see equation 5-16, pg 105, [59]). As we are working in the paraxial regime and assuming a paraxial lens (e.g. no aberrations), we can write the transform as

$$\Psi\left(u\right) = \left.\frac{1}{\sqrt{\alpha_\nu}}\mathcal{F}\left\{\Psi\left(\xi\right)\right\}\right|_{u=x/\alpha_\nu}. \tag{2.19}$$

Here we evaluate the Fourier transform ($\mathcal{F}$) at the frequency $u = x/\alpha_\nu$. Note this means our spatial scaling will differ between the two planes and any code using the FFT routine will be required to interpolate results of this to allow the same spatial scaling. In equation 2.19 α_ν is defined as

$$\alpha_\nu = \frac{cL_{\mathrm{F}}}{n_{\mathrm{s}}\nu} = \frac{\lambda L_{\mathrm{f}}}{n_{\mathrm{s}}}. \tag{2.20}$$

Where c is the speed of light, L_{F} is the length of the FPZ, n_{s} the refractive index of the cladding, ν the frequency of light. This approximation holds for the Fraunhoffer diffraction. This means the FPZ needs to fulfil (equation 4-24, pg 74 , [59])

$$L_{\mathrm{F}} \gg \frac{\pi W_x^2}{\lambda}. \tag{2.21}$$

Where W_x is the width of the input waveguide (equivalent to s_1, the input slit width in our conventional spectrograph). Note that α_ν is wavelength dependent for multiple orders.

Model input

With a transfer function complete we can model the FPZ regions of the AWG. The first input plane of the AWG is dependent on the type of input used. In

telecoms this is usually a Single Mode (SM) fibre so can be approximated as a gaussian (or a cosine in the core with an exponential drop off in the cladding). Astronomical applications will most likely require a different input, though this is not explored here.

The Arrayed Waveguides

We have dealt with how the light is propagated in the FPZ, either by equation 2.18 or 2.19. We must now deal with the AW section of the AWG. To do this the overlap integral must be calculated between the result of equation 2.18 and the electric field of the AW.

$$a = \int_{-\infty}^{\infty} \Psi(x)\,\psi(x)\,dx \tag{2.22}$$

where ψ is the AW electric field of the arrayed waveguides. The electric field for an individual SM waveguide is usually approximated as a gaussian [58]

$$\psi_{\mathrm{s}}(x) = \sqrt[4]{\frac{2}{\pi w_i^2}}\,e^{-(x/w_i)^2} \tag{2.23}$$

where

$$w_i = W_{\mathrm{i}}\left(0.321 + 2.1V^{-3/2} + 4V^{-6}\right). \tag{2.24}$$

Here W_{i} is the waveguide diameter (and hence S in equation 2.32 is W_{i}). Thus for a set of waveguides spaced uniformly by d_{w} we can make use of equation 2.23 to write the field distribution as

$$\psi(x) = \sum_{j=1}^{N_{\mathrm{wg}}} \psi_{\mathrm{s}}\left(x + (j-1)d_{\mathrm{w}} - \frac{(N_{wg}-1)}{2}d_{\mathrm{w}}\right) \tag{2.25}$$

where N_{wg} is the total number of waveguides.

However to calculate the field at the other end of the AWs we need to add the phase difference between them. To do this we take the length of AW j, which can be given by

$$l_j = l_0 + \Delta l \left(j + \frac{N_{wg}}{2} \right).$$ (2.26)

Where l_0 is the length of the shortest waveguide, which corresponds to $j = -N/2$. The value of Δl is set to an integer multiple of m of the design wavelength in the waveguides

$$\Delta l = \frac{m\lambda}{n_c} = \frac{mc}{n_c \nu}.$$ (2.27)

The value of Δl ensures that the central output wavelength (COW) is focussed on the centre of the second FPZ. The phase change corresponding to this length increment is

$$\beta_p \Delta l = 2\pi m \frac{\nu}{\nu_0}$$ (2.28)

β_p is the propagation constant in the waveguides. This means corresponding phase shift in waveguide j is

$$\Delta \phi_j = \beta_p l_j = 2\pi \frac{n_c}{c} \nu l_j$$ (2.29)

This can then be introduced to 2.25 as a phase term, so this becomes

$$\psi(x) = \sum_{j=1}^{N_{wg}} \psi_s \left(x + (j-1)d_w - \frac{(N_{wg} - 1)}{2} d_w \right) e^{-(i\Delta \phi_j)}$$ (2.30)

Model summary

We now have all the tools to simulate the whole device. An input field can be calculated either as an approximation of a single mode (see equation 2.23) or an

arbitrary field. This is then propagated to the AW section using either equation 2.18 or 2.19. The overlap integral (equation 2.22) is calculated between the field at the beginning of the AW section and the phase difference between adjacent waveguides added (see equation 2.30). This is then propagated to the output of the AWG using equation 2.18 or 2.19.

Examples of modelling

Whilst not detailed within this thesis it is useful to briefly compare the results of the two models in order to ascertain where they are useful. As stated before, the Munoz model assumes each FPZ is a perfect lens. As no lens is perfect moving the input or output off axis means the results are less accurate using this model. In figure 2.8 (a) we show a large scale system with the central and two neighbouring orders visible on either side. Both models shown use identical input parameters and show near identical results on large scales. Where the models differ is shown in figure 2.8 (b). This displays the order adjacent to the central one. Here the position and shape of the output is different for the two models. This shows for low resolution (or single spectral order) quick modelling the Munoz model is perfectly adequate. For higher resolution, or modelling of other effects, a more detailed simulation is required.

2.3.3 Waveguide Modes

There are several issues with trying to combine the designs of the AWG with the requirements of astronomy. In principle some are easy to solve (though the reality maybe be more complex). For example the replacement of the input waveguides with a single mode fibre (which acts as an entrance aperture) and the removal of the output waveguides, which allow the digital outputs that are used in telecoms to be adapted to the analogue spectra that are sampled from
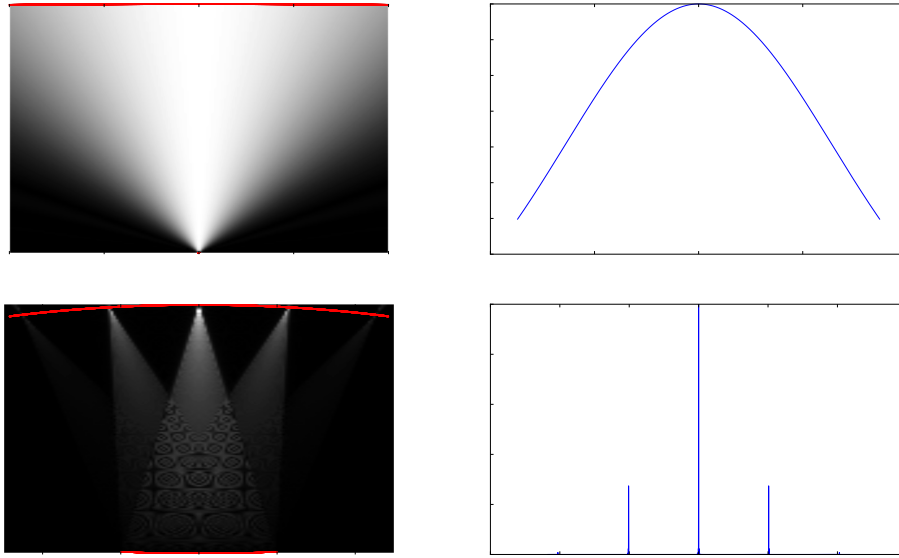
Figure 2.7: An example of AWG modelling. Top left is square root of the intensity in the first FPZ, top right the intensity at the input to the AWs. Bottom left is square root of the intensity in the second FPZ, bottom right the intensity at the detector. This is simulated using the Fresnel code. The red line in the two left hand images is the geometry of the FPZ. Figure for illustration purposes.
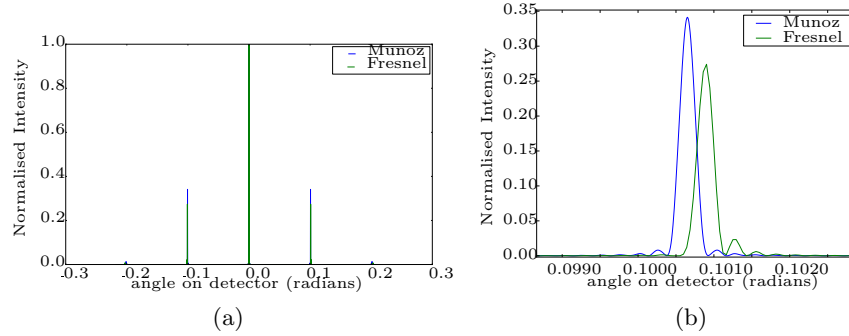
Figure 2.8: Comparing the results of the Munoz and Fresnel Models at the detector. Both models assume a Rowland circle arrangement. Here the Munoz model is shown in blue, with the Fresnel model shown in green a) Full output at the detector, with the central and two neighbouring orders visible on either side. As stated in the main text the results are almost indistinguishable. b) The first neighbouring order to the central one. As you move off axis the results from the Munoz simulation are less accurate than the Fresnel one, due to the assumption of a perfect lens.

astronomical objects.

Others however are more fundamental, such as the mismatch between the output of the telescope and the input of the AWG. We mentioned earlier that the AWG is designed for the SM input of a telecoms fibre and stated that this is well matched to a diffraction-limited source [60]. The output from a ground based telescope is generally seeing limited and and can be thought of as multi-moded. The number of modes is dependent on many factors which will be discussed within this thesis. We defined the diffraction-limit in section 2.2.1 and now define it in terms of the modes within waveguides.

Modes can be thought of as a consequence of two properties of light within a waveguide. The first property is associated with the ray model. Light can enter the waveguide at any accepted angle that is less than the critical angle allowed for total internal reflection. The light with the fastest travel time will be the meridional ray, which is co planar with the optical axis. Rays that enter

at other angles will take longer to travel the length of the fibre, leading to a different propagation constant, which we will return to later [21].

The second property is a consequence of the wave nature of light. For light to constructively interfere there needs to be a phase shift multiple of $\pi/2$ radians, or 90°. This means that the light exiting the fibre will be quantised and is called the modes of the fibre. For circular and square fibres (which we shall be dealing with here) these can be defined as Transverse Electrical (TE) and Transverse Magnetic (TM) modes. These have no electric (TE) and magnetic (TM) fields in the direction of propagation.

In both cases the mode number is defined by two suffix numbers for the mode type. For circular waveguides this is TE_{PL} and TM_{PL}, where the modes are circular symmetric and L is the number of half-wavelengths along the half-circumference, P is the number of half-wavelengths along the radius. Examples of these modes are show in figure 2.9. For square waveguides TE_{MN} and TM_{MN} M is the number of half-wavelengths along the width of the waveguide, N is the number of half-wavelengths along the height of the waveguide. Examples of these modes are shown in figure 2.10

The number of modes in a fibre depends upon many factors (the shape, composition, size) and has been extensively studied (e.g. [61, 62]). Here we only use the approximation for the number of modes within a circular and square step index fibre. To do this we define the V parameter, which is

$$V = \frac{2\pi}{\lambda} S\Theta = \frac{2\pi}{S} \sqrt{n_\text{c}^2 - n_\text{s}^2}. \qquad (2.31)$$

Where S is the radius of the fibre, Θ is the numerical aperture, n_c is the refractive index of the core and n_s the refractive index of the cladding. This will be used in many forms throughout the thesis. From this the number of modes (not including polarisation) can be approximated as
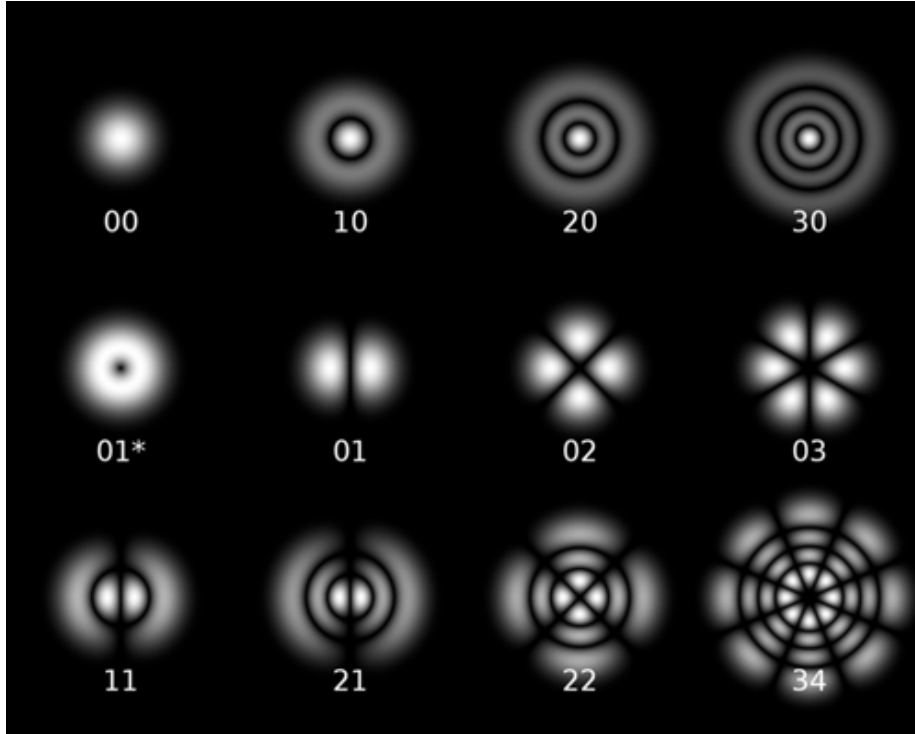
Figure 2.9: The TM$_{PL}$ modes in a circular optical fibre. The numbers in the images are PL. P is the number of half-wavelengths along the radius, L is the number of half-wavelengths along the half-circumference. The TE modes are the same, with the image rotated by 90°.
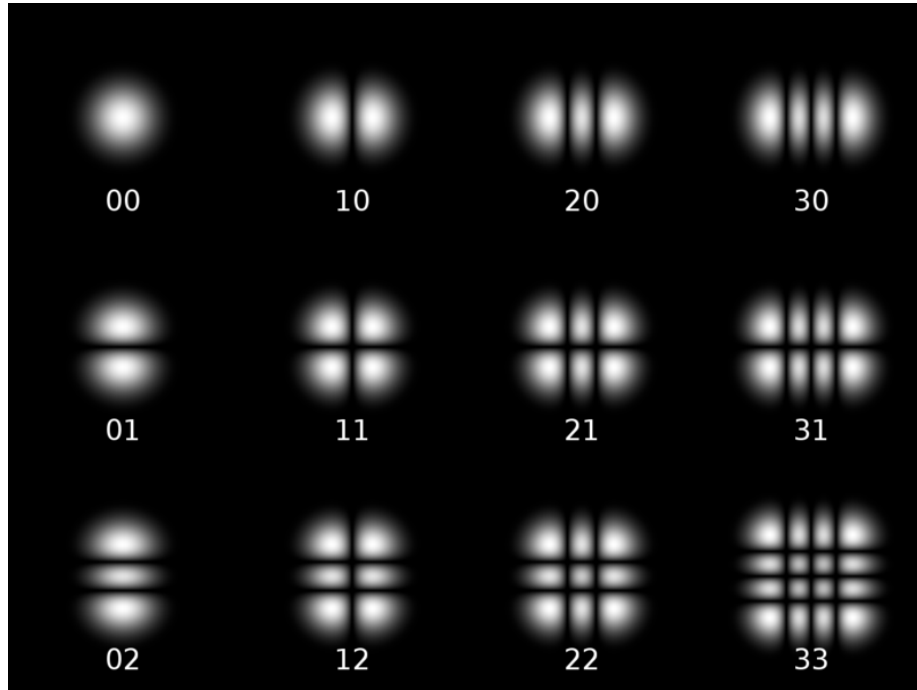
Figure 2.10: The TM$_{MN}$ modes in a square optical fibre. The numbers in the images are MN. M is the number of half-wavelengths along the width of the waveguide, N is the number of half-wavelengths along the height of the waveguide. The TE modes are the same, with the image rotated by 90°.

$$M = \frac{V^2}{4} \tag{2.32}$$

for a circular fibre (e.g. [61]). Or

$$M_{\mathrm{sq}} = \left(\frac{2V}{\pi}\right)^2 \tag{2.33}$$

for a square one [21].

2.4 Astrophotonics

We now discuss how photonic devices, such as the AWG can be used in astronomical instrumentation.

2.4.1 Coupling modes

In the previous sections we talked about how the spectral resolving power decreased as slit width increases. This also happens in the photonic world, though here instead of reducing the spectral resolving power we increase the number of modes and the number of AWGs required to adequately sample them. This drives up the size of the instrument, in a similar way to increasing the size of the collimated beam in a conventional spectrograph (even here there is no such thing as a free lunch).

To show this we define the resolution of an AWG as

$$R_{\mathrm{AWG}} = \frac{mN_{\mathrm{wg}}}{C}. \tag{2.34}$$

where C is a factor to account for manufacturing errors [63]. This has no dependence on telescope diameter so it would appear to break the relation. It must be noted though that this applies to a device operated at the diffraction

limit of the telescope, not at the seeing limit as with Equation 2.12.

We take the V parameter, defined in equation 2.31 and note that

$$\Theta \approx \frac{1}{2F_{\mathrm{T}}} \tag{2.35}$$

$$s_1 = \chi f_{\mathrm{T}} = \chi F_{\mathrm{T}} D_{\mathrm{T}} \tag{2.36}$$

where F_{T} the telescope focal ratio and f_{T} is the telescope focal length, the number of modes is given by

$$M = \left(\frac{\pi \chi D_{\mathrm{T}}}{4\lambda}\right)^2. \tag{2.37}$$

Therefore it can be seen that for each sampling element the number of modes increases as the square of the telescope diameter in a similar way to the number of slices at the diffraction limit $(\chi D_{\mathrm{T}}/1.22\lambda)^2$. This confirms that, to first order, photonic spectrographs are bound by the same scaling laws as conventional spectrographs [17].

This approximation can also be made for a square fibre, by taking the number of spatial modes for a one dimensional waveguide [21] and then squaring, from equation 2.33. This yields the number of spatial modes (again not including polarisation) in a square fibre as

$$M_{sq} \approx \left(\frac{\chi D_{\mathrm{T}}}{\lambda}\right)^2. \tag{2.38}$$

Note that the ratio between equations 2.37 and 2.38 is the ratio of the area of a circle to that of a square.

2.4.2   The photonic lantern

As shown in section 2.4.1 the number of spatial modes required to sample a Point Spread Function (PSF) increases with D_{T}^2 when the telescope input is seeing

limited (see the section 2.4.1 for further details). This means that a typical 4m telescope might require tens of modes at the seeing limit in the H band and a 40m telescope would require thousands for each spatial element in the near-IR. Correcting these modes using AO, or increasing the wavelength would reduce these numbers to more manageable levels. However, placing single mode fibres to sample all of these at the telescope focal plane would be exceedingly difficult and the fraction of area of collected light (fill factor) would be low, leading to light loss. We need a device to take the multimode light from a telescope and input it into an AWG (or alternatively reformat it into a diffraction-limited slit). This device is called the photonic lantern. The first one was manufactured in 2005 and was composed of SM fibres [64]. These were heated and drawn down to a single Multi Mode (MM) fibre using a capillary. This process is difficult though and alternative methods for the manufacture of fibre lanterns have also been proposed and demonstrated [65].

An alternative method for fabricating the photonic lantern has also been trialled using Ultrafast Laser Inscription (ULI) [66]. This uses an ultrafast pulsed laser to modify the refractive index of sections of a block of glass creating waveguides. By bringing these waveguides together the lantern can be made. The first device was created by [67], this was a 16 mode square array. Our ULI lantern will be described in Chapter 6.

2.4.3 Arrayed Waveguide Gratings in Astronomy

The use of photonic mux and demux devices in astronomy was first proposed by [14, 68], though the investigation suggested that at their current level of development they were not sufficiently advanced to be of use in astronomy. In 2006, [15] re-examined the idea of using photonic components in astronomy, this time with a far more positive outlook with regards to the use of photonic

components within astronomy.

The first practical work was undertaken by [3] in 2009. Initial tests were done using modified commercially-developed AWG. This had its output waveguides removed by polishing the surface back to the FPZ, the input fibre was retained and the device was packaged (similar to that shown in figure 2.11). It was then characterised in the lab where it showed transmission up to around 60%,(note this is with a laser input source, not the night sky). It was then taken to the Australian Astronomical Observatory (AAO) at Siding Springs, Australia. Here the output surface was re-imaged onto the IRIS 2 spectrograph [37] and the input fibre was placed so as to observe the night sky. As the device was not coupled to a telescope this showed that an AWG could be used to observe the night sky, though it did not show this technique could be used to efficiently observe astronomical objects.
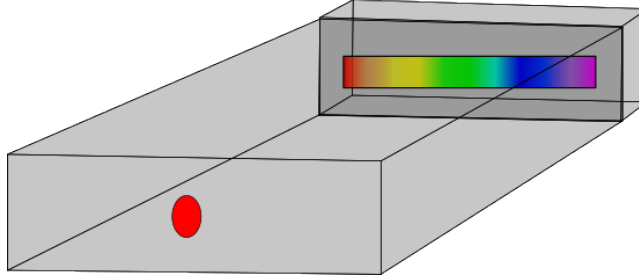
Figure 2.11: The single input design. A PL (not shown) reformats light from the telescope into single modes. Each single mode fibre feeds a conventional AWG which then disperses the light onto a detector. This detector can be linear if placed at the end of the AWG, or part of a 2D array if the output is re-imaged (not shown, but used in the experiments).

In order to make the concept viable for astronomy the device was redesigned and a new version was developed [69]. The SM fibre input was removed along with the input taper on the chip in order to increase the spectral resolution of the device. As with the previous device it also had the output waveguides

removed. It was tested in the lab, with spectral resolving powers up to 7000 measured and throughputs of up to 77% with a SM input [5]. These values were found to be lower for off-axis inputs. It was then tested on sky at the AAO in 2012 [70].

This time the AWG was fed by a lenslet coupled fibre PL to allow for a non diffraction-limited input (see Section 2.4.1). The PL consisted of nineteen cores drawn to a single MM fibre. Twelve of these cores were then re-arranged into a linear input of discrete single modes which was fed into the AWG (similar to that shown in figure 2.12). The separate inputs produced overlapped spectra at the output of the AWG. Because of this IRIS 2 [71] was used to cross disperse in order to separate out the obtained spectra. The results showed a similar throughput to the lab value (though the throughput was around 0.03 - 0.07% including telescope coupling and lantern losses) and lowered spectral resolving power (around 2500).
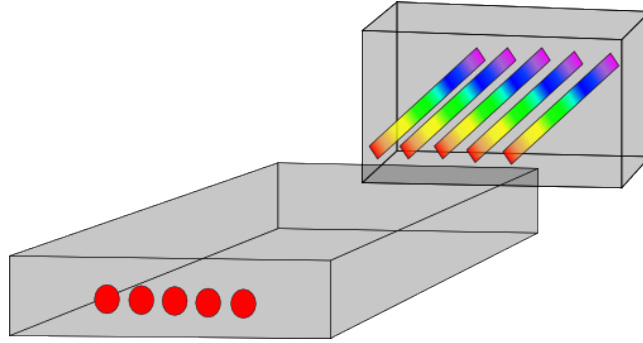
Figure 2.12: The cross dispersed AWG design. A PL (not shown) reformats light from the telescope into single modes. Multiple single modes are input to a single AWG. The resulting spectra are then cross dispersed at the output end using additional optics (not shown for clarity) onto a 2D detector.

2.4.4 Conventional spectrographs with photonic components

There has also been a proposal to use the PL coupled to conventional spectrographs [72]. These spectrographs utilise the SM fibres as the input to the spectrograph, the advantages of which are discussed later. There have been two proposed designs. The first is the Tiger concept, which is very similar to the lenslet IFU described above (e.g. [73]). The second concept requires the reformatting of the outputs from the PL into a long slit [72]. Both have inherent advantages and disadvantages, which will be discussed in later chapters.

2.5 Conclusions

We have discussed the theory behind spectroscopy, firstly in terms of astronomy and from the perspective of photonics. We have looked at how photonic spectrographs can be coupled to astronomical telescopes, first theoretically and then practically, examining current experimental work.

We began by discussing the theory behind modern spectrographs. We showed that for the seeing limited regime, the size of a long slit spectrograph is related to the diameter of the telescope it sits behind. In our calculations we did not take into account aberrations from the optics in the spectrograph, which would further increase the size relation. We briefly discussed the FSR of a spectrograph and how it relates to other parameters. We then discussed alternative ways of creating spectrographs, with examples of modern instruments. At this point we have not formally explored corrected systems, which will be explored in later chapters.

We then moved onto describing spectroscopy in the telecommunications world. We introduced the AWG, a device that acts as a digital spectragraph,

allowing signals to be multiplexed. We described models for the device, noting that these are simplified and would need additions to fully measure the capabilities of the devices. We then briefly examined the theory of waveguide modes as these will be important later.

Finally we concluded our chapter by detailing some of the work that has already been done combining photonic spectrographs with astronomical telescopes. The current work has been done with seeing limited telescopes and are technology demonstrators so not full devices. We looked at both fully photonic and semi photonic devices.

Chapter 3

Models of the IPS and existing Instruments

3.1   Introduction

In this chapter we determine the application areas where the IPS may have an advantage over conventional instrumentation. After defining our versions of the IPS in section 3.2, we consider the requirement for the field of view of the instrument in section 3.3. Simplified models of the IPS are presented in sections 3.4 and 3.5. The results of comparing conventional and IPS instruments is given in section 3.6. In section 3.7, we discuss different ways to reduce the number of AWGs and/or detector pixels, before presenting our conclusions in section 3.8. The chapter is largely drawn from [16].

3.2 The IPS

In this chapter we shall assume the IPS devices take light from an input fibre which is matched to the seeing limit (as with conventional fibre fed instruments) or an AO system and so supports few to many modes, further options will be explored later. The light from this MM input is then split into a number of SM fibres by a PL. At this point two options have been proposed [72].

P=1: The first requires a reformatting component [74, 67] to form a slit of SM fibres which can then be dispersed by bulk optics. We shall call this the semi-photonic case.

P=2: In the second the SM fibres are fed into AWGs which disperse the light into individual spectra, with one or more spectra per AWG [72]. These spectra have the advantage that they are in a linear format, so can be sampled using an array of fibres or a linear detector. This is our fully-photonic case.

3.3 The input field and spatial multiplex

In the previous chapter we approximated the number of modes per spatial sampling element (spaxel), this is equation 2.37. As with diverse field spectroscopy [35], photonic spectrographs address a number of individual spaxels, which can be grouped (as in Integral Field Spectroscopy; IFS), or separate (as in Multi Object Spectroscopy; MOS). In order to fairly compare with conventional instrumentation we need to make sure we sample the same number of spaxels (e.g. observe the same field).

A long slit can be thought of as a series of spaxels joined to form a rectangle of size $1 \times N$, where N is the total number of spaxels. In IFS, the field is equivalent to a series of slits (each composed of linked spaxels) joined so the total number of

spaxels is $N = N_x N_y$, where N_x is the number of spaxels in the x direction and N_y in the y direction. MOS can be thought of as the same number of spaxels, N, distributed throughout the field of the telescope and brought together to form a long slit. See figure 3.2 for an illustration of this.

An important consideration is the sampling of the field. From figure 3.1 and equation 2.37 it can be seen that the number of modes produced is dependent on the overall size of the field, not the individual spaxel size (as the number of modes per spaxel is proportional to the square of the spaxel size). This means the number of components for the IPS (and hence the approximate size of the instrument) required for the instrument will not depend on the sampling scale. However, the amount of spatial information and throughput will depend on the sampling scale. Although it might appear best to reduce the spaxel size and the number of modes, this will reduce the coupling efficiency and throughput[75]. At the other extreme the use of very large fibres would result in loss of spatial information. A balance must be found between throughput and spatial resolution. We do not investigate this fully here as it does not affect the total number of modes in the field or the required number of detector pixels. Thus we choose to make our spaxel size equal to the FWHM of the seeing.

In order to calculate the scale length of the instrument we take the cube root of the volume of the instrument. We can calculate this from the number of spaxels in the total field passed to the spectrograph

$$\text{scale length} = \sqrt{NM(\lambda_{\min})^{P-1} L_x L_y L_z}. \tag{3.1}$$

Where M is a function of the shortest wavelength in the spectrograph ($\lambda_{\min}$), in order to account for all spatial modes. L_x, L_y and L_z are the lengths of an individual component spectrograph or AWG in the x, y and z direction respectively which will be defined in the next two sections. P=1 and P=2

represent the semi-photonic and photonic cases respectively.

3.4   The semi-photonic IPS (P=1)

The semi-photonic case involves taking an individual spaxel and using a re-arranged PL to form a diffraction-limited slit, which is then dispersed by bulk optics [72].

3.4.1   Model Geometry

Slicing the input of a spectrograph has already been examined theoretically in [76]. The paper took existing instruments and sliced the input, either adding the slices to the length of the slit, or placing them into replica spectrographs. It showed that slicing could result in an instrument with a slightly smaller overall volume, though the instruments sliced to the diffraction-limit were shown to be larger than their counterparts due to the extra components required. This is important to us because we showed that photonic spectroscopy is similar to image slicing to the diffraction limit in section 2.3.3. Since conventional image slicing has already been examined we restrict ourselves to examining only the IPS concept, which takes each individual spaxel (not a number of them) and separates it into a single spectrograph. We will be using the modified model from [76] and adding this to our results. As the input to each spectrograph now depends on the number of modes per spaxel we shall be setting the length of the slit to the number of modes (equation 2.37).

3.4.2   Semi-photonic model limits and Calibration

In order to calibrate the model we use the same method as [76], with the $S=1$ case oversizing using a multiplicative factor and the $S=2$ case oversizing the
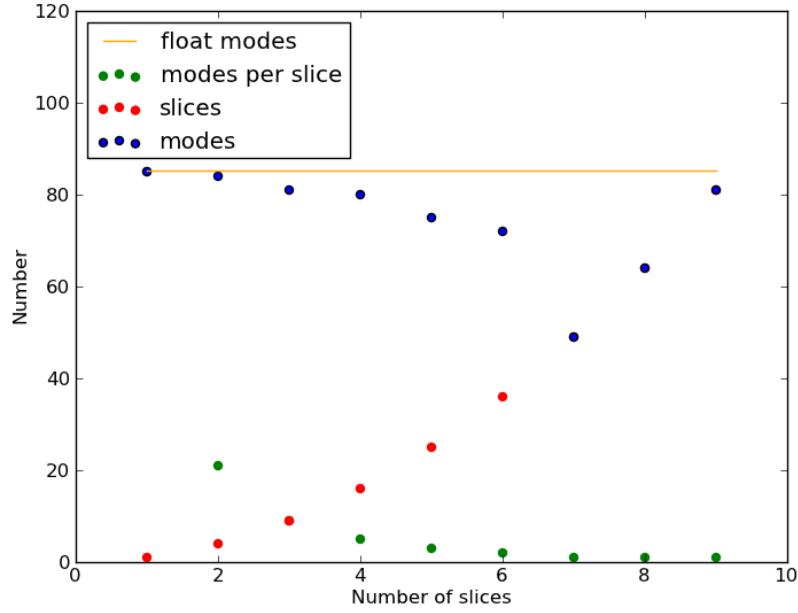
Figure 3.1: An example of the number of modes generated from a single spaxel on an 8m telescope of 0.5" FWHM seeing at λ = 1650nm. Fixing the size of the spaxel to the FWHM gives a single spaxel (here number of slices = 1). This spaxel is large and contains many modes. Slicing the spaxel produces smaller spaxel sizes, but larger numbers of them (the number of spaxels is the slices squared). This results in the same total number of modes in the area (the horizontal yellow line). The variation in the blue is due to the integerisation of modes within individual slices. Note that the three final red points lie under the blue ones.
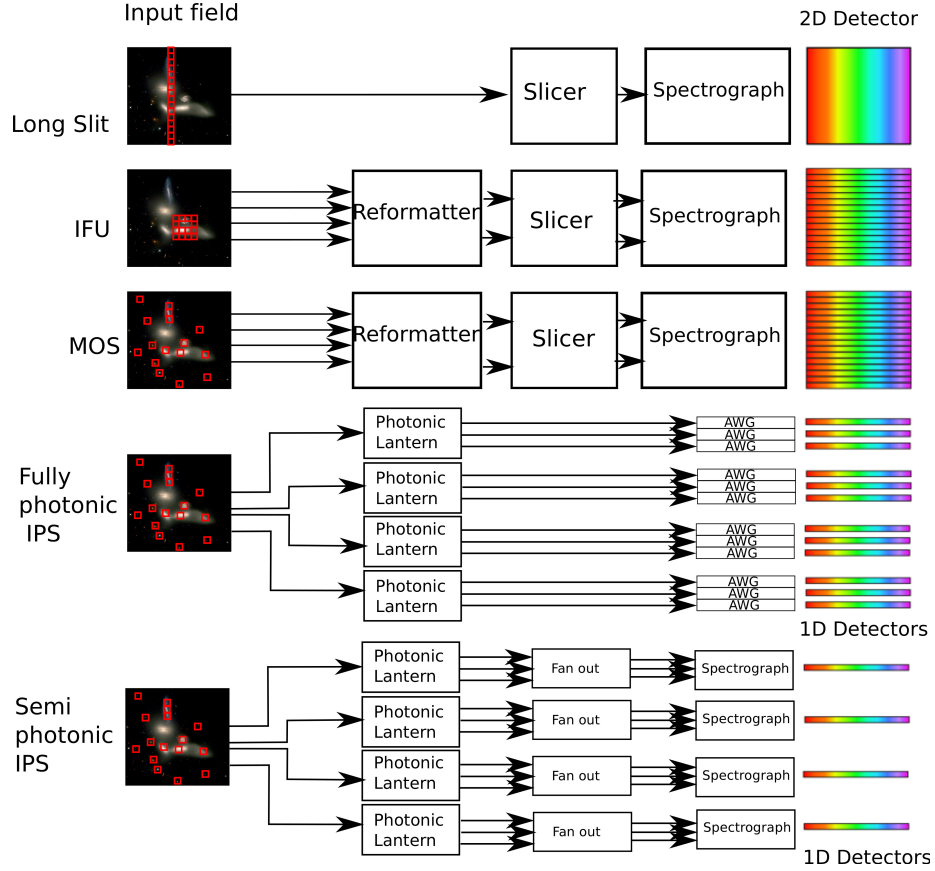
Figure 3.2: An illustration of conventional slicing and Photonic slicing. All methods sample an area of the same size (e.g. the same number of spaxels). The three conventional methods reformat the input and disperse it, producing one spectrum per spaxel. The fully-photonic option takes each input spaxel and splits it into individual modes using a photonic lantern. Each of these modes is fed into an AWG to produce a spectrum. These then need to be recombined and summed to produce the spectrum for the spaxel. The semi-photonic option uses the same photonic lantern, but this is then reformatted into a long slit and fed into conventional spectrographs.

Instrument	S =1		S =2	
	a (m)	b	a (m)	b
GNIRS	0.1	2.1	0.46	1.1
CRIRES	0.1	2.2	0.61	1.1
NIFS (J)	0.1	7.0	0.86	1.1
SINFONI (H)	0.1	7.0	0.86	1.1
IRMS	0.1	8.0	2.06	1.1
IRIS	0.1	10.0	1.46	1.1

Table 3.1: The scaling parameters for the semi-photonic versions of the conventional instruments. The scaling scenarios are described fully in [76] and [17].

spectrograph input beam. The scaling factors for our instruments can be found in table 3.1.

3.5 The fully-photonic IPS (P=2)

For our fully-photonic model we shall concentrate on modelling the size of the AWGs, not the components that feed them. We shall include a factor for our detector sizes.

3.5.1 Model geometry

For the fully-photonic model we first need to consider the geometry of AWGs. These are available in many different variations, especially with respect to the geometry which generates the path difference between waveguides (e.g. S-bend, circular, horse-shoe). To keep the toy model simple we have chosen a reflective AWG [77, 78] using a Rowlands Circle arrangement for the Free Propagation Region (FPR). We have removed the bend at the end of the waveguide array for simplicity. Because of this it looks almost identical to a conventional double-pass Echelle spectrograph.

Using the definitions in figure 3.3 we arrive at the following equations for
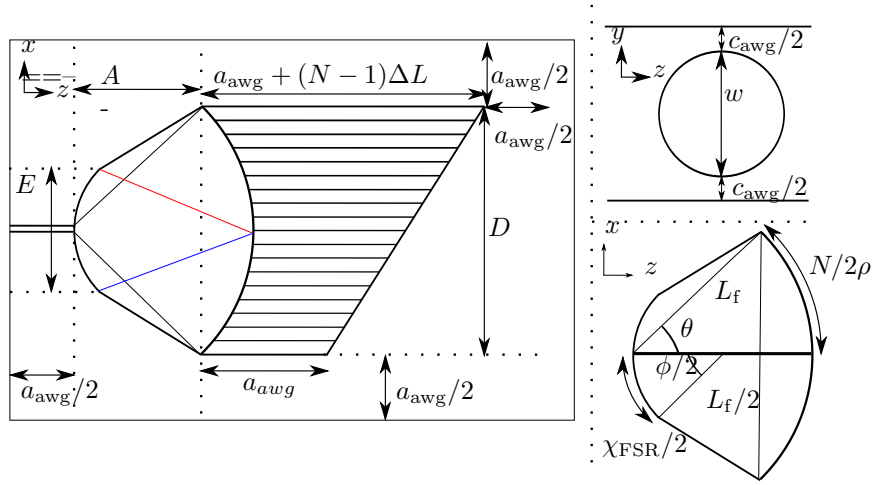
Figure 3.3: The fully-photonic model. The left image shows the x-y view of the AWG, with the (left to right) input fibre, Free Propagation region and waveguides. The top right image shows the side view of the AWG model, with the top and bottom cladding layers and the layer containing the waveguides in the centre. The bottom right image is an enlargement of the FPR which is a Rowlands Circle arrangement.

the size of the AWG model

$$L_x = (\max(D, E) + a_{\mathrm{awg}}) \, b_{\mathrm{awg}} \tag{3.2}$$

$$L_y = (c_{\mathrm{awg}} + W_{\mathrm{i}}) b_{\mathrm{awg}} \tag{3.3}$$

$$L_z = (a_{\mathrm{awg}} + A_x + (N_{\mathrm{wg}} - 1)\Delta L) \, b_{\mathrm{awg}}. \tag{3.4}$$

Here A_x is the x-length of the FPR, ΔL the length difference between adjacent waveguides to achieve the required order for a given central wavelength (λ_c), D is the length containing the waveguides (analogous to the illuminated length of the grating in a standard echelle grating), E the x length of the detecting surface, W_{i} is the waveguide diameter. The oversizing parameters a_{awg}, b_{awg} and c_{awg} parameterise the extra size required to implement a practical device.

First we calculate the appropriate dispersion order, m, in terms of the free spectral range (FSR, $\Delta\lambda_{\mathrm{FSR}}$) for an AWG

$$m = \frac{\lambda_{\min}}{\Delta\lambda_{\mathrm{FSR}}}. \tag{3.5}$$

Setting $D = N_{\mathrm{wg}}/\rho$, this can be combined with equation 2.34 where ρ is the density of waveguides (analogous to the ruling density of a conventional disperser) to give

$$D = \frac{CR}{m\rho}. \tag{3.6}$$

The physical extent of the FSR in an arrayed waveguide grating is $X_{\mathrm{FSR}} = (\lambda_{\min} L_F \rho / n_{\mathrm{s}})$, where n_{s} is the refractive index of the slab and L_F the length of the free space propagation region. Combining with geometrical arguments gives

$$E = L_{\mathrm{F}} \sin\left(\frac{\Phi}{2}\right) = L_F \sin\left(\frac{\lambda_{\min}\rho}{n_{\mathrm{s}}}\right). \tag{3.7}$$

Where Φ is defined in figure 3.3. In order to calculate ΔL we make use of the equation for calculating the central wavelength of the AWG

$$\Delta L = \frac{\lambda_{\mathrm{c}} m}{n_{\mathrm{c}}} \tag{3.8}$$

where n_{c} is the refractive index of the waveguides, the central operating wavelength is $\lambda_{\mathrm{c}} = \lambda_{\min} + \Delta\lambda_{\mathrm{FSR}}/2$, so A_x can be calculated from geometry as

$$A_x = L_{\mathrm{F}} \cos(\theta) = L_F \cos\left(\frac{N_{\mathrm{wg}}}{2\rho L_{\mathrm{F}}}\right). \tag{3.9}$$

where θ is defined in the figure and N_{wg} is calculated using equation 2.34. In order to calculate L_F we make use of the fact that imaging requires the number of detector pixels to be able to adequately sample at the resolution required (equivalent to sampling of the Echelle model in [76]). To do this we take the dispersion relation

$$\left(\frac{\delta\lambda}{\delta x}\right) \simeq \left(\frac{d\lambda}{dx}\right) = \frac{n_{\mathrm{s}}}{L_{\mathrm{F}} m \rho}. \tag{3.10}$$

and combine it with equation 3.5, setting $\delta x = N_0 d_{\mathrm{p}}$, where N_0 is the oversampling and d_{p} is the size of the pixels. We also take the equation for the spectral resolution $\delta\lambda = \lambda_{\min}/R$. Minimising to obtain the maximum L_F we find

$$L_{\mathrm{F}} \geq \frac{n_{\mathrm{s}} N_0 d_{\mathrm{p}} R \Delta\lambda_{\mathrm{FSR}}}{\rho \lambda_{\min}^2}. \tag{3.11}$$

Finally we can calculate the number of pixels we need for the required resolution

$$N_{\mathrm{P}} = \frac{L_{\mathrm{FSR}}}{N_0 d_{\mathrm{p}}} = \frac{\lambda_{\mathrm{c}} L_{\mathrm{F}} \rho}{n_{\mathrm{s}} d_{\mathrm{p}}}. \tag{3.12}$$

3.5.2 Fully photonic model Limitations and Calibration

Astronomical spectrographs are usually designed to operate with a large free spectral range (typically several hundred nm). This is a problem for the IPS because conventional telecoms AWGs are designed with low free spectral range in order to deal with the discrete narrow band input from the telecoms industry. For astronomy, single AWGs need to be redesigned to work in lower spectral orders by reducing the path difference between adjacent waveguides. This requires more waveguides to maintain the maximum theoretical resolution and an increase in L_{F} to maintain a practical one (see eqn 3.11). This produces very large AWG dimensions which cannot be manufactured due to chip manufacturing size constraints [63].

We wish to avoid this problem and retain a fully integrated design with no external optics. As such we make use of the tandem AWG arrangement, where a primary AWG filters the light by wavelength into secondary AWGs, each encompassing a fraction of the original FSR (see figure 3.4 and [79]). This allows the individual component dimensions to be within manufacturing limits whilst allowing our full device to sample the correct FSR. It would also allow the AWG design process to remain similar to current specifications.

Since no fullscale AWG instruments currently exist, we are required to use a bottoms-up approach to estimate its size. To do so we take an existing AWG acquired from Gemfire Livingstone. We use its known parameters and adjust the models produced dimensions until they match the real ones. In order to emulate [76], we set the scaling parameters to two extremes.

S=1 :   Minimise b_{awg}=1.1,which yields a $a_{\mathrm{awg}} = 10$mm
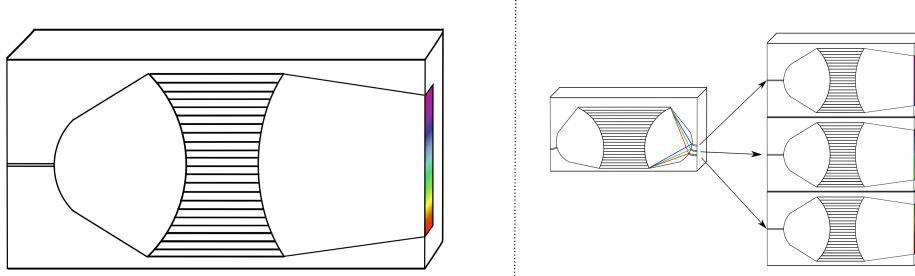
Figure 3.4: An illustration of the tandem and single AWG setup. The image on the left shows the conventional AWG dispersing the whole spectrum. The image on the right is the tandem configuration. The intial AWG (or other dispersive optic) splits the light by wavelength (here to $\Delta\lambda_{\mathrm{FSR}}/3$) and feeds the second set of AWGs. This has the advantage that each individual AWG can be smaller, though it requires more AWGs, additional components (feeding fibres) and is subject to extra loss of throughput which makes current devices unviable (see chapter 5). Note that the length of the output must be the same in both cases in order for the detector to sample adequately.

S=2 : Minimise $a_{\mathrm{awg}} = 0$mm, which yields $b_{\mathrm{awg}} = 2.8$

For both scenarios we keep $c_{\mathrm{awg}} = 0.7$mm as the device is planar so the height should not change.

For simplicity we will not include the volume of the initial multimode fibre bundle, the photonic lantern or the housing of the instrument. We will however include an estimate for the size of the detector. This value is calculated assuming the size of a typical detector sub-system including the cryostat. This is estimated as 10^{-7}m^3 per detector pixel , using the GNIRS detector as a guide [80].

3.6 Results

To estimate the uncertainties within our model, we use both of our oversizing options for both models and also vary C between 1 (diffraction-limited) and 4 (the initial results obtained in [3]) for our fully-photonic instrument. This gives

us two extremes and allows for the current maximum of $C = 1.6$ achieved in [5].

To test our models we choose two sets of instruments. First those designed to represent current instrumentation on 8m telescopes. Then we test against instruments that have been designed for the TMT. We shall only investigate a single mode of operation for each instrument which is the case for many survey and high precision facilities, though may be oversimplifying for our instrument choices as they are designed to operate at different resolutions and at different wavelengths by changing gratings or optics. It however keeps the model simple and IPS devices could be adapted to suit various purposes, this is discussed in the conclusions.

The first set of instruments are in current use on 8m telescopes and are intended to represent generic instrument types. We use the parameters in table 3.2 to calculate the volume of the instruments. The instruments we have chosen are:

1. Gemini Near InfraRed Spectrograph (GNIRS) on Gemini-North. The instrument has an overall wavelength range of 1.0-5.4µm, resolutions of between 1,700 and 18,000 and slit widths of between 0.1 and 1.0 arcseconds. It has an imaging mode, a long slit mode and originally an IFS mode (destroyed during maintenance at the telescope). We will be comparing our photonic instrument to the long slit configuration.

2. CRyogenic high-resolution InfraRed Echelle Spectrograph (CRIRES) is a high resolution spectrograph on the Very Large Telescope (VLT). It is designed to operate between 1.0-5µm, with a resolution of up to 10^5. We have chosen it to illustrate a long slit high resolution spectrograph.

3. Near-Infrared Integral Field Spectrometer (NIFS) on Gemini-North is our first IFU instrument. It is designed to work with the Adaptive Optics system, over 0.9-2.4 µm.

4. Spectrograph for INtegral Field Observations in the Near Infrared (SIN-FONI) on the VLT is our second IFU instrument. It operates in the 1.1 to 2.45µm range again with AO.

We have also chosen two hybrid instruments proposed for the Thirty Meter Telescope [81]. IRMS will employ 10 or more IFUs. Each one will have a 2 x 2 arcsecond squared field of view with 50% of the energy enclosed by 50 mas at wavelength of 1µm, resulting in 1600 spaxels per IFU. IRIS has 3 IFU units, two of which will be lenslet arrays (for observing smaller fields) and one will be an image slicer (larger fields). Here we model the slicer, which has 88 mirror facets, but will keep the best resolution possible with our AWG model. As with the 8m instruments , the instrument scale lengths are fitted to values taken from the literature, see table 3.2.

Table 3.3 shows the resulting parameters in the fully-photonic case. The total number of AWGs required are shown in the second column, this number will be in the tens of thousands for 8m instruments and the hundreds of thousands for the 30m instruments. The large number of AWGs requires rigorous quality control to test the large number of individual components. This may be of advantage though, as the individual AWGs should be less prone to flexure and, due to their modular nature, are better suited to mass production and upgrades and expansion to suit cashflow. Note that the size predictions do not include provision for mounting hardware required to support the instrument components or to provide a suitable controlled environment.

The next eight columns show the different resulting normalised scale lengths of the instrument. Note that this is the scale length of the overall instrument, not the individual components. The first four are the scale lengths without provision for the detector size and show that the total size of the 8m instruments will be on the same order as the conventional instrument. If the diffraction limit

Instrument	χ ('')	$N_y (N_x) [N_{IFU}]$	Total Spaxels	R	λ_c (nm)	$\Delta\lambda_{FSR}$ (nm)	ρ (mm^{-1})	Vol (m^3)
GNIRS	0.3	330(1)	330	5,900	1,650	400	31.7	2.00
CRIRES	0.3	200(1)	200	100,000	1,650	48	31.6	3.00
NIFS (J)	0.1	30(29)	870	6,050	1,250	600	600	2.75
SINFONI (H)	0.2	32(32)	1,024	3,000	1,650	400	128.57	2.75
IRMS	0.1	40 (40)[10]	16,000	10,000	1,200	400	128.57	16.00
IRIS	0.1	60(60)[1]	4,000	8,000	1,200	400	310	55.00

Table 3.2: Table of input parameters all instruments. Symbols except for N_{IFU}, the number of IFUs in the instrument, are explained in the text. The numbers are taken (and approximated from) [76] for GNIRS, [82] for CRIRES, [83] for NIFS, [84] for SINFONI, [85] for IRMS and [49] for IRIS.

Instrument	Total number of AWGs	Normalised Scale length							
		No detector				With detector			
		$C=1$		$C=4$		$C=1$		$C=4$	
		$S=1$	$S=2$	$S=1$	$S=2$	$S=1$	$S=2$	$S=1$	$S=2$
GNIRS	13,000	0.49	0.87	1.46	1.55	0.51	0.89	1.47	1.55
CRIRES	6,300	0.50	0.90	1.19	1.32	0.60	1.09	1.22	1.42
NIFS	8,900	0.79	1.45	1.66	1.93	0.80	1.46	1.66	1.93
SINFONI	28,000	0.39	0.64	1.36	1.39	0.39	0.66	1.36	1.39
IRMOS	520,000	1.69	3.08	3.53	4.09	1.71	3.11	3.53	4.11
IRIS	110,000	0.72	1.07	1.34	1.48	0.73	1.08	1.35	1.49

Table 3.3: Table of the resulting scale lengths of the respective fully-photonic instruments. The total number of modes in the whole instrument is shown first, with the next four columns showing the respective sizes for the model with no detector. This is followed by the model with detector. All of the scale lengths are normalised to the cube root of the volume in table 3.2. The AWG model uses a waveguide separation of $\rho = 200\text{mm}^{-1}$.

Instrument	Modes per spaxel	Total detector pixels $/(10^6)$	Reference Instrument pixels $/(10^6)$
GNIRS	39	60.69	1.05
CRIRES	31	47.31	2.10
NIFS	10	112.43	4.19
SINFONI	27	66.50	4.19
IRMOS	32	6263.44	83.89
IRIS	32	1127.42	16.78

Table 3.4: Further information on the fully-photonic model. The AWG model uses a waveguide separation of $\rho = 200 \text{mm}^{-1}$.

Instrument	Number of replica Spectrographs	Normalised Scale Length S = 1	Normalised Scale Length S = 2	Number of detector pixels* $/(10^6)$
GNIRS	330	4.30	5.30	1.05
CRIRES	200	3.06	4.66	2.10
NIFS	870	9.55	9.54	4.19
SINFONI	1,024	8.62	9.36	4.19
IRMOS	16,000	26.07	32.48	83.89
IRIS	3.600	8.49	9.20	16.78

Table 3.5: Results for the semi-photonic model. All of the scale lengths are normalised to the cube root of the volume in table 3.2. The semi-photonic model uses ρ stated in figure 3.2. * The number of detector pixels assumes that the modes in each spaxel can be reduced onto the detector appropriately, which may not be the case.

can be achieved the resulting instruments are smaller for all scenarios, with the exception being NIFS with the $S{=}2$ scaling. If the diffraction-limit cannot be achieved the instruments will have a scale length larger than the original instruments. The results for the 30m instruments are similar to the 8m ones, with the $S{=}1$ scaled case of IRIS being slightly smaller and the rest being slightly larger.

The second four include the provision for detector and show similar results, though the scale lengths are increased slightly as expected. This shows the size of the additional detector pixels (discussed later) will not pose a significant size restriction on the instrument.

Table 3.4 shows the results corresponding to the number of modes per spaxel and hence the requirements in terms of detector pixels. The second column shows that all of the instruments will have around 30 modes per spaxel, with the exception of NIFS, which will have 10. This causes problems with oversampling in the fully-photonic model due to each mode needing to be sampled using two detector pixels per resolution element (Nyquist sampling). There needs to be some way of combining the individual spectra to stop massive oversampling (shown in column 3). This will be discussed later, but will probably involve additional components, increasing the size of the instrument.

Table 3.5 shows the results from the semi-photonic model. The second column shows that the number of replica photonic instruments will be 10^3-10^4. As a consequence using the semi-photonic method will require mass production of the replica spectrographs which is not common in the astronomical instrumentation community. The alternative is to put many spaxels in the same spectrograph and would require a balance between redundancy and over-large components for this version is to work.

The next two columns show that using the semi-photonic model for the in-

strument will result in much larger instruments. This matches with the results of [76], where as the input was sliced more the instrument tended to get bigger. As stated in section 3.4 we are slicing the instrument to the diffraction-limit in the spatial direction and then separating each spaxel into a separate spectrograph, which imposes huge redundancies. The number of required detector pixels are shown in the final column. For this we are assuming that all the detector separate modes can be combined onto a linear detector, however this may not be possible.

3.7 Modifications to Integrated Photonic Spectrographs

From the results already discussed, it is clear that IPSs in their current state offer little or no advantage in terms of size and detector pixels when compared with existing instruments on large telescopes or those planned for ELTs. However it is possible to envisage modifications to the fully-photonic device which would make it possible to exploit the unique features of photonic spectrographs. One such scheme is already being studied [5].

3.7.1 Multiple-input Arrayed Waveguide Gratings

So far we have restricted ourselves to one input per AWG (i.e. one mode per AWG), which as shown in previous sections requires many AWGs. Placing multiple inputs per AWG would reduce the dependence on equation 2.37, at the extreme eliminating it entirely if all the inputs could fit into a single AWG. In order to introduce these extra inputs additional fibres are placed at different positions on the input FPR. This introduces a path difference between each input with respect to the central one (see figure 3.5 and 3.6). This path difference
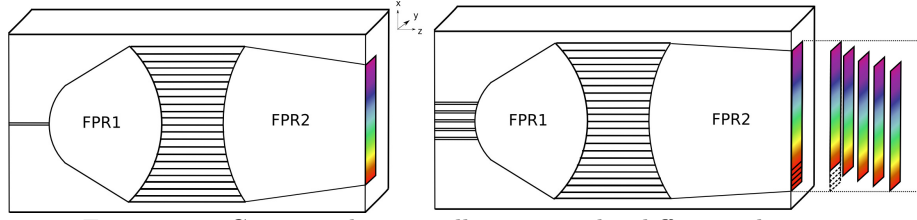
Figure 3.5: Cutaway diagram illustrating the difference between the single and multiple input versions of the AWG. To the left is the single input, which would make use of a linear detector array to sample the output spectrum. To the right the multiple input version. Here five inputs produce five separate spectra that overlap at the output of the AWG. This has a couple of implications, first the spectra would need to be cross dispersed in order to be sampled and second the end of the second FPR would need to be larger (though not the input which would remain the size of the waveguides). The path difference in the waveguides is not illustrated in this diagram for simplicity.

is carried through the system and results in the output spectrum of each mode being shifted in the dispersion direction at the output. To remove the overlap between spectra, it will be necessary to introduce cross dispersion.

The AWG also produces multiple diffraction orders (as with a conventional grating) so we also need to make sure the inputs all lie within a region half that of the FSR of the central input. This is to stop the same wavelength from different orders lying in the same position in the linear output, resulting in the cross dispersed spectra lying the same position on the detector. The refractive index change in fused Silica is not great enough to disperse the light by polishing the AWG at an angle. In order to separate the spectra, the outputs need to be cross-dispersed using conventional optics [3] . This means that each AWG will need a two-dimensional detector, a dispersive element and collimating and camera lenses. Here we look at the relative advantages of using cross dispersion in the system. Note we do not discuss energy resolving detectors, which would eliminate the need for cross dispersion here, please see chapter 5.
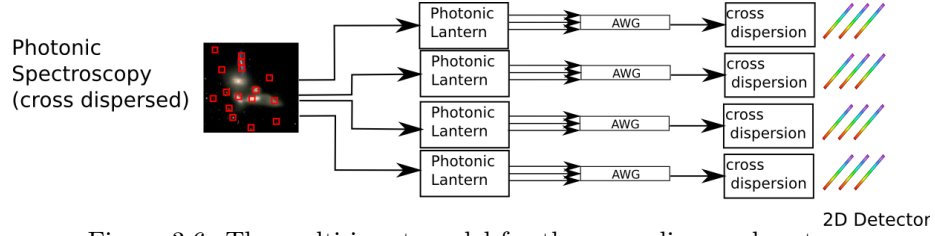
Figure 3.6: The multi-input model for the cross dispersed system. Each spaxel from the input field is fed into a photonic lantern. The output SMFs are fed into AWGs, with multiple fibres in each AWG. The output from these AWGs is then cross dispersed onto a 2d detector.

3.7.2   Adding cross-dispersion

To cross-disperse we need additional optics, which means that the device is no longer fully integrated, potentially making manufacture and maintenance more difficult, but reducing the number of AWGs required for the device. We construct a new toy model to see how the scale length of a cross dispersed system (multiple inputs) compares to one with linear arrays (single inputs). For this section we have modified our fully-photonic model so it is no longer reflective and the output of the second FPR outputs is linear (e.g. figure 3.5 and [86]). The first FPR is still in its original shape so as to allow the multiple inputs. Changing the model like this will affect the overall size of the instrument (due to the difference in AWG design), but will still allow us to examine the relative sizes of the two scenarios.

We retain the single input model for our comparison and use the length values calculated in previous sections. As such the scale length of the instrument (with all modes) is still $N_{awg}L_xL_yL_z$, where N_{awg} is the number of AWGs.

The cross dispersion option requires the AWG, a collimator, prism and then camera in front of the detector (see figure 3.7). The equation for the volume of the system now becomes $N_{awg}L_xL_yL_z$, where $N_{awg} = N/N_i$, the total number

of spaxels divided by the number of inputs per AWG and the dimensions being defined below.

We start by examining the output end of the AWG. For a single input the x length of the AWG system would be the same as described in equation 3.2, E will now be X_{FSR} as we have flattened out the output. Adding extra inputs such as the ones illustrated in figure 3.7 will increase this x length. The maximum distance between inputs must be less than X_{FSR}, to avoid the same wavelength in two different orders lying on the same position. For simplicity we assume evenly spaced inputs, which when combined with the previous condition yields equation 3.19. We set the maximum number of inputs to be X_{FSR} / D_{input}, where D_{input} is the diameter of the input fibre (here set to 125µm, which is the diameter of a single mode fibre).

To calculate the y length, we must consider how the spectra are to be cross dispersed. We need to make sure that the output beam from the system is collimated. To do this we make sure the output angle of the collimator is small: $\theta_2 = W_{\text{i}}/ 2f_1 < 0.01^0$. Where θ_2 is the divergence in the collimator and f_1 is the focal length of our collimator. As our system is diffraction-limited, the diameter of our collimated beam is

$$D = \theta_1 f_1 \approx \left(\frac{\lambda_{\text{max}}}{W_{\text{i}}} \right) f_1 \tag{3.13}$$

For cross-dispersion we use a prism, athough a grating could also be used. We need to work out the required resolution of the prism, which is proportional to the number of inputs (e.g. as the number of inputs increases the FSR decreases by that factor). This gives

$$R_{\text{x}} = \frac{N_{\text{i}} \lambda_{\text{min}}}{\Delta \lambda_{\text{FSR}}}. \tag{3.14}$$

where R_x is the resolution of the cross dispersed system. We can then combine this with the equation for the resolving power of a diffraction-limited prism [22] to yield

$$t > R_\mathrm{x} \left(\frac{d\lambda}{dn} \right) = \left(\frac{N_\mathrm{i} \lambda_\mathrm{max}}{\Delta \lambda_\mathrm{FSR}} \right) \left(\frac{d\lambda}{dn} \right). \tag{3.15}$$

where t is the path difference between the upper and lower rays in the prism. In order to account for all wavelengths we must use the maximum value of the material dispersion, $d\lambda/dn$ within the required wavelength range. The vertex angle of the prism is

$$\alpha = \arcsin \left(\frac{2D}{nt} \right). \tag{3.16}$$

where α is the angle the prism makes to the collimated beam and n is the refractive index of the prism. This allows the calculation of the vertex angle of the prism

$$\kappa = 2 \arcsin \left(\frac{t}{2D} \sin \alpha \right). \tag{3.17}$$

The output angle of the prism is then

$$\beta = \pi - \kappa - 2\alpha. \tag{3.18}$$

We can then calculate L_y from figure 3.7, giving equation 3.20. Finally from above and from the geometry in figure 3.7 we have
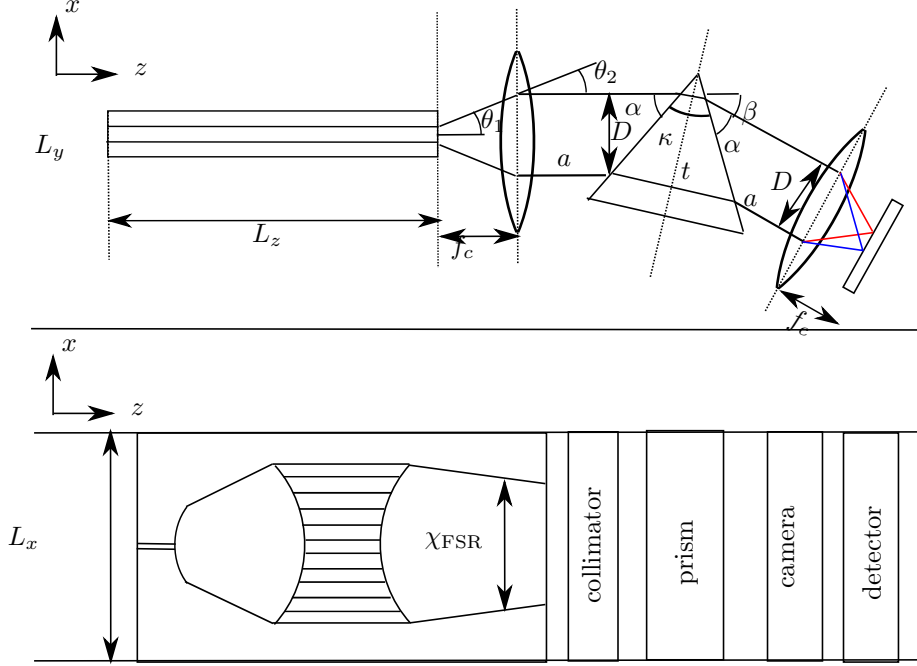
Figure 3.7: The new model for the AWG. This allows multiple inputs to the AWG and includes cross dispersion at the output in order to separate overlapping spectra.

$$L_x = MAX\left(X_{\mathrm{FSR}}\left(\frac{2N_{\mathrm{i}}-1}{N_{\mathrm{i}}}\right),D\right) + 2a_{\mathrm{awg}} \tag{3.19}$$

$$L_y = \frac{D}{2} + t\sin\delta + a\sin\beta + MAX\left(f_1\sin\beta,\frac{D}{2}\right) \tag{3.20}$$

$$L_z = L_z + f_1 + a + t\cos\delta + (a+f_1)\cos\beta. \tag{3.21}$$

Here $\delta = (\alpha + \beta)/2$.

3.7.3   Results for cross-dispersed multiple-input AWG

We now run the simulation for all the instruments detailed in section 3.6 using the model above and fused silica as the glass in our prism. We also set the

maximum value of t to 30cm, to represent sensible limits for the prism size.

By imposing our limit on t we can see in figure 3.8 that the number of inputs per chip is limited to the tens for all the resulting graphs due to equation 3.15. The potential advantage of this is all the resulting modes from a single spaxel could be fed into one AWG, meaning each one could be isolated.

We can also see that though the instrument size decreases (particularly for NIFS, IRMS and IRIS) as more inputs are added all instrument sizes will be much larger than the single input version. Existing results have only put around 10 inputs on a chip and then cross dispersed by the IRIS2 instrument [5], which fits with our results. There is no result for CRIRES as the prism would have to be too large to have sufficient resolution.

Not shown in the resulting graphs are the numbers of pixels required for the instruments, which would be of the same order or greater for this new setup.

It should be noted that we have used a prism in our example, which is usually used for lower resolution cross dispersion. The alternative is to use a grating, though this would work in a similar way. Taking the equation for FSR and combining it with a diffraction-limited grating ($R_x = m\rho W$) yields

$$N_i = \rho W. \tag{3.22}$$

This shows the grating size (related to W) will increase as the number of inputs increases (given a maximum ruling density).

3.7.4 Other instrument options

In its present form it is clear that trying to compete with large IFU style instruments is not a viable option. As shown in [17] the areas providing the greatest advantage would be small or diffraction-limited telescopes, preferably operating at longer wavelengths with instruments that only require a small field of view.
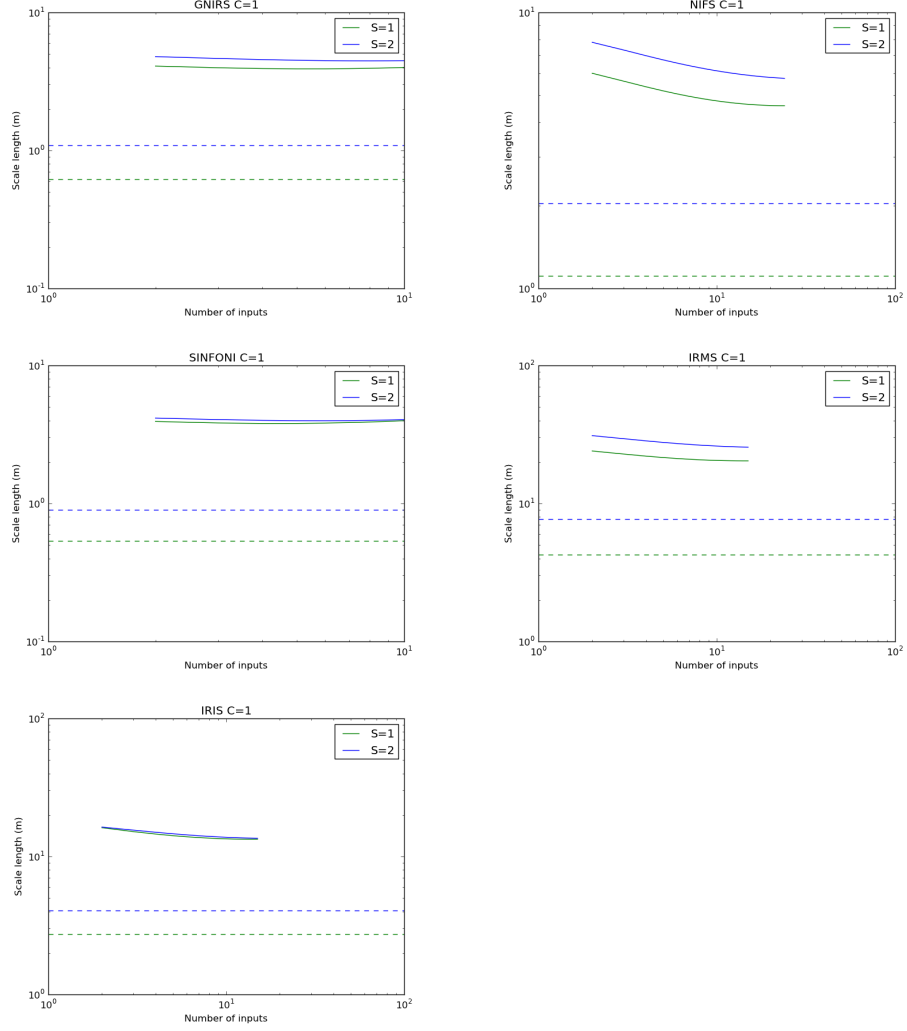
Figure 3.8: The resulting scale length due to varying the number of inputs to each AWG on each instrument. The different scaling cases are show in green and blue with the dashed horizontal line indicating the scale length of the single input instrument. From the figure you can see that all the results will produce larger instruments than the single input case. The result for CRIRES is omitted as no sensibly sized prism could be found with sufficient resolution to cross disperse the outputs.

There is potential for applications in solar system science, planetary and stellar science and studies of individual stars in galaxy populations

Another option is to use multiple single-input AWGs, but to combine the output onto a single linear detector array to reduce the number of detector pixels by a factor equal to the number of modes per spaxel. This would greatly reduce the cost of the detector system and bring the benefit of adaptability of a one-dimensional detector array to the output focal surface of the AWG. This would only be possible if the pixels had a large aspect ratio. This might incur a penalty in terms of extra detector noise if the area of the pixel was increased, as dark current scales with the volume of the detector pixel [87]. In addition the number of AWGs is not reduced. This option is currently under investigation [88], though no references were found for arrays currently under development.

A further option is to reduce the number of modes that are extracted from the input multimode light to produce an acceptable tradeoff between cost and performance defined as a combination of throughput, spectral resolution and field size. Options include :

(a) Restrict the number of single-mode fibres output from the photonic lantern with a consequent loss of throughput. This may be acceptable because the population of excited modes is not likely to be uniform [75] but will reduce as a function of mode number to a cutoff value at high order. Thus the overall performance of the system in terms of the product of cost and throughput may be acceptably high.

(b) Reduce the number of AWGs (and detector pixels) by making each work in a partly multimode (i.e. few mode) configuration so that the AWG disperses light which is not in a single mode. This is explored in chapter 5. This may be acceptable if high resolving power is not required e,g, in a survey of faint, unresolved galaxies.

(c) Reduce the number of AWGs (and detector pixels) by decreasing the field of view. This directly trades-off cost with field coverage. This is of relevance to applications requiring little spatial multiplex, e.g. single-object spectroscopy or spectroscopy with high-order adaptive optics such that the input image is already near the diffraction limit [17].

3.8   Conclusion

We have examined the application of Integrated Photonic Spectrographs in astronomy and shown that an IPS is equivalent in function to an image slicer. We have shown that as the telescope diameter increases, the size of an IPS must also increase (provided the system is slit, not aberration limited and that the slit is not matched to the diffraction-limit) due to the increase in number of modes in the field (equivalent to the number of diffraction-limited slices). We have also shown that the number of modes in a field is independent of how the field is initially sampled (the size of the sampling element (spaxel) has no effect on the total number of modes in the field).

We modelled IPS instruments to compare them with conventional instruments on large telescopes and found that they require 10^3-10^5 single input Arrayed Waveguide Gratings (AWGs) or 10^3-10^4 replica spectrographs if bulk optics are used for instruments on 8m and 30m telescopes. We found that fully-photonic instruments were comparable in size to their conventional counterparts but only if the AWG was close to the diffraction limit. The semi-photonic instruments were found to be much larger, due to the redundancies of having multiple spectrographs.

We have also found that unless the input image is sampled near the diffraction limit, the number of component spectra in each spaxel is very high, requiring large numbers of pixels in the detector array (assuming the device is read noise

limited, with square pixels) . This is equivalent to oversampling the PSF and could also potentially increase detector noise in the instrument. Constructing detectors with rectangular pixels is being investigated [88], though no references were found in the literature of their construction.

To combat the problem of size we considered the effect of adding extra inputs to the AWG to reduce the number of AWGs required. However the resulting instrument was of the same size or larger. It also means that the problem of oversampling in the linear case remains unsolved and potentially will be worse since the spectra will need to have gaps between them to distinguish them.

We also examined other options for reducing the number of detector pixels and/or AWGs and concluded that instruments of photonic construction may be viable depending on the extent to which performance (including throughput, spectral resolution and spatial multiplex) can be traded against cost.

Chapter 4

Parameters and Science Cases for the IPS

4.1 Introduction

In Chapter 3 we compared models of the IPS with equivalent models based on conventional instrumentation. We found that for these models the IPS would have a similar or larger volume and require more detector pixels to adequately sample the resulting spectra. In this chapter we reuse our IPS model and add a model based upon that developed in [76]. We use the scaling parameters for GNIRS [89] and the AWG device to fix our models for conventional and photonic instrumentation. We choose GNIRS as it is representative of an existing facility-class instrument in the wavelength range that our AWG was developed for. We examine the results of varying the spectral resolution (R), Field of View (FOV) or number of spaxels (N), telescope diameter (D_T) and the seeing of the telescope (χ) in order to ascertain where an IPS could be most useful within astronomy. We then examine the science cases that fit the best results of the

extended model by comparing them to the results of the ASTRONET report on Europe's 2-4m telescopes over the decade to 2010 [90] and the ReSTAR report from the committee for Renewing Small Telescopes for Astronomical Research [91]. The model in this chapter is adapted from [17].

4.2 The echelle Model

The echelle model is adapted from that shown in [76]. Here we will be calculating the model using the initial input parameters of χ, R, λ_c, $\Delta\lambda_{FSR}$, N_y and ρ. As stated in [76] modelling a spectrograph for monochromatic light is simple, but for a large wavelength range we need to add in extra parameters accounting for dispersion. For our model here we use $\pm\Phi/2$ to represent the extra beamspread due to the wavelength dispersion and $\pm\Psi/2$ to represent the dispersion due to conservation of etendue. Note for our model we are assuming aberration free optics, which would increase the size of the instrument. Although this is taken into account using the scaling parameters for the fixed model, it becomes an approximation as the model parameters are varied. Our toy model is based on an echelle spectrograph with double pass construction (see figure 4.1). For an unsliced spectrograph its dimensions are estimated as

$$L_x = (D_{\mathrm{col}} + \Phi (a_{\mathrm{ech}} + D_{\mathrm{col}} \tan\gamma) + a_{\mathrm{ech}}) b_{\mathrm{ech}} \qquad (4.1)$$

$$L_y = (D_{\mathrm{col}} + \Psi (a_{\mathrm{ech}} + D_{\mathrm{col}} \tan\gamma) + a_{\mathrm{ech}}) b_{\mathrm{ech}} \qquad (4.2)$$

$$L_z = (D_{\mathrm{col}}F_{\mathrm{c}} + D_{\mathrm{col}} \tan\gamma + 2a_{\mathrm{ech}}) b_{\mathrm{ech}}. \qquad (4.3)$$

Where D_{col} is the diameter of the collimated beam, γ the blaze angle and F_{c} the focal ratio of the collimator and camera. We include a_{ech} and b_{ech} as an oversizing parameter in order to allow the model to be fitted to existing
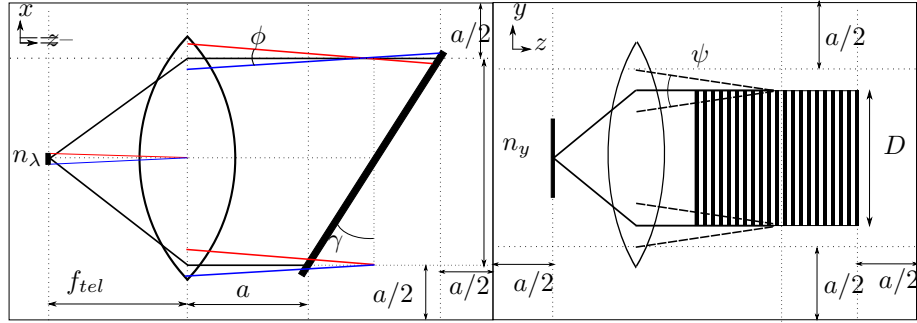
Figure 4.1: The echelle model. The left part of the image shows the spectra dispersion of the echelle model, and the right part shows the spatial extent of the device. This is identical to the one described in [76]

instruments, with a_{ech} as the additive term and b_{ech} the multiplicative. We consider Littrow configuration at blaze, so we can re-arrange equation (2.12) to give the diameter of the collimated beam

$$D_{\mathrm{col}} = \frac{R\chi D_{\mathrm{T}}}{2\tan\gamma}. \tag{4.4}$$

The blaze angle in Littrow configuration is $\sin\gamma = \frac{\rho\lambda_{\mathrm{c}}m}{2}$, and the FSR of a system is $\Delta\lambda_{\mathrm{FSR}} = \frac{\lambda_{\mathrm{c}}}{m}$. Thus

$$T = \tan\gamma = \tan\left(\sin^{-1}\left(\frac{\rho\lambda_{\mathrm{c}}^2}{2\Delta\lambda_{\mathrm{FSR}}}\right)\right). \tag{4.5}$$

To work out the spatial beamspread we use conservation of etendue, yielding

$$\Psi = N_y\chi\frac{D_{\mathrm{T}}}{D_{\mathrm{col}}}. \tag{4.6}$$

We now work out Φ, using the FSR and λ_{c}. In order to calculate the total angle occupied on the detector by the spectrum we use the grating equation $\sin(\theta_{\mathrm{i}}) + \sin(\theta_{\mathrm{o}}) = m\rho\lambda$. Setting $\theta_{\mathrm{i}} = \gamma$ gives

$$\Phi = \theta(\lambda_{\mathrm{max}}) - \theta(\lambda_{\mathrm{min}}). \tag{4.7}$$

Where λ_{max} and λ_{min} are the maximum and minimum wavelengths that the system operates at $(= \lambda_{\mathrm{c}} \pm \Delta_\lambda/2)$. In order to find the minimum focal length for our system we need to make sure we can resolve each point in our spectra. We know that $\chi F_{\mathrm{c}} D_{\mathrm{T}} = n_0 d_{\mathrm{p}}$, where n_0 is the oversampling of the detector (we use 2.5 allowing for a non-gaussian shape in the PSF) and d_{p} is the size of each pixel (here we choose 13.5µm). From this we can calculate the minimum focal ratio of the camera F_{c}.

With all this in place we can rewrite the equations for the scale lengths of the instrument as

$$L_x\left(\chi\right) = \left(\frac{R\chi D_{\mathrm{T}}}{2T} + \Phi\left(a_{\mathrm{ech}} + \frac{R\chi D_{\mathrm{T}}}{2}\right) + a_{\mathrm{ech}}\right) b_{\mathrm{ech}} \tag{4.8}$$

$$L_y\left(\chi\right) = \left(\frac{R\chi D_{\mathrm{T}}}{2T} + \Psi\left(a_{\mathrm{ech}} + \frac{R\chi D_{\mathrm{T}}}{2}\right) + a_{\mathrm{ech}}\right) b_{\mathrm{ech}} \tag{4.9}$$

$$L_z\left(\chi\right) = \left(\frac{R\chi D_{\mathrm{T}}}{2}\left(\frac{F_{\mathrm{c}}}{T} + 1\right) + 2a_{\mathrm{ech}}\right) b_{\mathrm{ech}}. \tag{4.10}$$

Finally to correctly sample the output we require one sampling point in the spatial direction (as we have fixed our slit to the FWHM already) and n_0 samples in our spectral direction, yielding

$$N_{pixels} = n_0 N_y N_\lambda = \frac{\Delta\lambda_{\mathrm{FSR}} n_0}{\Delta\lambda} = \frac{\Delta\lambda_{\mathrm{FSR}} R n_0}{\lambda_{\mathrm{min}}}. \tag{4.11}$$

4.3 Model Results

We set the input parameters in Table 4.1 to represent GNIRS [89]. We then vary resolution, field of view (FOV) of the instrument, telescope diameter and seeing.

χ	Slit Length	D_{T}	R	λ_{c}	$\Delta\lambda_{\mathrm{FSR}}$	Vol	F_{tel}	S	a	b
(")	(")	(m)		(nm)	(nm)	(m^3)	(m)		(mm)	
0.3	99	8	5900	1650	400	2.00	4.8	1	100	1.2
								2	200	1.1

Table 4.1: Table of input parameters for GNIRS calibration, taken from [76] and calculated using the model. These will be used as the default parameters for the models.

The results of the modelling are presented in graphical form in figures 4.3 to 4.10.

Figure 4.3 shows that varying the spectral resolving power will produce instruments with similar scale lengths for all models, with the IPS instrument being slightly larger for existing technologies. The figure shows that as the resolution is increased the instruments become more similar in size, and further increases in resolution will produce instruments smaller than echelle instruments. This may not be possible due to manufacturing restrictions on the AWG. For example most AWG chips can only be manufactured up to 8 inches and as resolutions are increased the manufacturing tolerances become more stringent.

In figure 4.4 we see that using instruments with higher spectral resolution results in a constant additive factor to the number of detector pixels. This suggests that spectral resolution will not be a major factor in deciding whether IPS instruments will be of use.

Figure 4.5 shows the size of the IPS instrument will be smaller than conventional instrumentation for a small FOV. This is due to the beam spread of the echelle being larger than the planar AWG. When the FOV is increased the added volume due to the beam spread increases slower than the added volume due to the extra AWGs. This means at some point the increase in FOV will make the IPS instrument larger than the echelle. This effect is illustrated in

figure 4.2.

Figure 4.6 shows once again the number of detector pixels on the IPS instrument becomes larger as the FOV increases, but this is at the same rate as the echelle instrument. This means the field of view is unlikely to be a deciding factor in whether the IPS will be of use.

Figure 4.7 suggests increasing the size of the telescope will make the IPS model larger than the conventional one. This means the same size issues will be present for IPS instruments as conventional ones for ELTs using the model setup.

We also see from figure 4.8 that increasing the telescope diameter results in the number of pixels increasing with a squared relationship (see equation (2.37)), Suggesting a smaller telescope would be better for the IPS instrument.

Figure 4.9 suggests that the relative sizes of the instruments are dependent on seeing. This is due to the number of modes increasing the number of detector pixels required by the instrument. This suggests a near diffraction-limited input would be best for the IPS.

Figure 4.10 shows the number of detector pixels is comparable for diffraction-limited inputs, but increases hugely as the seeing becomes worse, again due to the extra modes (see Equation 2.37). This suggests a near diffraction-limited input would be best for the IPS.

4.4   Model Conclusion

We find that the IPS model will be similar in size for all cases, though becoming smaller when the FOV of the instrument is small or when the resolution is high. The latter is potentially interesting provided the instrument can be manufactured, as no devices currently exist in this regime. This fits well with the results of chapter 3. We also find this problem will be compounded for
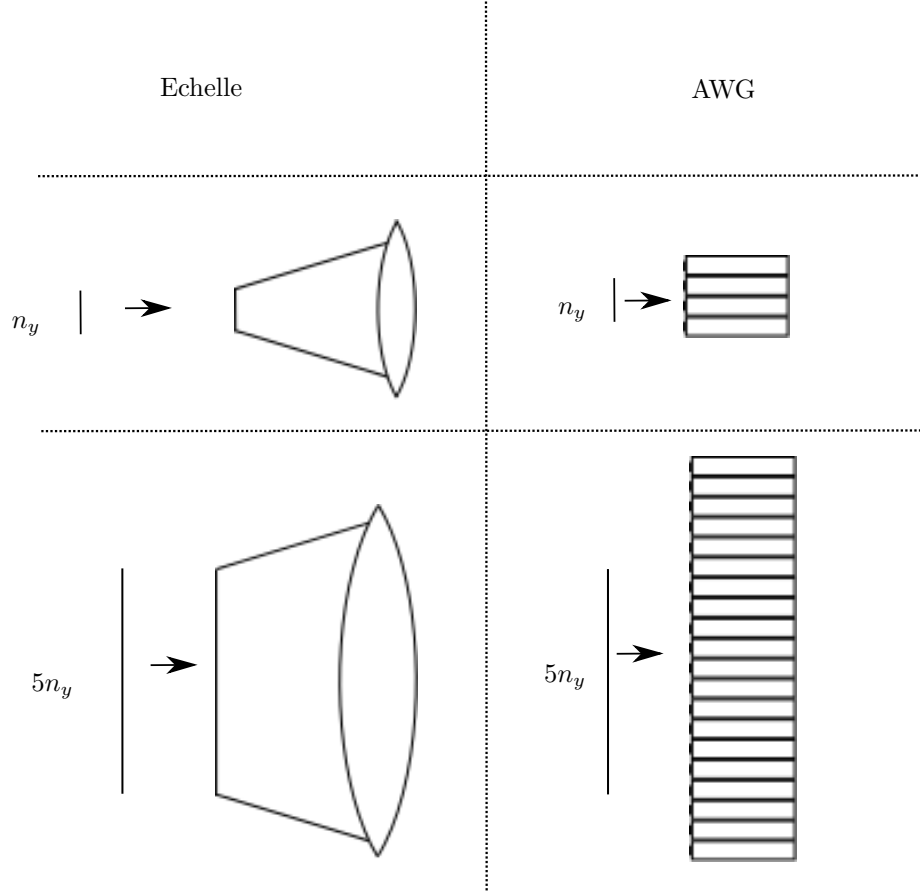
Figure 4.2: An example of changing the slit length of the different model instruments. When the slit is small (in this example of length n_y) the echelle instrument is larger. This is because the divergence of the light (and hence the size of the optic required to collimate it) is greater than the width of the AWG device. As the length of the slit increases the size of the optic increases, though much more slowly than the size of the AWG stack. Eventually this leads to the IPS instrument becoming larger than the echelle instrument (here for a slit length of $5n_y$).
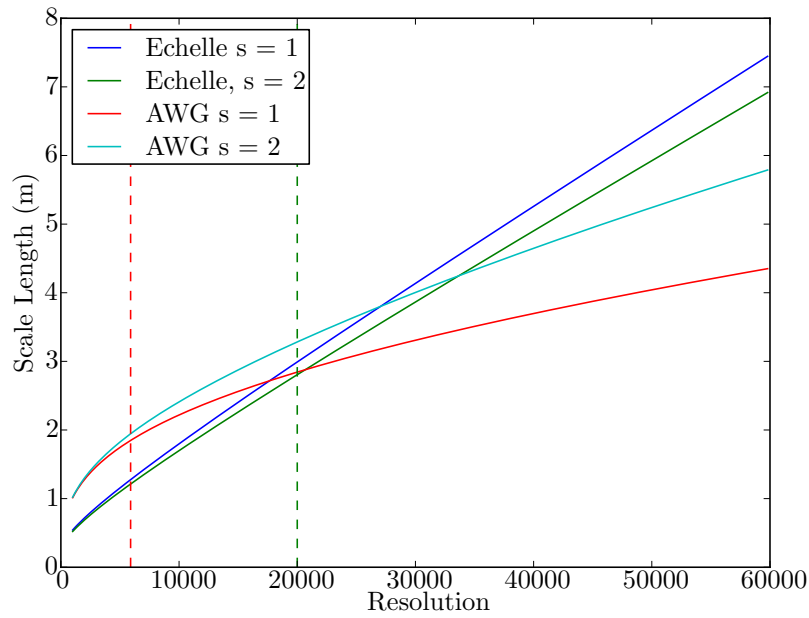
Figure 4.3: The resulting scale lengths due to varying the resolution of the GNIRS models with the different scaling parameters. The red dashed line represents GNIRS, the green dashed line represents where telecommunications AWGs operate.
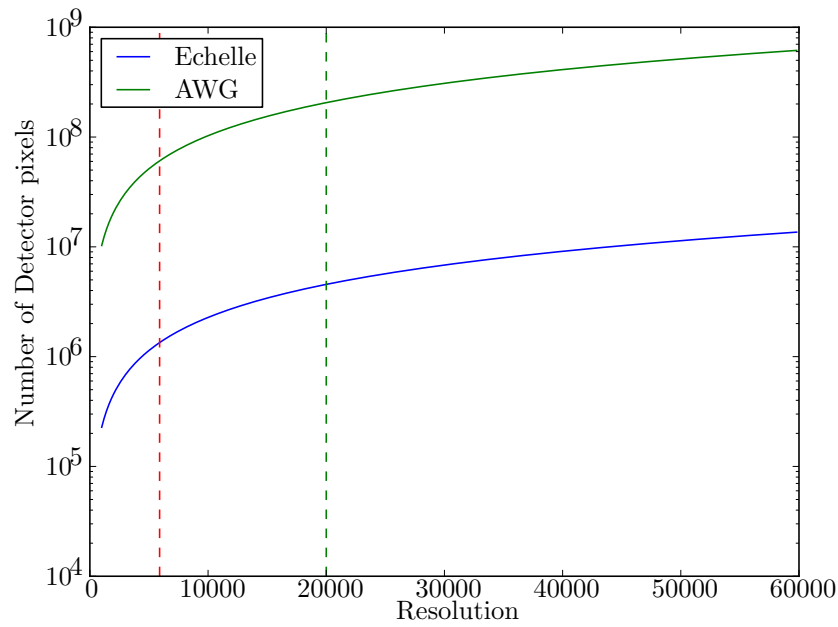
Figure 4.4: The resulting pixel numbers due to varying the resolution of the GNIRS models with the different scaling parameters. The red dashed line represents GNIRS, the green dashed line represents where telecommunications AWGs operate.
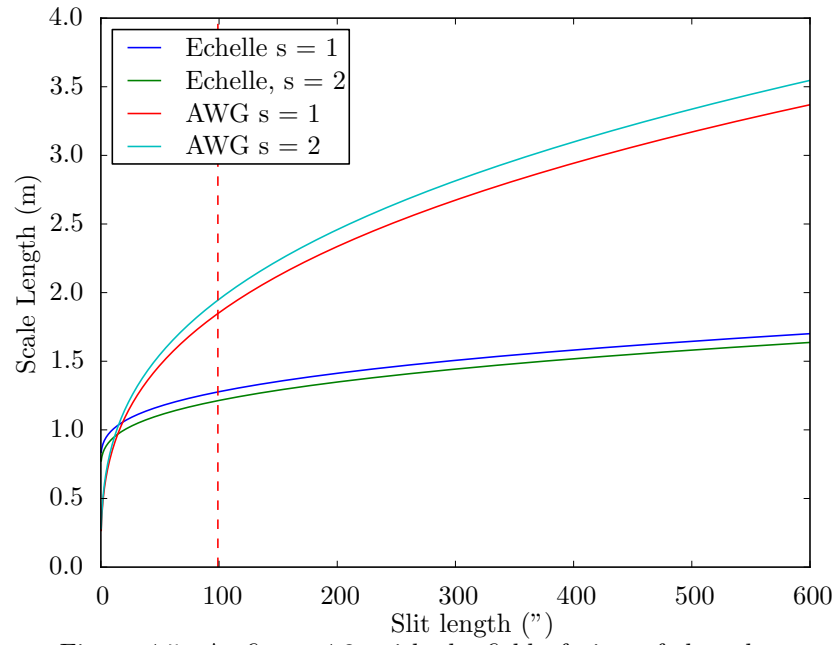
Figure 4.5: As figure 4.3, with the field of view of the telescope varying.
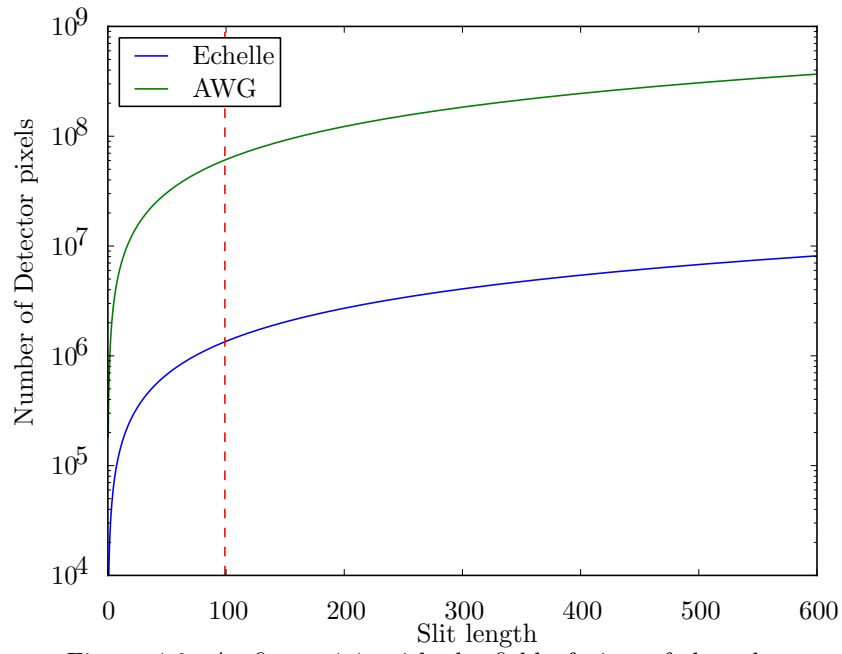
Figure 4.6: As figure 4.4, with the field of view of the telescope varying.
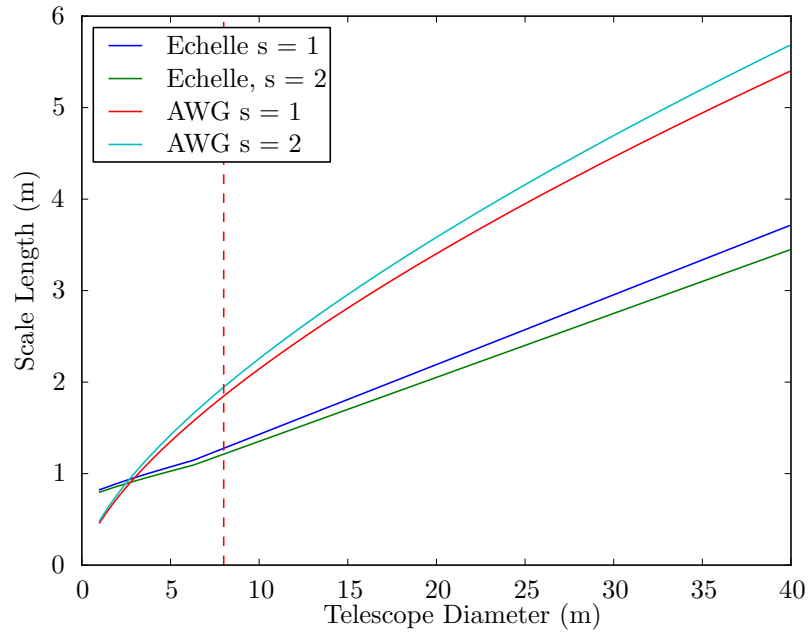
Figure 4.7: As figure 4.3, with the diameter of the telescope vary-ing.
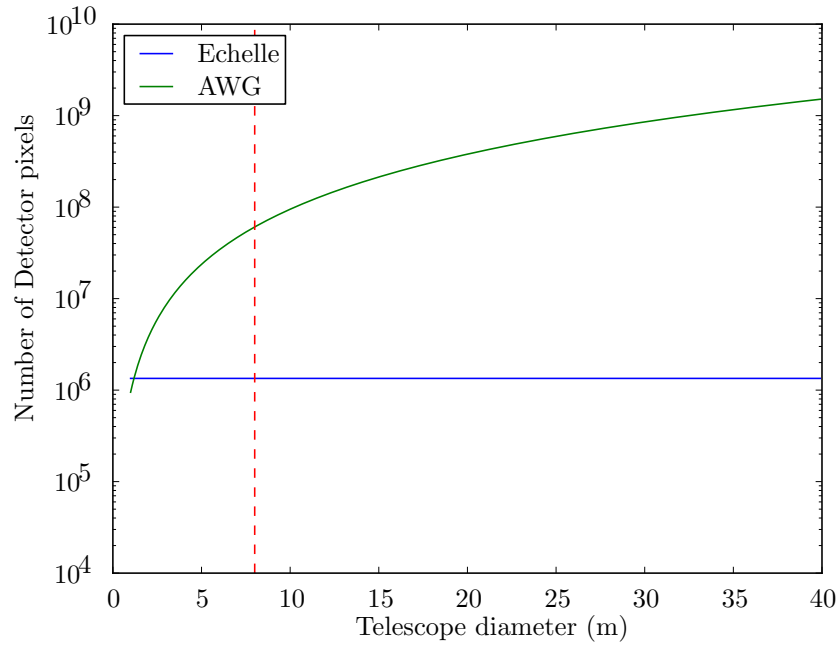
Figure 4.8: As figure 4.4, with the diameter of the telescope varying.
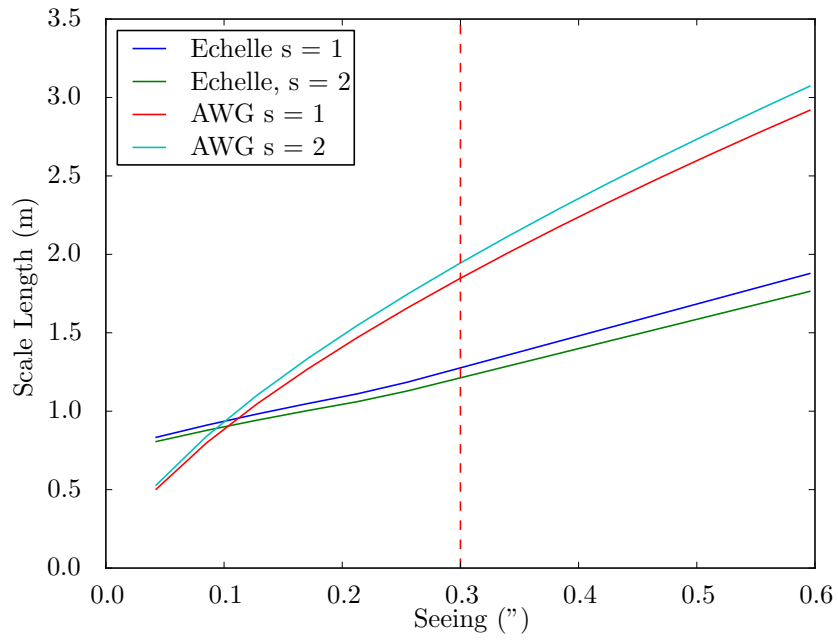
Figure 4.9: As figure 4.3, with the seeing of the telescope varying.
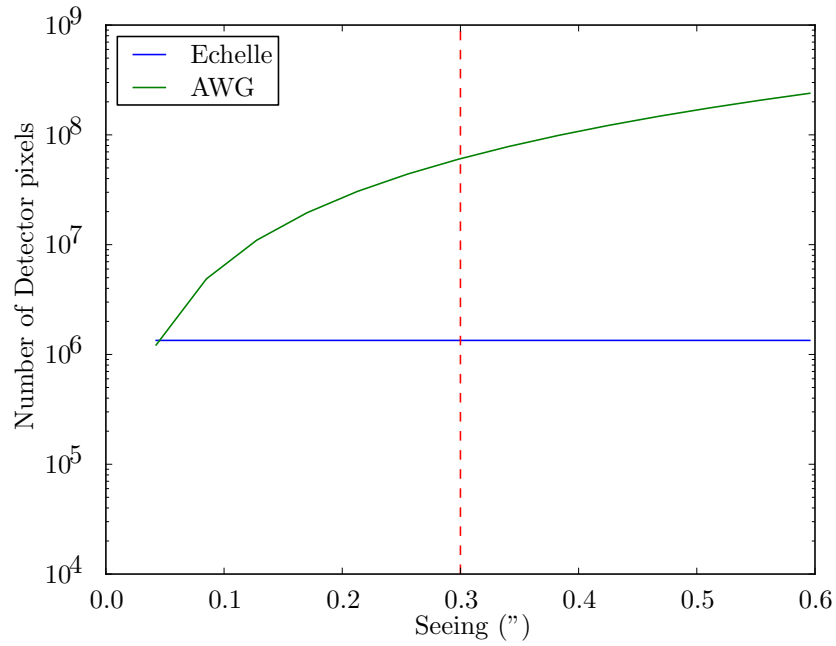
Figure 4.10: As figure 4.4, with the seeing of the telescope varying.

larger telescopes unless the input is very close to the diffraction-limit. We find that IPS instruments may be suited to instruments with smaller FOV, such as amateur instruments or for high resolution spectroscopy.

Our results indicate the number of detector pixels will be substantially higher for photonic instruments unless the input is very close to the diffraction-limit. This suggests that either near diffraction-limited AO or a space based mission would be required for optimal performance from photonic spectrographs.

4.5 Identifying scientific cases for the IPS

We have examined the AWG version of the IPS and concluded that the instruments would need to have a small FOV (to maintain a small size), and have a near diffraction-limited input (due to the number of detector pixels) to best compete with conventional instrumentation. This means the instruments would be best suited for certain types of astronomy and require either a small telescope, near diffraction-limited AO, or to be space based. Also due to the nature of the devices any science cases would most likely be in the near IR.

In order to examine the science cases we explored the literature. We found our requirement for near diffraction-limited seeing overlaps with those of the ASTRONET report [90] and the ReSTAR report [91]. These reports examined uses of 1 to 4 metre class telescopes in the future, both in Europe and the US. This class of telescope is also the most likely to trial initial IPS instruments. As such we take their report from December 2007 and identify which of its recommendations also had a small FOV or cases where few objects were examined at once in order to identify where the IPS could be of most use. We split the science cases into two regimes, low to medium ($R <$10,000) and high ($R >$10,000) spectral resolution.

4.5.1 Low-Medium Resolution

The ASTRONET report, does not identify many areas that are immediately suited for the IPS (the focus is on IFU or wide wavelength range instruments. However the ReSTAR report identifies three main areas of interest that require low spectral resolution and have a small FOV. In this regime the stability of the instrument is less important, with the focus being on the ease of manufacture, reducing the cost of the instrument and the ability for the instrument to be mass produced. The areas are listed below.

Studies of small objects in the solar system

Numerous small bodies are present in the solar system, with most inhabiting the asteroid belt and Kupier belt. Studies of these small objects within the solar system rely on detection and follow up capabilities, which small telescopes are ideally suited for provided the objects are bright enough. Not only can these objects tell us about the chemical makeup of the solar system, they can also give us information as to how it formed.

There are two main competing sets of theories about evolution of objects in the solar system. The first, older set of theories states most objects formed in place from the remnants of the material that created the sun, with a few moving due to planetary perturbations (The nebular hypothesis). The second set of theories state that the migration of Jupiter and Saturn caused massive upheavals in the solar system moving around all the materials. Thus, understanding the location and chemical composition of small objects within the solar system is key to understanding its formation history. The ReSTAR report [91] identified that imaging would be required to identify objects in both the asteroid and Kuiper Belt. Follow up studies using spectroscopy on 4m class telescopes would allow observations at limiting magnitudes of > 21 and would then tell us about

the composition of these objects and test the theories on solar system formation. This type of spectroscopy suits the IPS system, as it is examining single objects and the wavelength ranges that are of interest are the visible and near IR, so would require few modes per spaxel.

Low Mass Brown Dwarfs

Though Brown dwarfs had been hypothesised for a long time, it was not until 1995 when the first Brown Dwarf was confirmed [92]. Since then the numbers and diversity in candidates have grown hugely, mostly due to surveys such as 2MASS [93]. Future surveys will increase the numbers of candidates and in order to fully classify these objects follow up observations will need to be done. Spectroscopic surveys in particular are required to determine parameters such as composition, temperature and density. Due to the temperature of these objects low spectral resolution NIR spectroscopy is ideal to maximise flux contrasts. To observe the brightest objects a 4m class telescope will be needed to provide sufficient signal to noise within a reasonable time [91].

Variable stars

Observations of variable stars are useful, both to determine the processes driving their variability, but also in the case of Cephied variables can be used to determine other parameters such as distance. The [91] report also identifies the need for time resolved spectroscopy as part of a network of telescopes and instruments around the globe. This would allow the continuous monitoring of variable objects in various wavelength ranges and time periods. It would give information on variables such Cephied Variables, Wolf-Rayet stars, eclipsing binaries and Gamma Ray Bursts. The IPS could be used to monitor these variable stars in the near IR.

4.5.2   High Resolution spectroscopy

Both the ASTRONET and ReSTAR report identify several areas where the IPS could be useful in high spectral resolution spectroscopy. This is once again looking at small numbers of objects. The IPS has potential to be very useful due to its diffraction-limited slit providing a highly stable input. However to utilise this to its full potential any IPS device will need to be subject to the same constraints on temperature and other variations as current high resolution spectrographs (e.g. HARPS [94]).

4.5.3   Solar system

The ReSTAR report identified two main areas in the solar system that would benefit from study using a device with a small FOV. The first area is the study of comets and in particular their tails. As stated in section 4.5.1 these objects can tell us about the formation of the solar system. The report states there are around 30 per year that are bright enough to study spectroscopically using 4m class telescopes. The second area is the atmospheres of planets. Whilst this has been an active area of research for many years further study allows us to probe the composition and dynamics of the atmospheres to greater levels.

4.5.4   Planetary candidates

Both the ASTRONET and ReSTAR reports included identification and classification of extrasolar planets as areas of interest. The first exoplanet around a main sequence star was discovered using spectroscopy in 1995 [95] and since then the number of candidates has grown rapidly (around 1800 at the time of writing). In recent years the transit technique has reached maturity and is delivering lots of candidates due to surveys such as SuperWASP and HAT, and space missions such as COROT and Kepler. Despite this, spectroscopy surveys

on instruments such as SOPHIE and HARPS are still heavily used, not only to detect planets, but also to confirm candidates and constrain parameters on already discovered planets. The ASTRONET report identified that stable spectrographs of R = 100,000 to achieve > 1m/s precision in the optical would allow more candidates to be detected and classified. If the IPS could be proven at these wavelengths and resolutions it would be very useful.

The ASTRONET report also identified the need for stable R = 70,000 spectrographs (again > 1m/s precision) in the near IR. This would allow examination of the smaller stars with increased sensitivity to planets, in an area where the star to planet flux ratio is lower. This is ideally suited to current IPS technologies,which are mainly designed from telecommunications wavelengths. The IPS also has the potential to increase the stability of these spectroscopic surveys by slicing to the diffraction-limit. This means the modal noise associated with multimode fibres is rearranged into the spatial axis, removing a source of noise and increasing the precision of the instrument.

4.5.5   Nearby Stars

Both the ASTRONET report and ReSTAR report identified that investigations of nearby stars with high resolution spectrographs would be an important area of research. Determining the chemical high spectral resolution spectroscopy could be used to determine the chemical composition and dynamical properties of these. Examining the chemical composition could be used to help further constrain the evolutionary models of stars, particularly if studying the whole life cycle. Studies of the dynamical properties would allow better understanding of the dynamics of our galaxy.

Science Case	Number of Spaxels	Wavelength Range	Resolution	Telescope size
Solar system objects	1	Vis & NIR	Low, high	4m
Brown Dwarfs	1	NIR	Low	4m
Variable stars	1	NIR	Low	> 2m
Exoplanet	1	Vis & NIR	High	4m
Nearby Stars	1	Vis & NIR	High	> 2m

Table 4.2: Parameters for the IPS science cases. The number of spaxels is the number of spatial samples, the wavelength ranges are either Visible or Near IR, the resolution domains are defined at the start of this section and the telescope size is the minimum size in the reports that would be useful for observations.

4.6 Conclusions

We have used simplified models for both a conventional echelle model and an IPS model to simulate the size and number of detector pixels of GNIRS on Gemini. We have then varied spectral resolution, telescope diameter, sample size and FOV. Our results are presented in terms of the scale length (cube root of the volume) of the instrument and the number of detector pixels the instrument will require. Our findings suggest that photonic spectroscopy would be most useful on instruments with diffraction-limited seeing, or a small telescope. The is also potential for the IPS to be useful in high resolution spectroscopy, provided the devices can be made. We find that the IPS instrument will be on the same magnitude in terms of size as a conventional spectrograph, but will have more detector pixels if the input is not diffraction-limited.

From this we examined which science cases put forward by the ASTRONET report [90] and the ReSTAR report [91] were near diffraction-limited, had a small FOV and were in the near IR. We found that there are multiple cases for the development of the IPS at both low and high spectral resolution. If an IPS could be shown to be cheaper and more stable than a conventional spectrograph then it could complement or replace certain types of instrumentation on existing

telescopes.

Chapter 5

Alternative designs for the IPS

5.1 Introduction

In this Chapter we propose methods to improve upon the design of the IPS system by modifying current AWG technologies. We assume modular instruments containing a single spaxel and make use of both conventional and photonic techniques. Where an AWG is used we assume that the input and output waveguides (or first and final faces for a tandem concept) have been removed to optimise spectral resolution. We present a table summarising the concepts and then conclude with our preferred instrument concepts.

5.2 Methodology

We shall use the following metrics in our examination

- **The throughput of the system** T. This includes all the components

of the system excluding the telescope coupling and detector efficiency. It also ignores the wavelength-dependence of the system.

- **The spectral resolving power**, R ($\equiv \lambda/\delta\lambda$, where $\delta\lambda$ is the spectral resolution). The maximum for a diffraction-limited spectrograph is $R^* = mN$, where m is the diffraction order and N is the number of waveguides in the AWG or the number of illuminated rulings on a grating.

- **The Free Spectral Range** F of the device, for a conventional AWG with a spectral resolution of $R \approx 20{,}000$ this will be of order 40nm. With current manufacturing techniques the AWG is restricted in size to around 8". As such an AWG will be restricted in the FSR and spectral resolution it can achieve [63].

- **The number of pixels required to sample the output spectra** N_P. This influences the total cost of the instrument. It will be dependent on the number of modes produced by the PL and how the spectra are arranged on the detector. The minimum per spaxel will be $P_{\min}$, which corresponds to the Nyquist-Shannon limit.

- **Number of AWGs or spectrographs per spaxel**, N_{AWG} or N_{S}. This will be dependent on the number of modes that can be input into each AWG or spectrograph and will influence how much the final instrument costs.

- **The instrument size per spaxel**. This is the approximate size of the instrument per input spaxel. This is an estimate based on the rough size of the components.

- **The manufacturability**. This will depend on the components used. Most of the concepts described here use existing manufacturing methods, although some are more commonly used than others.

We shall use the following symbols and values for our components.

- T_{PL} : In lab conditions the fibre PL has been shown to have throughput up to $\approx 90\%$, though so far this has not been replicated on sky.

- T_{AWG} : The throughput of the individual AWG, which we take as 75%, consistent with tests in laboratory conditions. [5]

- T_{REF} : This is the throughput of the reformatter used to rearrange the single modes. This can be achieved using technology such as ULI [96] to form a slit. We assume a throughput of 75% which is consistent with in laboratory tests for ULI reformatters.[13].

- T_{OPT} : The throughput of additional optics for re-imaging. This is dependent on the type of optics used and the number of components. We assume a throughput of 90%.

- T_{X} : The throughput of cross dispersion optics. This will vary depending on the type of cross dispersion used, but we assume 75%.

- T_{S} : The throughput of a conventional spectrograph. We assume 75%, the same as an AWG.

- M : The number of spatial modes (not including polarisation) per spatial sampling element, or spaxel. If the input is diffraction-limited, M will equal one. If the input is from a larger seeing-limited telescope, M will scale with the diameter of the telescope squared [17].

- P_{min}: The minimum number of pixels required to sample a spaxel using a set FSR at a set spectral resolution in a conventional spectrograph. This corresponds to the number of spectral resolution elements multiplied by the Nyquist-Shannon sampling limit (2 samples per element).

- *Q:* The number of single mode inputs per AWG. For most of the concepts this is an estimate and would require further research to determine more accurately.

5.3   Design options using AWGs

5.3.1   Single input design

The single input concept for an IPS was first explored by reference [3]. Since this was designed as a demonstrator, it is not fully optimised; however it provides a good reference for comparison.

In the device a PL samples the PSF from the telescope. This splits the light into multiple single mode fibres, each of which feeds an AWG. The light from each AWG is sampled by a detector (which can be coupled to the end of the AWG, e.g. [97]). This concept is shown in figure 5.1.

The overall throughput will be $T_{\mathrm{PL}}T_{\mathrm{AWG}}$, which using our estimated values yields $\approx 68\%$. The spectral resolving power will be R^*/C, where C is a factor accounting for errors, meaning the AWG does not achieve diffraction-limited performance [63]. Whilst there are no current explanations in the literature about why this is the case, several reasons may include errors in waveguide lengths and widths, differences in refractive index within the chip and errors when coupling to the devices. The lowest current value of C is 1.6[63]. The FSR is set to F_{AWG} which is around 40nm for a standard instrument.

Since light from each spaxel will be split into separate spectra the number of pixels required to sample the spectra will be MP_{min} resulting in the over-sampling of the spectra by a factor of M. The number of AWGs per spaxel will also be M, similar to a conventional spectrograph design, or larger if the input is far from the diffraction limit (see [17]). There are no known issues with the

manufacture of these devices, as all the components currently exist.
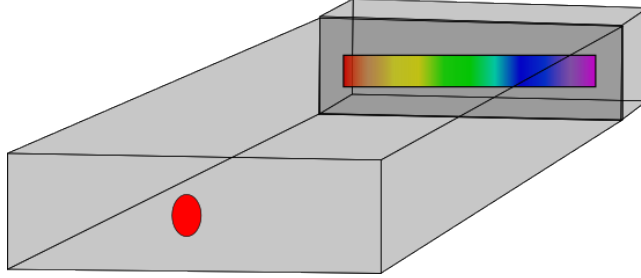
Figure 5.1: The single input design. A PL (not shown) reformats light from the telescope into single modes. Each single mode fibre feeds a conventional AWG which then disperses the light onto a detector. This detector can be linear if placed at the end of the AWG, or part of a 2D array if the output is re-imaged (not shown).

Although it shows the basic functionality required for an astronomical instrument, this design is not optimised for astronomical applications due to its limited FSR and the single input per AWG.

5.3.2 Tandem AWG design

This is a design proposed in the telecoms industry [79, 98] to increase the FSR of AWG devices. In astronomical applications a PL will be required to sample the telescope PSF. These will be fed to a single broadband AWG (or other dispersive component), which separates a large FSR into chunks. These are then sent to a second line of AWGs which disperse the light at a high spectral resolution onto a detector. This concept is shown in figure 5.2.

The throughput of the system will be lower than that of the single AWG design due to the extra AWGs. In theory this should be $T_{\mathrm{PL}}T_{\mathrm{AWG}}^2$, which with our estimates yields $\approx 51\%$, although reported throughputs are less than 10%[79]. Note that although this looks an attractive prospect the current instruments show very low throughput. The spectral resolving power is only dependent on

the second row of AWGs, so remains at R^*/C. The FSR is greatly improved from the single AWG design, resulting in approximately $N_{\mathrm{C}}F_{\mathrm{AWG}}$, where N_{C} is the number of cascaded AWGs.

The number of pixels will be $MP_{\min}N_{\mathrm{C}}$ due to each mode requiring a set of cascaded AWGs. The number of AWGs per spaxel will be $M(N_{\mathrm{C}}+1)$ for the same reason. Whilst the design removes the limits on FSR imposed by individual chip size we now have an increased number of AWGs. This means the total size is of the same order as a conventional or photonic instrument, with the same spectral resolution and FSR. As with the single input concept all of the technology has been tested, although it is not currently in common production within the telecommunications industry.
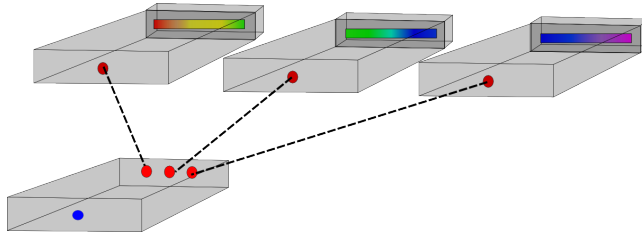
Figure 5.2: The tandem AWG design. A PL (not shown) reformats light from the telescope into single modes. These single mode inputs are then split by wavelength within an initial AWG. This produces multiple single mode fibre outputs containing different wavelength ranges. These are fed into separate AWGs which disperse the spectra onto detectors.

The use of the tandem design allows for larger FSR than the single input AWG, potentially making it more suitable for astronomy. Due to the tandem nature the throughput of the device will be reduced. There are also still spectral oversampling problems if the device is not fed by a diffraction-limited input.

5.3.3   Multiple inputs per AWG, with a cross dispersed output

In this design, multiple modes are arranged at the input of a conventional AWG. For astronomical applications the system will require a PL to sample the telescope PSF. These are then dispersed in the AWG and the resulting spectra cross dispersed using a separate dispersive element at the output end of the AWG. This was first explored by [5] and is shown in figure 5.3.

The throughput of the central input is $T_{\mathrm{PL}}T_{\mathrm{AWG}}T_{\mathrm{X}}$, which with our estimates yields $\approx 51\%$. However experiments have shown this is reduced for inputs which are not located at the centre of the AWG [5], as such the total throughput will be $< 51\%$. The spectral resolving power shows a similar pattern with $R = R^*/C$ for the central input and reduced for others. Current designs have set the FSR to be F_{AWG}, though with modification the cross dispersion could potentially be used to access other spectral orders allowing a greater FSR.

The number of pixels per spaxel will be greater than MP_{min}, most likely due to gaps in the spectra on the detector. The number of AWGs per spaxel will be dependent on the number of inputs per AWG, M/Q. The size was recently shown to be larger than conventional spectrograph or IPS due to the addition of extra components [17]. All of the technology is currently developed and the concept has been demonstrated [5].

It should also be noted that the device could be used without cross dispersion, this would require two different conditions. First the FSR could be reduce and the inputs separated such that there was no overlap between the resulting spectra. This would likely lead to losses in both throughput and resolution as the inputs were moved off axis (such as those in [5]). The second involves using energy resolving detectors such as those mentioned in section 2.2.1, this would greatly reduce the size of instruments. However current devices have low

resolutions (R ≈ 10), which are too low for current AWG devices.
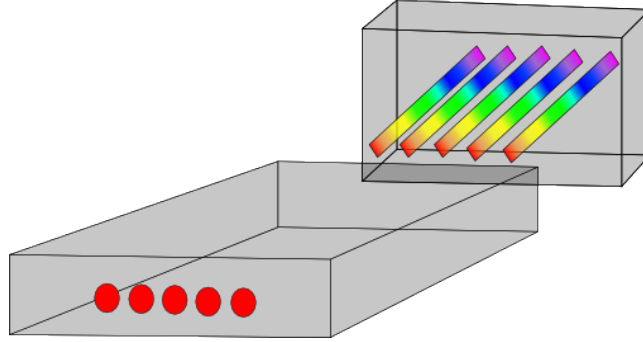
Figure 5.3: The cross dispersed AWG design. A PL (not shown) reformats light from the telescope into single modes. Multiple single modes are input to a single AWG. The resulting spectra are then cross dispersed at the output end using additional optics (not shown for clarity) onto a 2D detector.

This design reduced the number of AWGs, but requires additional optics to be added to the design, meaning the device is no longer fully integrated. Additionally the spectral oversampling remains large for inputs that are not diffraction-limited.

5.3.4 AWG with slit input

This concept uses multiple modes in single AWG (in a similar manner to the cross dispersed option), but with the inputs closer together in the form of a slit. This is then dispersed within the AWG, with a degraded spectral resolution due to the increased width of the slit. For astronomical applications this will require a PL to sample the PSF from the telescope and a reformatter to make the slit. This will then need to be integrated with the AWG and the output fed to a detector. The concept is shown in figure 5.4.

The throughput will be $T_{\mathrm{PL}}T_{\mathrm{REF}}T_{\mathrm{AWG}}$, which with our estimates yields ≈ 51%. The spectral resolving power will be degraded due to the increased slit

width and there is also potential for it to be degraded due to modal interactions. Whilst the precise factor needs to be examined through simulations of the modes within the slit, the spectral resolving power should be approximately R^*/CQ. The reduction in spectral resolving power would be similar in a conventional spectrograph with a similar input, though this would not be done in conventional spectroscopy. As with the single AWG the FSR is set to F_{AWG}.

The number of pixels per spaxel can be reduced to P_{min} and as with the single input option the AWG can use a linear detector instead of a two-dimensional device. The number of AWGs per spaxel will be M/Q. Although this concept initially reduces the instrument size per spaxel, to maintain the same spectral resolution as other concepts the AWG need to increase in size, resulting in a similarly sized instrument.
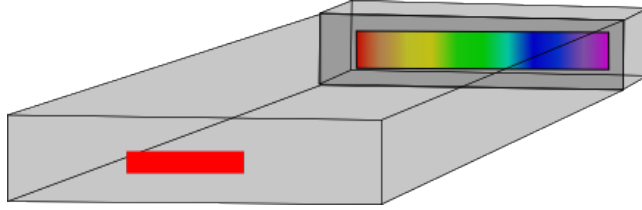
Figure 5.4: The AWG with slit input design. A PL (not shown) reformats light from the telescope into single modes, which are then reformatted into a long slit. This would then be attached to the AWG parallel to the axis of dispersion. This would then be dispersed, with the length of the slit reducing the spectral resolution compared to a conventional design.

This design trades spectral resolution and stability for simplicity. All of the components are integrated which has the potential to make a robust low resolution spectrometer.

5.3.5 Thickened AWG with slit input

This involves increasing the thickness of the AWG. This allows an input that is multimode in the spatial direction, but single-moded in the spectral direction. To manufacture the concept would require laying a thicker layer of the core material, then etching the structure for longer than for a standard AWG. For astronomical applications a PL would be required to accept the light from the telescope, this would then have to be reformatted before being fed to the modified AWG. This would then disperse the output onto a detector. The concept is shown in figure 5.5.

The throughput will be $T_{\mathrm{PL}}T_{\mathrm{REF}}T_{\mathrm{AWG}}$, which with our estimates yields $\approx$ 51%. The spectral resolution will be degraded by the extra modes. These additional modes would have differing effective indices, reducing the spectral resolution of the device. The limit will tend to $n_{max}/(n_{max} - n_{min})$ as the diffraction order tends to infinity, here n_{max} and n_{min} are the maximum and minimum effective indexes of the input modes, the calculation for this is shown in appendix 8.1. As with the single AWG the FSR is set to F_{AWG}.

Provided that light from all the modes can be directed into the pixels of a linear detector array (which may be rectangular), the number of pixels can be as low as MP_{min}/Q. The number of AWGs per spaxel will be M/Q. As with the slit input concept, the spectral resolution is decreased. To maintain the same spectral resolution as other concepts the size will have to be increased, resulting in a similar sized instrument. There are also potential difficulties with the manufacture of these devices due to the depth of the core layer.

This concept retains an integrated design, though creates a degradation in resolution due to differing effective modal indices. It has the potential to reduce the spectral oversampling, although there is considerable uncertainty over whether the concept can be manufactured. This design is best used for low
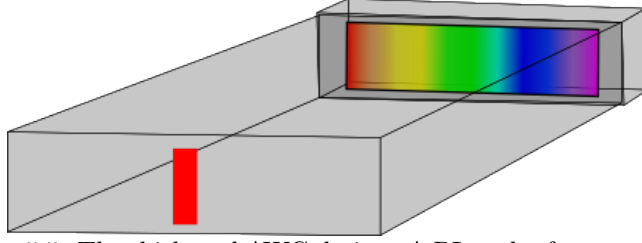
Figure 5.5: The thickened AWG design. A PL and reformatter (not shown) couples light from the telescope into single modes, which are then reformatted into a long slit. This slit is then joined to a modified AWG perpendicular to the spectral direction. The light is then dispersed and sampled by a coupled detector.

spectral order (and hence low resolution) operation due to its asymptotic limit on spectral resolution.

5.3.6   Angled AWG stack

This involves polishing multiple AWGs at an angle. These are then stacked, focussing all of the outputs on a detector. For astronomical applications it will require a PL to sample the telescope PSF. This will feed all of the AWGs which will disperse light onto a detector. The concept is shown in figure 5.6.

The throughput would be $T_{\mathrm{PL}}T_{\mathrm{AWG}}$, which with our estimates yields $\approx$ 68%. However detector efficiency reduces with angle, which will reduce this value. This reduction is low at small angles and rapidly increases as the angle increases [99]. The spectral resolving power will be up to R^*/C, although this requires all the output spectra to be focussed at the same point. This will be dependent on manufacturing tolerances and may be difficult to achieve. As with the single AWG the FSR is set to F_{AWG}.

The number of pixels per spaxel will be at least P_{min}, depending on the dimensions of the pixels used. The number of AWGs per spaxel will be M. The size will be smaller than single input devices due to the removal of the

cladding, though still of the same order as conventional instruments. There may be interference between modes as the outputs are brought together resulting in the formation of speckles with a consequent degradation of spectral resolution. There are also concerns as to whether the AWGs can be polished to the required thickness without breaking as this concept will require the output end to be tens of microns thick.
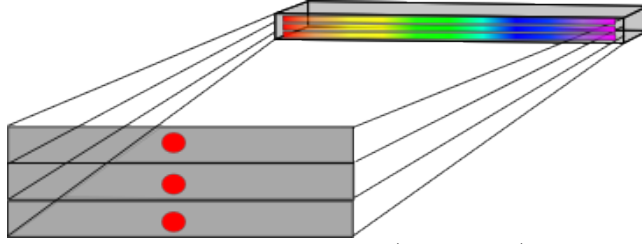
Figure 5.6: The angled design. A PL (not shown) reformats light from the telescope into single modes, which are then reformatted into a long slit composed of single modes. These are fed to a stack of modified AWGs. These disperse the light and focus the resulting spectra on a point or small area on the detector.

Theoretically this has a lot of advantages, as it allows the device to be made smaller by the reduction of the cladding in the AWG and reduces the amount of pixels needed. In practise there may be degradation of resolution due to modal interference and manufacturing errors. This makes it a less attractive design option.

5.3.7 Multiple stacked AWGs focussed onto Detector (stacked)

This involves focussing the outputs of multiple AWGs onto a detector using a cylindrical lens as proposed in [72]. For astronomical applications it would require a PL to sample the PSF from the telescope. This would feed multiple stacked AWGs with their outputs focussed onto a detector using a cylindrical lens. The concept is shown in figure 5.7.

The throughput will be $T_{\mathrm{PL}}T_{\mathrm{AWG}}T_{\mathrm{OPT}}$ which, with our estimates yields $\approx$ 61%. The spectral resolving power will be up to R^*/C, provided the resulting spectra from the AWGs can be overlapped on the detector without modal interactions. As with the single AWG the FSR is set to F_{AWG}.

The number of detector pixels will be at least $P_{\min}$ depending on the dimensions of the pixels used. The number of AWGs per spaxel will be M. The size will be larger than the single-input AWG option due to the extra components in the system.
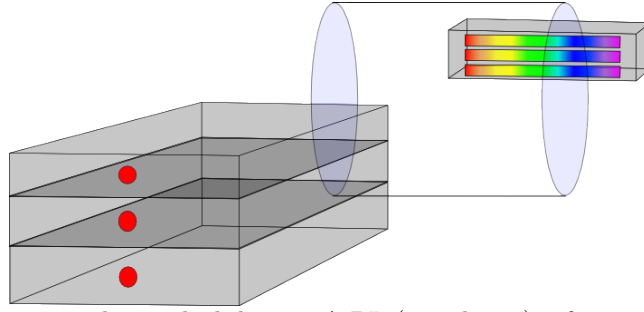
Figure 5.7: The stacked design. A PL (not shown) reformats light from the telescope into single modes. The single mode fibres feed a stack of AWGs which disperse the light. The outputs are then focussed using a lens onto a detector.

This option may suffer from problems with modal interactions as multiple spectra are focussed onto the detector. It is not a fully-integrated photonic system due the addition of the cylindrical lens. It has the potential to reduce the oversampling problem using conventional, off the shelf components.

5.3.8 Multiple inputs in a modified AWG

This requires multiple inputs per chip in a similar way to the thickened design, but would leave enough space for the modes to have the same effective index. This would be achieved by depositing a layer of core material, then etching the

structure and repeating the process to build up multiple layers. For astronomical applications this would require a PL to sample the PSF from the telescope, multiple modes would then be input into a single AWG. The output of this would then illuminate a detector. The concept is shown in figure 5.8.

The throughput should be $T_{\mathrm{PL}}T_{\mathrm{AWG}}$ which, with our estimates yields $\approx$ 68%. The resolving power will be R^*/C. As with the single AWG the FSR is set to F_{AWG}.

The number of detector pixels for this concept will depend on the size of the pixels and the distance between modes. If rectangular pixels were used this could reduce the total number of pixels, although this requires investigation. As such the number of detector pixels will be at least MP_{min}/Q. The number of AWGs per spaxel will be M/Q. The size will be smaller than the stacking concept due to thinner cladding layers than between individual AWGs. Investigations would have to be undertaken to see if modified AWGs can be etched deep enough. If rectangular pixels are to be used then the individual layers within each AWG would need to be manufactured to very tight tolerances to maintain spectral resolution.

Figure 5.8: The multiple inputs per AWG design. A PL (not shown) reformats light from the telescope into single modes. These are then reformatted to a long slit which is then input into a modified AWG. This disperses the light which is coupled to a detector.

This concept has the potential to reduce the size, and redundant oversampling. However, it requires the redesign of AWGs which may not be possible. It also requires all the stacked AWGs to be manufactured to tight tolerances, otherwise there is potential to degrade the resolution of the device.

5.4 Non-AWG concepts

We now turn our attention to concepts that use conventional optics to disperse the output from a PL or lantern/reformatter combination. This is in essence a new form of image slicing, which is most applicable when the input is near diffraction-limited. This retains the advantage of using single mode components whilst also using existing technologies developed for astronomy.

5.4.1 Individual single modes

Here light from the telescope is fed to a conventional spectrograph using single mode fibres in the form of a slit (PIMMS#1 as proposed by [72]). For astronomical applications a PL is required to sample the PSF from the telescope, which are rearranged into a slit. This is then fed into a conventional spectrograph. The concept is shown in figure 5.9.

The throughput will be $T_{\mathrm{PL}}T_{\mathrm{S}}$ which with our estimates yields $\approx 68\%$. The spectral resolution will be R^*. The FSR will be set by the spectrograph design.

The number of detector pixels will depend on how small the slit can be made, but will be greater than $MP_{\min}/Q$. The number of spectrographs per spaxel will be one, provided the optics can accommodate the length of the slit. The size will be the same as a conventional spectrograph, as we are image slicing to the diffraction-limit (e.g. chapters 3 and 4 and [76, 17, 88]).

This concept takes advantage of the flexibility of photonic technologies with the benefits of the conventional spectrograph. Depending on manufacturing techniques this may be an attractive option, although if the modes can be brought together then the number of pixels could be reduced. This is explored in the next concept.

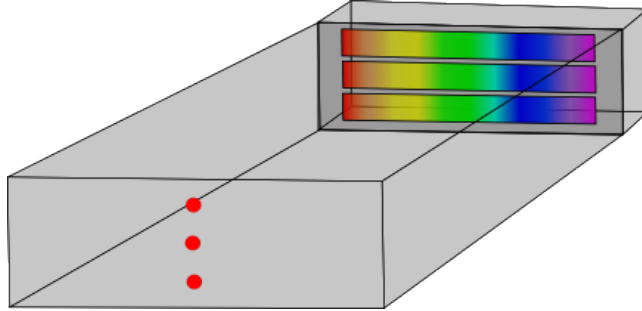Figure 5.9: The individual single mode feeding a spectrograph design. A PL (not shown) reformats light from the telescope into single modes. These are then reformatted into a long slit composed of single modes, which are then dispersed in a conventional spectrograph.

5.4.2   Long Slit

Here light from the telescope is reformatted into a long slit but with no spaces between modes. This has been recently demonstrated by [19]. For astronomical applications it uses a PL to reformat the PSF from the telescope and a reformatter (either fibre or ULI) to arrange them into a slit. The concept is shown in figure 5.10.

The throughput will be $T_{\mathrm{PL}}T_{\mathrm{REF}}T_{\mathrm{S}}$ which with our estimates yields $\approx 51\%$. The spectral resolution will be R^{*}. The FSR will be set by the spectrograph design. The number of detector pixels will be MP_{min}/Q. The number of spectrographs per spaxel will be one, provided the optics can accommodate the length of the slit. The size will be the same as a conventional spectrograph, as we are image slicing to the diffraction-limit (e.g. chapters 3 and 4 and [76, 17, 88]).

The concept is similar to the above slit composed of separate single modes, but could take up less space on the detector. Care needs to be taken when
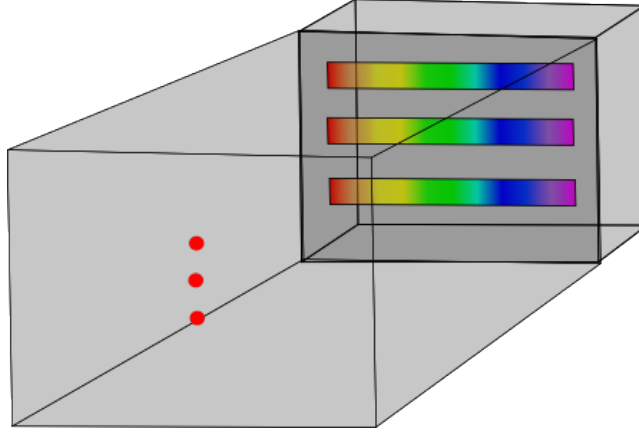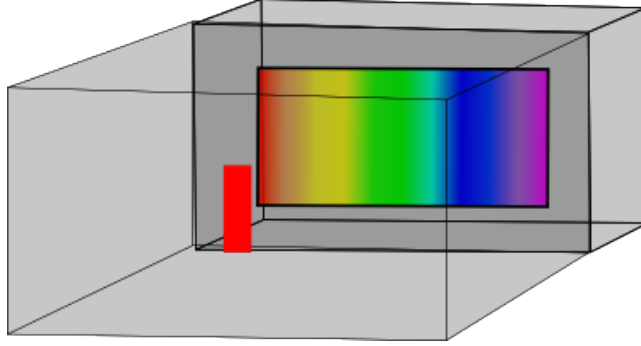
Figure 5.10: The long slit conventional spectrograph design. A PL (not shown) reformats light from the telescope into single modes. These are then reformatted into a long slit which is then dispersed in a conventional spectrograph.

bringing the slit together that light is not lost due to modal interactions.

5.4.3 Tiger Concept

This uses the multicore output from a PL to feed a conventional spectrograph (as proposed by [73]). For astronomical applications it uses a PL to reformat the PSF from the telescope, this is not reformatted but separated out into single modes. These single modes are then dispersed by conventional optics. These are rotated to make sure the resulting spectra do not overlap. The concept is shown in figure 5.11.

The throughput will be $T_{\mathrm{PL}}T_{\mathrm{S}}$ which with our estimates yields $\approx 68\%$. The resolution will be R^*. The FSR will be set by the spectrograph design. The number of detector pixels will be MP_{min}. The number of spectrographs per spaxel will be one, provided the optics can accommodate the length of the slit. The size will be the same as a conventional spectrograph.

This concept has potential for use in astronomy, though suffers from spectral oversampling when the input to the device is far from the diffraction limit.
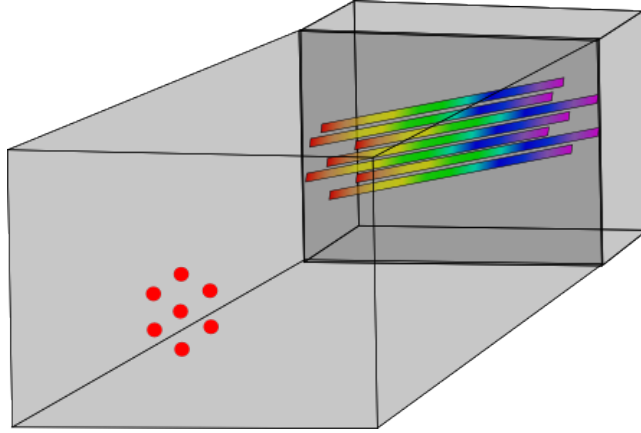
Figure 5.11: The Tiger concept. A PL (not shown) reformats light from the telescope into single modes. These are then fed to a conventional spectrograph and dispersed so that the spectra do not overlap.

5.5   Concepts summary

We summarise the values of our metrics in tables 5.1 and 5.2. All of the above concepts had similar results in estimated throughput, with the single input, angled, multiple input per AWG, individual modes and Tiger concepts showing the highest values of 68%. This is our least accurate metric as components in the field are rapidly improving and the results they achieve are very dependent on wavelength and atmospheric conditions. The spectral resolution is high for all concepts, with the exception of the cross dispersed, slit input and thickened concept, which were reduced either due to off axis inputs or a slit input. The cross dispersed, slit, thickened and multiple AWG concepts reduced the numbers of AWGs, potentially reducing the cost. The cross dispersed, tandem and conventional spectrograph concepts allow a greater FSR, which would be useful in certain areas of astronomy. All the concepts are similar in size if required to have the same science requirements (e.g. spectral resolution, mode count). As such we believe manufacturability is the most important factor in concept

design.

5.6   Conclusions

In this Chapter we have examined various design concepts for the IPS. We have looked at their relative strengths and weaknesses in terms of throughput, spectral resolution, FSR, number of detector pixels required, the number of AWGs or spectrographs required, the instrument size per spaxel and any additional difficulties with manufacture. All of the concepts described here tradeoff with the above metrics. As such the science case will determine which is most useful within astronomy.

Due to the simplicity of manufacture and number of pixels, we have two preferred concepts. Our first preference is for the AWG with slit input as it uses existing technologies and could potentially provide low resolution integrated spectrographs, though with a limited FSR. The second is the long slit with a conventional spectrograph behind. It reduces pixel numbers and is very similar to existing concepts. Both of these concepts require the demonstration of an efficient lantern/slit reformatter.

Finally, we note that there are areas including spatial filtering [100] and spectral stability which we have not explored here where photonic components could provide additional advantages, these would also need to be made to match the science cases. There are also technologies that could provide new improvements, such as energy resolving sensors that could be used instead of cross dispersion (e.g. [101]). These would also need to be considered in future science cases and instrument designs.

Design	T	Q_{max}	N_{AWG}	N_P	R	FSR
Single Input	68%	1	M	MP_{min}	R^*/C	F_{AWG}
Tandem	51%	1	$M(N_C+1)$	$MP_{min}N_C$	R^*/C	$\approx N_C FSR_{AWG}$
Cross dispersed	$< 51\%$	10	M/Q	$\geq MP_{min}$	$\leq R^*/C$	$\geq F_{AWG}$
Slit input	51 %	10	M/Q	P_{min}	R^*/CQ	F_{AWG}
Thickened	51 %	10	M/Q	$\geq MP_{min}/Q$	$\leq n_{min}\,/\,(n_{max}\text{-}n_{min})$	F_{AWG}
Angled	≤ 68 %	10	M	$\geq P_{min}$	$\leq R^*/C$	F_{AWG}
Stacked	61%	10	M	$\geq P_{min}$	$\leq R^*/C$	F_{AWG}
Multiple	68%	10	M/Q	MP_{min}/Q	R^*/C	F_{AWG}

Table 5.1: A summary of all the proposed concepts using an AWG. T is the estimated overall throughput of the system, Q_{max} is the estimated maximum inputs per spectrograph, N_{AWG} is the number of AWGs per spaxel, N_P is the number of pixels per spaxel, R is the resolution of the device and FSR the Free Spectral Range of the device

	T	$Q_{\max}$	N_S	N_P	R	FSR
Individual modes	68%	M	1	$MP_{\min}$	R^*	FSR_{S}
Long Slit	51%	M	1	$P_{\min}$	R^*	FSR_{S}
Tiger	68%	M	1	$MP_{\min}$	R^*	FSR_{S}

Table 5.2: A summary of all the proposed concepts using a photonic input and a conventional spectrograph. T is the overall throughput of the system, $Q_{\max}$ is the estimated maximum inputs per spectrograph, which is estimated from the size of current AWGs or devices, N_{S} is the number of spectrographs, N_{P} is the number of pixels per spaxel, R is the resolution of the device and FSR the Free Spectral Range.

Chapter 6

The photonic-dicer

6.1 Introduction

In this chapter we present the fabrication and testing of the photonic-dicer chip, which reformats the PSF from a telescope into a single mode slit input for a spectrograph. This was tested in conjunction with the CANARY AO system [102] on the WHT in La Palma.

Many modern instruments reformat the PSF from a telescope (e.g. using the image slicing techniques mentioned in chapter 2), however, in general, the output of the reformatter is not diffraction-limited. This means that there may be variations in the input to the spectrograph, resulting in uncertainties on measurements at the output. Solving this using photonic components has been suggested within the community (e.g. [72, 103, 104, 105]). There have also been several demonstrations of similar concepts to ours, both in the lab (e.g. [105]) and on-sky (e.g. [88, 12]). This is the first demonstration where ULI has been utilised on a telescope in this manner. It is also the first demonstration of coupling photonic technologies to an AO system. Future demonstrations will

be essential to increase the throughput. This will be done by better matching the output of the AO system to the number of modes in the photonic-dicer (see previous chapters), making them viable for future instrumentation.

The photonic-dicer consists of multimode input which samples the telescope PSF (here the PSF from CANARY) and reformats it into a single mode slit (see figure 6.3). In order to efficiently couple the light from CANARY into the chip a re-imaging system was used to magnify the image. A beamsplitter was also used to allow the PSF from CANARY to be simultaneously imaged.

Ultimately this would allow the reformatting of the corrected PSF from the telescope to form a diffraction-limited slit to a high resolution astronomical spectrograph or a low resolution photonic one. This is illustrated in figure 6.1

The device was fabricated at Heriot-Watt University in the summer of 2013 and tested on the WHT with the CANARY AO system in September of that year. This chapter is based upon [19] and although all of it is my own work it is in collaboration with the authors of that paper. In particular, an equal contribution in all areas was made by David G. MacLachlan, with whom the device was co-fabricated.

6.2   Methods

Here we describe the design of the experiment, we briefly outline the fabrication of the photonic dicer, and the alignment and optimisation procedure on CANARY.

6.2.1   Photonic-dicer design parameters

The photonic-dicer was designed to approximately match the Full Width Half Maximum (FWHM) of the PSF from CANARY. In order to do this we took images supplied by the CANARY team (e.g. [106]). These images were averaged

Telescope	AO	Dicer	Spectrograph
Uncorrected PSF	PSF	Slit	Spectrum
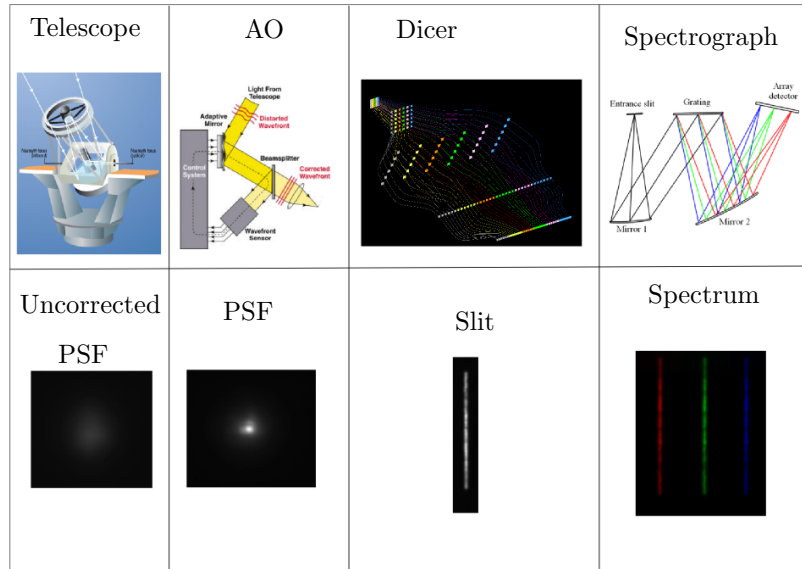
Figure 6.1: Concept for the photonic-dicer system. The top set of images shows the devices and the bottom set show the outputs. The telescope feeds an uncorrected PSF to the AO system. This feeds the corrected PSF to the photonic-dicer, which reformats it into a long slit. This diffraction-limited slit feeds a spectrograph. Top left image courtesy of the ING, second left from Lawrence Livermore National Laboratory and NSF Centre for Adaptive Optics, second right from [19] and top right from BWTEK.

and the maxima of the averaged images found. The PSF was then azimuthally averaged to allow the calculation of the FWHM. The averaged image and the azimuthally averaged profile are plotted in figure 6.2, the FWHM is shown as a red horizontal line and is approximately 450-480mas.

These results were used to estimate the number of modes that would allow the FWHM to be coupled to the photonic-dicer. To calculate this we took the diameter of the WHT, which is 4.2m, the central wavelength resulting from the passband of our filter (A KMOS H band filter) and the response of our Xenics Xeva -1.7 320 InGaAs camera, which is 1450nm, and combine it with equation 2.37. This yields approximately 25 spatial modes.

In order to cover differing values of seeing at the telescope we decided to manufacture a chip containing several devices, from a single mode up to around 50 modes. To keep the design and manufacture of the photonic-dicer simple we opted for a square input design. This is not an optimal shape for the CANARY PSF, which would have an ideal shape of a airy function (see figure 6.2). This would result in lower coupling, due to the mode shape mismatch (square mode profile vs circular mode profile). In addition coupling to the FWHM results in some of the light being lost (overfilling the aperture). We manufactured devices with 1, 4, 9, 16, 25, 36 and 49 modes arranged in a square. The separation between the modes was then increased and the individual columns shifted horizontally to allow the waveguides to be rearranged into a slit. The 6x6 design is shown in figure 6.3, with the others following a similar pattern.

6.2.2 Chip writing

The photonic-dicer was written using ULI (e.g. (see [107, 108, 109, 110, 67, 12]) at Heriot-Watt University in collaboration with David MacLachlan. This section is taken from [19] and is included for completeness. The full fabrication details
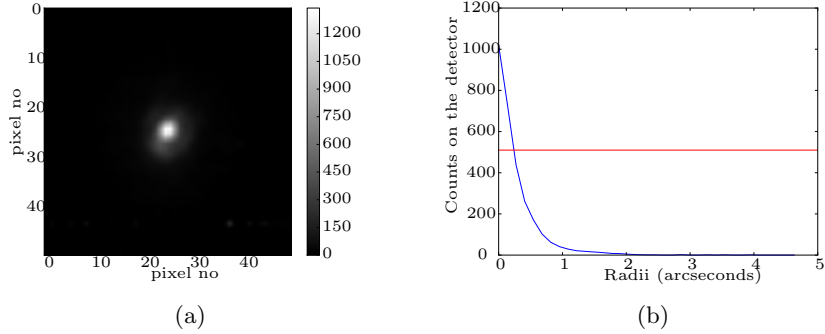
Figure 6.2: The sample CANARY data. a) The averaged CANARY PSF. b) The azimuthally averaged intensity profile of the PSF. The red line is the FWHM of the PSF, which intercepts at about 240mas.

and characterisation of the photonic-dicer will be communicated in MacLachlan et al. (in prep) and the thesis of David MacLachlan.

The substrate used to fabricate the photonic-dicer structures was a borosilicate glass (Corning, EAGLE 2000). Optical waveguides were inscribed using 460 fs pulses from a Fianium Femtopower 1060 femtosecond laser, operating at repetition rate of 500 kHz and a central wavelength of 1064nm. The waveguides were inscribed in the transverse inscription geometry using the multiscan technique [111]. Each single-mode waveguide was inscribed using 21 scans, with each scan separated by an offset of 0.4 µm. The pulse energy used was 251 nJ, with the pulses focused at a depth of ≈ 200 µm beneath the surface using a 0.3 NA aspheric lens. The inscription beam was circularly polarized. The substrate was translated through the beam focus at a speed of 8 mm s^{-1} using cross roller-bearing xyz translation stages (Aerotech ANT130). As shown in figure 6.3 (a) the multimode entrance to our photonic-dicer is constructed by bringing 36 single-mode waveguides together with a centre-to-centre separation of 8.4 µm to form a square multimode waveguide supporting ≈ 6 spatial modes in each orthogonal axis. As shown in figure 6.3 (g), the pseudo-slit output of the
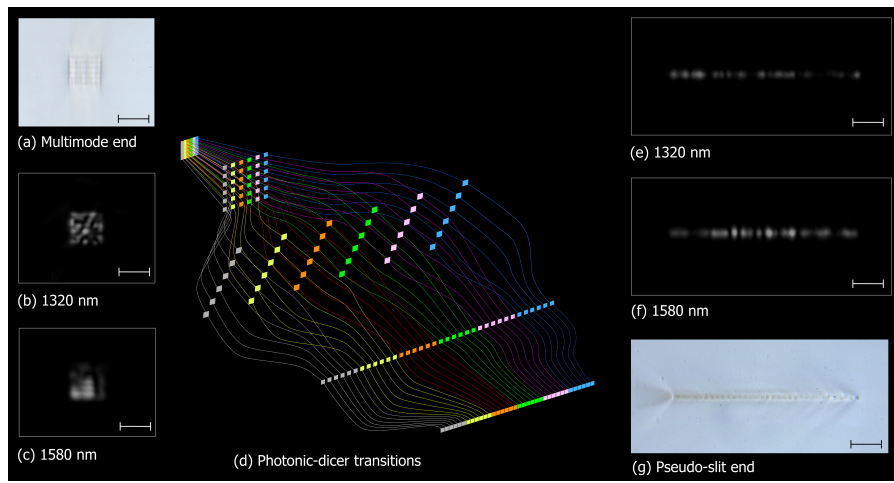
Figure 6.3: The 6x6 photonic-dicer. (a) The input facet to the input of the 6x6 dicer, here shown under a transmission microscope. Image of the facet when injected using (b) 1320 nm and (c) 1580 nm light. (d) Diagram of the dicer configuration, here the waveguides are colour coded. Monochromtically excited light at (e) 1320 nm and (f) 1580 nm. (g) Image of the reformatted slit, here shown under a transmission microscope. Scale-bar for each image represents 50 µm. Created by Debaditya Choudhury.

photonic-dicer is constructed by reformatting the 36 waveguides into a single linear array with a centre-to-centre separation of 8.4 µm.

6.2.3   Experimental Design

In order to test the photonic-dicer on-sky with a changing telescope input two simultaneous images were required. Firstly the output of the chip needed to be re-imaged onto the detector, to measure the throughput of the system and observe how it changed with time. Additionally a reference arm was needed to simultaneously image the PSF from CANARY in order to calibrate the throughput of the photonic-dicer and examine how variations in the input affected the output. A beamsplitter was used to reflect ∼10% of the light into the reference arm whilst the rest was passed to the photonic-dicer. To maximise throughput the system was also designed to be telecentric. This was achieved by arranging the lenses in a 4f configuration [112]. The experimental design is shown in figure 6.4 and described in detail below.

Due to space constraints a 200mm focal length lens (L1) was used to collimate the output from CANARY. Nintety percent of the light then passed through a beamsplitter and was re-imaged by L2. Ideally assorted L2 lenses would have re-imaged the PSF directly onto the photonic-dicer. However as described in section 6.2.1 there were different sized devices on the photonic-dicer chip (due to differing numbers of modes). This required seven different magnifications to allow the FWHM of the PSF to be re-imaged onto the chip surface and no commercially available combinations of L1 and L2 could be found to fit within the CANARY space envelope and produce the required magnifications.

As such an identical 200mm focal length lens (L2) was used to re-image the CANARY output while creating minimum aberrations. A telescope (L3 and L4) was then used to change the magnification. To reduce the risk of damaging

the photonic-dicer it was decided to make L3 variable. The appropriate magnifications for the different photonic-dicers were calculated and the lenses used for L3 are listed in table 6.2.

Due to the different focal lengths of L3 the whole experiment had to be mounted on a sliding breadboard with a micrometer used for calibration (see figure 6.5). To ensure the correct spacing between all the lenses the system was first collimated using all lenses up to L3. The position of the breadboard was measured by the micrometer and noted. The correct separation between L3 and L4 was also measured by removing L2 and collimating the beam from L4. When changing L3 the values could be looked up to ensure the correct spacing between the optics.

The output of the photonic-dicer was re-imaged by L5 and L6. These lenses were chosen so that the largest dicer slit (around 400µm) could be re-imaged onto the camera.

The reference arm consisted of the same first lens (L1). Around 10% of the light from this was then reflected from a beamsplitter and was re-imaged by L7 and L8. This combination of lenses provided a magnification of 4.3, giving the reference arm a plate scale of 19.5 arcseconds per mm.

In order to calibrate the throughput the experiment was designed so that the photonic-dicer could be removed easily. All on-sky images were taken with the chip in place and then the photonic-dicer was removed and reference images taken. The reason for this will be fully explained in section 6.4.1.

6.3 CANARY

This section appears in [19] and is included for completeness.

CANARY is an on-sky AO demonstrator system that was developed to investigate novel AO instrumentation and control techniques that will be required for
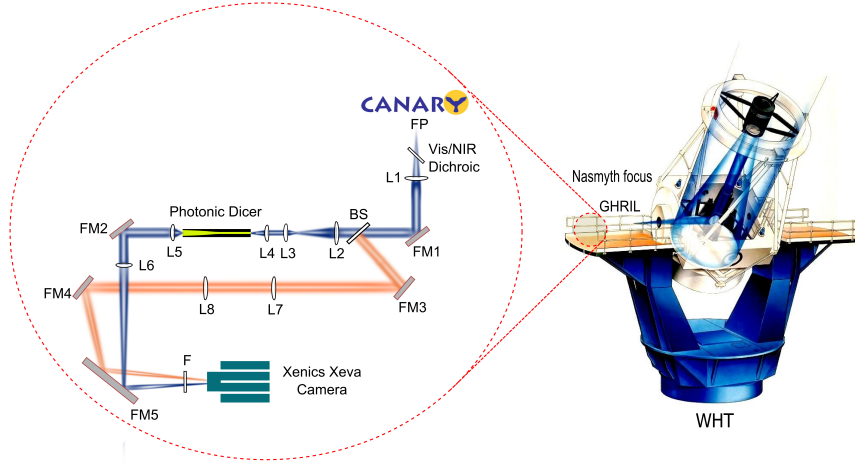
Figure 6.4: The on-sky experimental setup. The light from the William Herschel Telescope is corrected by the CANARY Adaptive-Optics system, reducing the PSF to a few modes. The light of less than 1000nm is passed to a wavefront sensor and the rest of the beam to our experiment. L1 collimates the light which is then passed to a beam splitter. 10% of the light (in blue) is fed to the reference path (here in red) and L7 and L8 re-image the PSF to the camera. The other 90% of the light is refocussed by L2 and then the magnification changed by L3 and L4. The light is injected into the input facet of the photonic-dicer. The reformatted output is then collimated by L5 and re-imaged by L6. All the fold mirrors are used for alignment. WHT image courtesy of the Isaac Newton Group of Telescopes, La Palma. Image created by Debaditya Choudhury.

Item	Thorlabs Part No	Focal length (mm)
L1	LA1509	100
L2	LA1509	100
L3	Assorted	see table 6.2
L4	C660TME-C	2.97
L5	A397TM-C	11
L6	AC254-200-C	200
L7	LA1978	750
L8	LA1464	1000
FM1-4	TBD	∞
FL5	TBD	∞

Table 6.1: Table of the lenses and mirrors used on-sky. L1 to L6 are all in the main arm of the experiment. L1, L7 and L8 are the reference arm. All components are from the Thorlabs online catalogue.

Thorlabs Part No	Focal length (mm)	Magnification at chip	Plate Scale (" mm^{-1})
C260TME-C	15.29	0.19	23.89
A375TN-C	7.5	0.4	11.35
C430TME-C	5	0.59	7.69
C350TME-C	4.5	0.66	6.88
C660TME-C	2.97	1	4.54
C392TME-C	2.75	1.08	4.20
C150TME-C	2	1.49	3.05

Table 6.2: Table of L3 lenses. The magnification at chip is compared to the output from CANARY. The plate scale is calculated using the WHT plate scale of 4.54 " mm^{-1} as the initial value. All components are from the Thorlabs online catalogue.
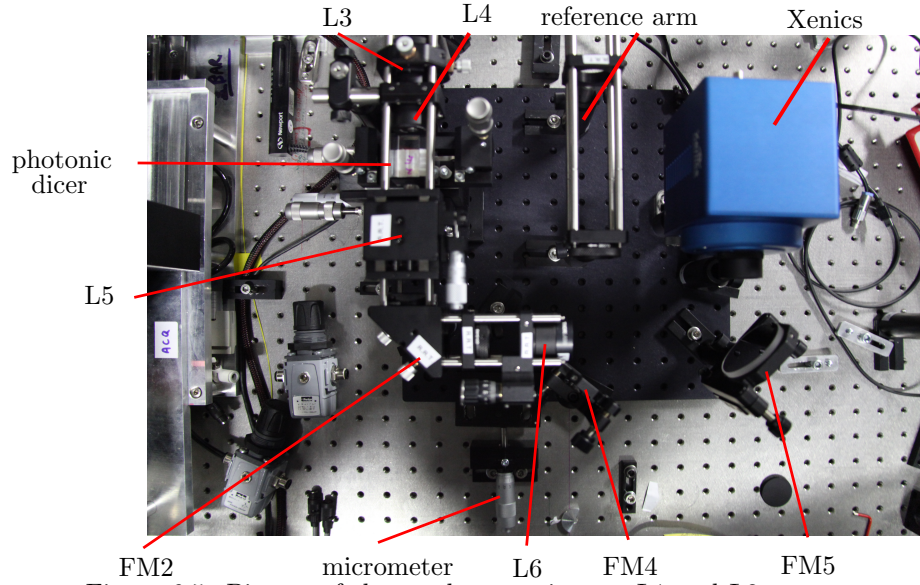
Figure 6.5: Picture of the on-sky experiment. L1 and L2 are not shown here and are off above and to the left. The main arm is visible on the left hand side. L3 collimates the beam, which is imaged onto the photonic-dicer chip by L4. The output from the chip is collimated by L5, reflected by FM3 and reimaged by L6. The reference arm is also shown (middle right) and the Xenics camera in blue. The micrometer is used to calibrate the breadboard position.

the next generation of ELT AO systems. For the work presented here, CANARY was configured to provide closed-loop AO correction using an on-axis natural guide star as the wavefront reference. Light with a wavelength >1000 nm was sent to the multimode entrance of the photonic-dicer with visible wavelengths directed to a 36 sub-aperture Shack-Hartmann Wavefront Sensor (WFS). The WFS measurements were used to drive a 56-actuator deformable mirror and a separate fast-steering mirror which could provide a partially corrected PSF at a wavelength of 1500 nm. The WFS was placed behind the deformable mirror measuring the residual wavefront error after correction. The deformable mirror commands were calculated using a basic integrator feedback controller with a closed-loop gain of 0.3.

CANARY includes a range of sources that can be used when not on-sky to calibrate and optimize system performance. For our purposes, a 1550 nm laser was coupled into a single-mode fibre and placed at the input focal plane of CANARY. Light from this calibration source passes through the CANARY optical train (including the deformable mirror and fast-steering mirror) and the output PSF is re-imaged onto the photonic-dicer multimode entrance using the setup shown in figure 6.4. The PSF at the multimode input of the photonic-dicer was then modified by changing the surface shape of the deformable mirror to maximize the detected flux from the pseudo-slit output. To modify the PSF, the AO-correction loop was engaged and static offset terms were artificially applied to the measured WFS signals. These offset terms were automatically adjusted through a process of simulated annealing [113]. The final WFS shape that provided maximum throughput was recorded and used as a reference for all subsequent on-sky operations.

CANARY was operated in three modes during data acquisition to investigate the photonic-dicer performance under different degrees of AO correction. In closed-loop mode, CANARY provided correction of both tip-tilt and higher-order wavefront aberrations at an update rate of 150 Hz. Tip-tilt mode reduced the integrator loop gain on the high-order modes to a small value (typically 0.001). In this way only tip-tilt was corrected, but the reference wavefront was maintained without providing high-order AO correction. Open-loop mode additionally reduced the gain on the tip-tilt correction to maintain the PSF in the reference location for optimum coupling without providing high-frequency AO correction.

6.3.1 Optimising for CANARY

Initial alignment of the experiment was done using 633nm HeNe lasers. One was a pencil beam used for alignment and the other re-imaged the pupil so the distances between the optics could be calibrated. Once this was done the system was optimised using the 1550nm alignment laser used by CANARY, which produced a diffraction-limited PSF at the input to the system. A five axis stage was used to align the entrance and exit facets of the photonic-dicer and the throughput was measured using a power meter (the reference arm was unused in this case). This was placed before and after the photonic-dicer and two values divided. Differing combinations of devices and L3 lenses were used to maximise the throughput of the chip.

With the photonic-dicer aligned the throughput was further optimised using a simulated annealing routine [113]. The Xenics camera was used to re-image the output from the slit whilst the routine put random patterns on the DM. The pattern with the highest throughput was recorded and set as the ideal for on-sky performance.

6.4 Results

Here we analyse our results taken on the night of the 13th September 2013. For this experiment we used the lenses in table 6.1 and the 4.5mm focal length L3 lens shown in table 6.2. All the data was taken between 21:45 and 22:30 GMT. The star selected was TYC1052-3027-1 from the Tycho 2 catalogue [114], a 3rd magnitude star in the H-band. This star was chosen as it was bright enough for short exposures, but not bright enough to saturate the CANARY wavefront sensors. The seeing during the observations was recorded by ROBODIMM [115] and was between 0.7" and 0.95" over the course of the observations (see figure
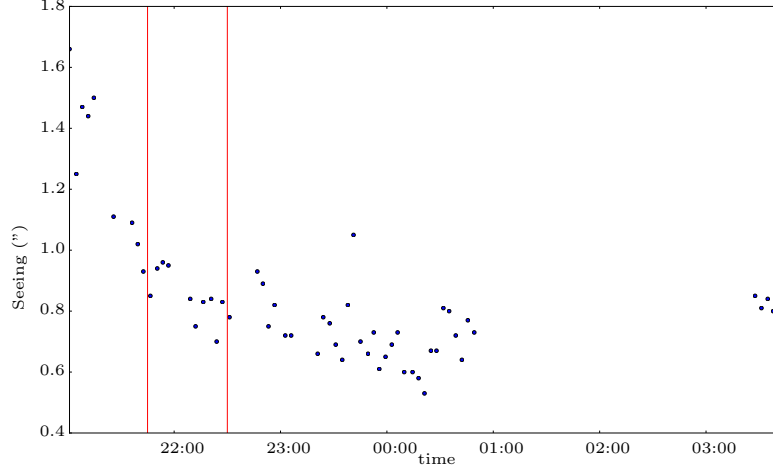
Figure 6.6: ROBODIMM values of seeing for 13-09-2013 to 14-09-2013. The scatter plot shows the recorded values of seeing recorded by the ROBODIMM seeing monitor [115]. The red lines represent the start and end of the observations for the photonic-dicer, other data points are included for completeness.

6.6 for the values). As 0.7" is the median expected seeing for the site these values represent median to poor seeing. As CANARY is designed for median seeing this resulted in a degraded PSF compared to ideal conditions, even with full correction applied. The science images were taken with three levels of correction applied : Closed-loop, which was full correction. Tip-tilt, correcting low order aberrations, and open-loop, which was no correction.

6.4.1   Data acquisition and reduction

All images were taken by the Xenics camera, with a 400µs exposure. Three types of images were taken :

1. **Science images.** These were taken in all three AO modes (Closed-loop, tip-tilt and open loop).

2. **Dark exposures.** These were taken to allow background subtraction.

3. **Reference images.** These were taken for flux calibration. This was done
   by removing the photonic-dicer and moving L5 to re-image the output from
   L4. These images were taken with L5 in two positions. The first was out
   of focus without the Neutral Density (ND) filter, which meant that the
   arms had the same optics in place with and without the photonic-dicer.
   The second was with the image in focus and an ND filter in place to stop
   the camera from saturating.

Example science and reference images are shown in figures 6.7 (a) and (b) .

(a)   (b)
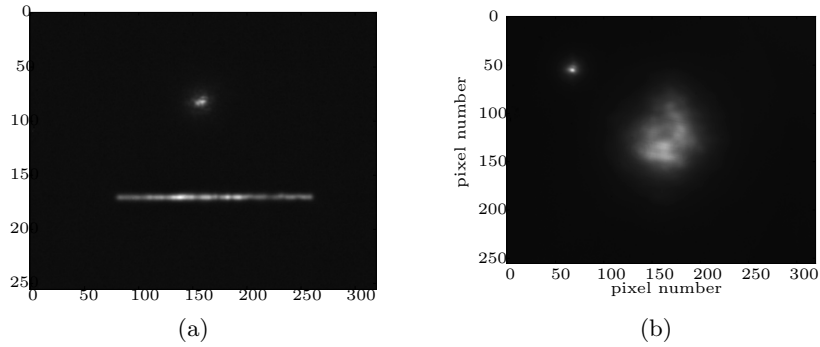
Figure 6.7: Examples of science and reference images produced by
the photonic-dicer after background subtraction. a) The reference
arm (top object) and slit (bottom object). b) The reference (top
left) and main arm reference (bottom). Note that this reference
image shows the defocussed reference.

The dark exposures were averaged and then subtracted from the other images
to remove the camera background and any hot or dead pixels. Once this was
done object identification was carried out using gaussian smoothing and then a
flood fill algorithm was applied to locate objects using joined pixels. Conditions
on the flooding algorithm were set to remove small objects such that only two
objects were identified in any frame. Once the objects were identified the flux
within that object on the actual image was calculated and stored.

In order to measure the throughput of the photonic-dicer the reference images were averaged. The ratio of the flux in the main arm to that of the reference arm was then taken for this average image. For each of the science images this ratio was also taken and then divided by the reference image ratio. This is shown in equation 6.1 where F_S is the flux in the slit, F_{RS} is the flux in the slit reference, F_R is the flux in the main arm of the averaged reference image and F_{RR} is the flux in the reference arm in the averaged reference image. This was done for all of the science images taken.

$$T = \frac{F_S F_{RR}}{F_R F_{SR}} \tag{6.1}$$

6.4.2 System Throughput

With the data reduction complete the throughput from the photonic-dicer for each of the science images could be calculated. The values were 20 ± 2 % for closed loop, $9\% \pm 2\%$ for tip-tilt and $10.5\% \pm 2\%$ for open loop. The errors are calculated standard deviations and the results for individual frames are plotted in figures 6.8 (b), 6.9 (b) and 6.10 (b) for closed loop, tip-tilt and open loop respectively. To illustrate the varying atmospheric conditions the averaged images are shown in figures 6.8 (a), 6.9 (a) and 6.10 (a). You can see that the averaged tip-tilt image has a larger spot size than the open-loop one. This means a lower flux coupled to the photonic-dicer, explaining the lower throughput, despite the higher correction level.

The photonic-dicer throughput was also measured in the laboratory, using monochromatic multimode laser light, in a manner similar to that described by [67]. These laboratory measurements showed a maximum throughput of $66\% \pm 3\%$ could be achieved for light in the 1320 nm to 1580 nm spectral region. This is significantly higher than the on-sky values, though this light was coupled

directly into the photonic-dicer using a multimode waveguide. This will be discussed in the next section.

(a)   (b)
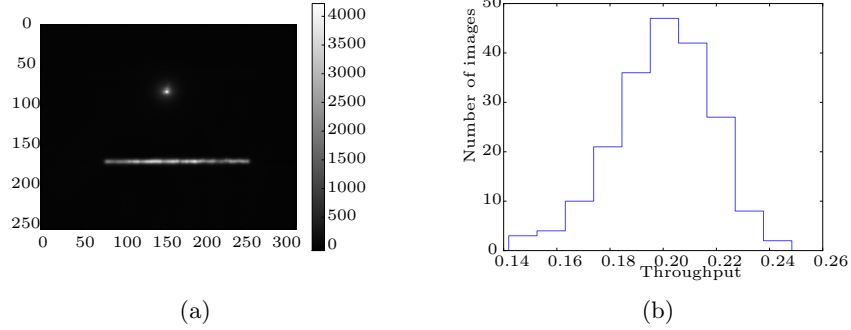
Figure 6.8: CANARY using closed-loop correction. a) The averaged frames from CANARY. The top is the re-imaged reference and the bottom is the slit. b) Histogram of the flux for closed-loop operation. The throughput is 20 ± 2 %.

(a)   (b)

Figure 6.9: CANARY using tip-tilt correction. a) The averaged frames from CANARY. b) Histogram of the flux for tip-tilt correction. The measured flux is $9\% \pm 2\%$.

6.4.3   PSF analysis

In the previous section there is a discrepancy of a factor of 2-3 between the lab measurements and on-sky throughput. This is due to the different methods used to measure the throughput. To quantify where the losses occurred the

(a)   (b)
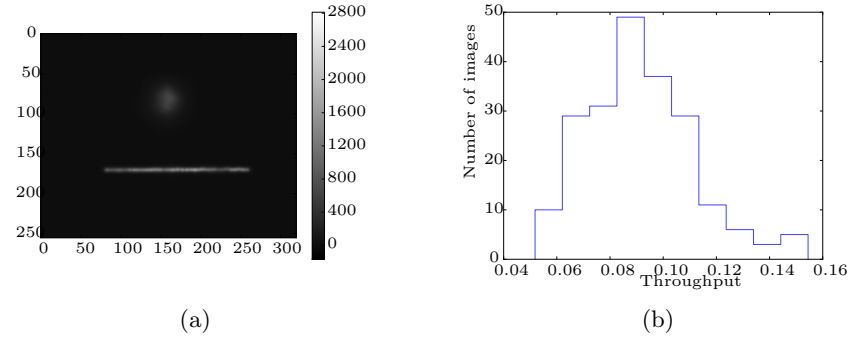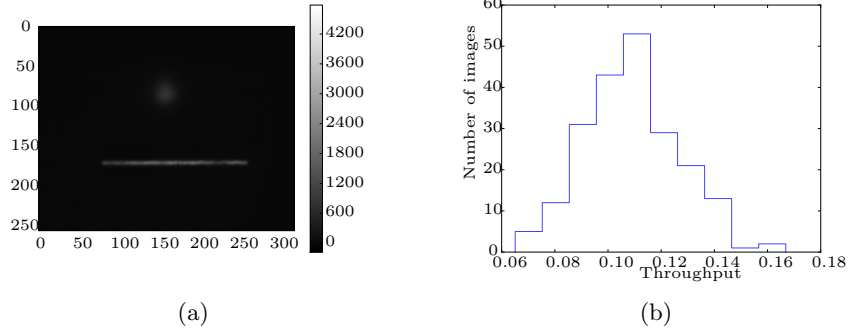
Figure 6.10: CANARY using open-loop correction. a) The averaged frames from CANARY. b) Histogram of the flux for open-loop correction.The measured flux is $10.5\% \pm 2\%$.

input needed to be examined. In the laboratory tests a multimode waveguide was placed against the input facet of the photonic-dicer, ensuring as much light coupled as possible. However in the on-sky experiment the photonic-dicer was designed to couple to the FWHM of the PSF. Next we analyse the produced images to calculate how much light had been coupled into the photonic-dicer.

To do this we need to know relative scaling between the reference and main arms. The output from CANARY is approximately an F/11 beam, with has a plate scale of 4.54 arcseconds mm^{-1}. With the lenses in the experiment this should have been converted to F/7.3 beam with a plate scale of 6.88 arcseconds mm^{-1}, meaning the photonic-dicer would have a spatial scale of ∼0.35 arcseconds on-sky in each axis. However to check the system worked as designed the magnification factor between the reference arm and the main arm was checked.

To do this the focussed reference images were averaged. The centre was found for both the main arm reference and reference arm image. The encircled energy was then calculated for both arms. This was normalised and then scaled so that the two curves were overlaid. The image is shown is shown in figure 6.11 (a) and the rescaled encircled energy in figure 6.11 (b).

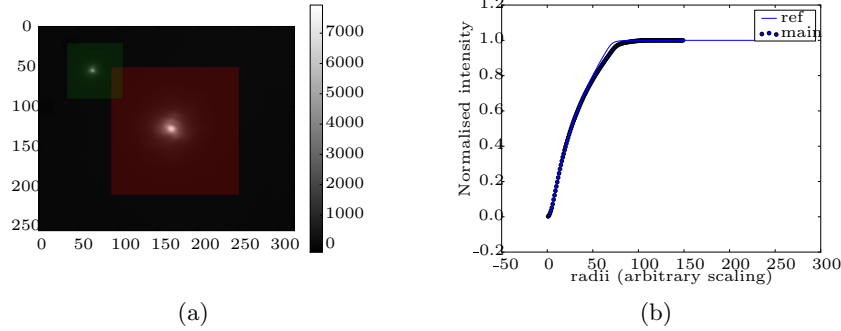(a)   (b)

Figure 6.11: The scaling between the main and reference arms.
a) The averaged reference from CANARY. The reference arm is
enclosed by the green box and the main arm by the red. b) The
rescaled encircled energy of the PSF, the reference arm is the solid
line and the main arm is the scattered data. Here the reference
arm is magnified by a factor of 2.8.

From figure 6.11 (b) you can see the best fit between the two arms occurs
at a magnification factor of 2.8, however according to the designs it should
have occurred at 3.29. This means the difference between the expected and
actual magnifications was 1.175. This could also have been a defocus term,
or other aberrations, though this would result in the shape of the enclosed
energy curve changing between the two PSFs, which does not appear to happen
except at the edges of the PSF. This could have occurred in one of three
places: in the reference arm, before the chip and after the chip. From the
measured positions and calculations in Zemax, changing the positions in the
reference arm by sensible amounts ($\sim$ 5mm, when compared to images taken of
the system) produced negligible errors in the magnification, due to the long focal
length of the lenses. This was also true of moving the lenses after the photonic-
dicer, where moving both lenses by $\sim$ 5mm produced a maximum error in the
magnification of 1.05. This means the cause of error is the lenses that image
CANARY onto the photonic-dicer.

This means that during the tests the photonic-dicer was injected with a beam

of F/6.2 giving a plate scale of 7.96 arcseconds mm^{-1}, meaning the angular size of the photonic-dicer was ∼0.405 arcseconds in each axis.

In order to quantify how much light was coupled into the photonic-dicer the science images were averaged and the centre of the photonic-dicer located from the averaged maximum in the reference arm. By taking the ensquared energy from this location the fractional energy coupled to the photonic-dicer in each image was calculated. This was compared to the calculated throughput and the results are shown in figure 6.12. The figure shows a linear increase in throughput with ensquared energy. This indicates that although there will be some coupling effects due to the mismatch between the CANARY PSF and the shape of the modes, the photonic-dicer still acts as a 'light-bucket' over the exposure time. This means to obtain the values of throughput for the photonic-dicer (not including coupling losses) the ensquared energy can be divided by the total throughput. A histogram of the photonic-dicer throughput for all AO modes is shown in figure 6.13 and the averaged throughput is 57% ± 4%. These results match well with the reported laboratory value, suggesting the methods used to compare throughput are compatible once the coupling losses are taken into account.

6.4.4 CANARY and spatial scaling

As shown in section 6.4.2 the improvement in throughput for the whole system with full AO correction was a factor of two improvement over no correction. This is a relatively low value for CANARY, which is designed to operate over spatial sizes (∼ 100mas), rather than the large spatial size of the photonic-dicer (∼ 400mas). In order to quantify how much light would have been coupled to the photonic-dicer the ensquared energy was calculated for the different AO modes at different spatial sizes. This is shown in figure 6.14. This shows the
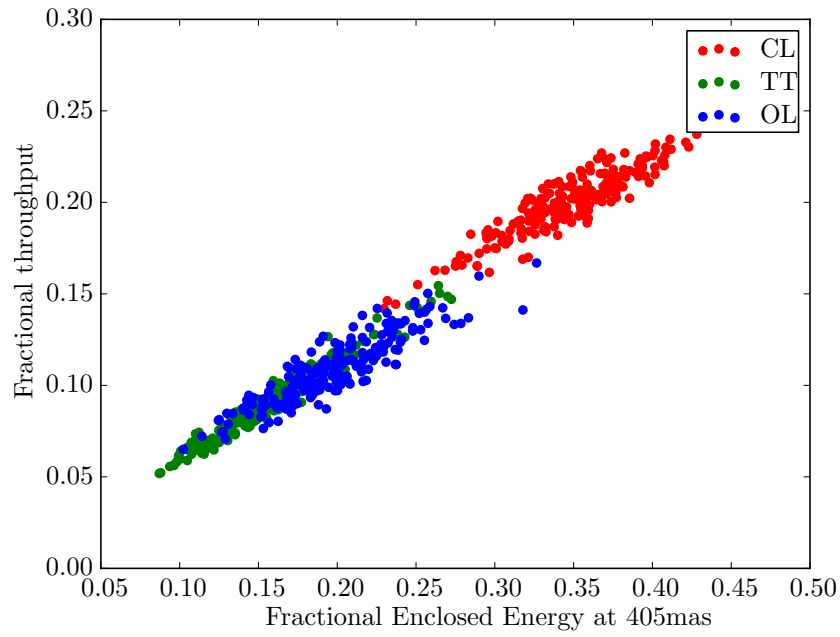
Figure 6.12: Throughput vs Ensquared Energy.   The measured throughput from the slit end of the photonic-dicer plotted against the ensquared energy from the reference arm at 405 mas. This is shown for the three AO-modes.
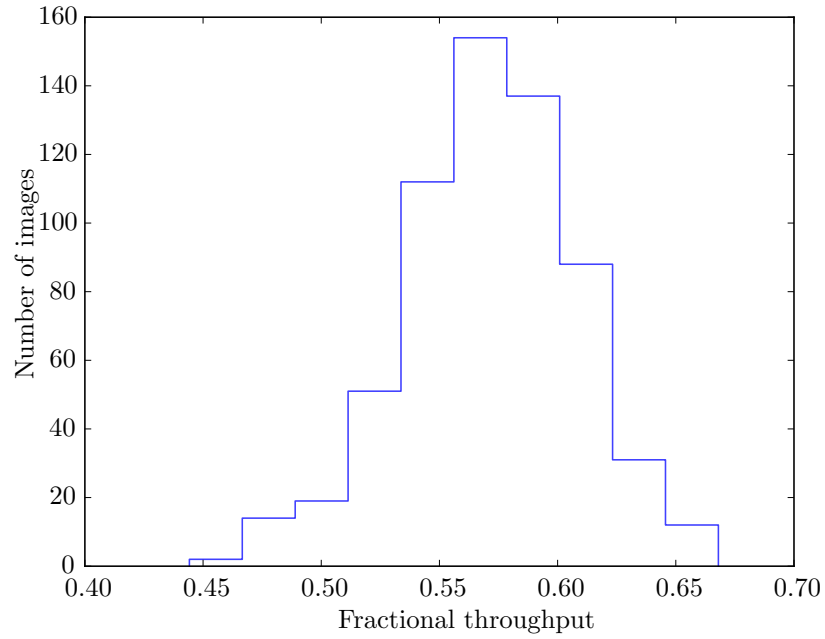
Figure 6.13: Histogram of the photonic-dicer throughput for all AO modes. This is the calculated throughput of the photonic-dicer, not including coupling losses from CANARY.

largest improvement in ensquared energy between the AO modes is at small spatial sizes, however in this form it is difficult to quantify the improvement.

To make this quantification easier it can also be shown as a ratio of ensquared energy with full and no AO correction over different spatial sizes. This is done by dividing the two levels of correction and is shown in figure 6.15. In this case the ensquared energy at the same angular size at the photonic-dicer shows a 2.3 times improvement (comparable to our previous results), but on the spatial sizes CANARY is designed to operate it is closer to a 6 times improvement. It must be noted that this relationship may show some variance over small timescales, as although the modes within an area can be estimated by equation 2.38 the actual mode coupling will depend upon the shape of the modes with the device and the PSF from the telescope.

This is an interesting result for both technologies. Whilst both aim for the smallest spatial sizes, resulting in few modes and a high relative throughput, they are required to operate slightly outside of this. Future devices will need to weigh up the cost of a high level AO system against the cost of detector pixels for a large photonic-dicer, or accept a loss of throughput.

6.4.5   Slit Analysis

In order to make use of the photonic-dicer for the concepts described in chapter 5 the output slit must be as uniform as possible along its length. This must be true of both the centring of the output along the slit and in terms of the width. In the low-resolution AWG version of the IPS, if the slit is not straight or varies in width this will result in losses when coupled to the AWG. In the high-resolution version of the IPS any variation in the width or centring will result in a degradation of spectral resolution (see chapter 2). Unlike the low resolution case it may be possible to calibrate this out in any attached spectragraph. However
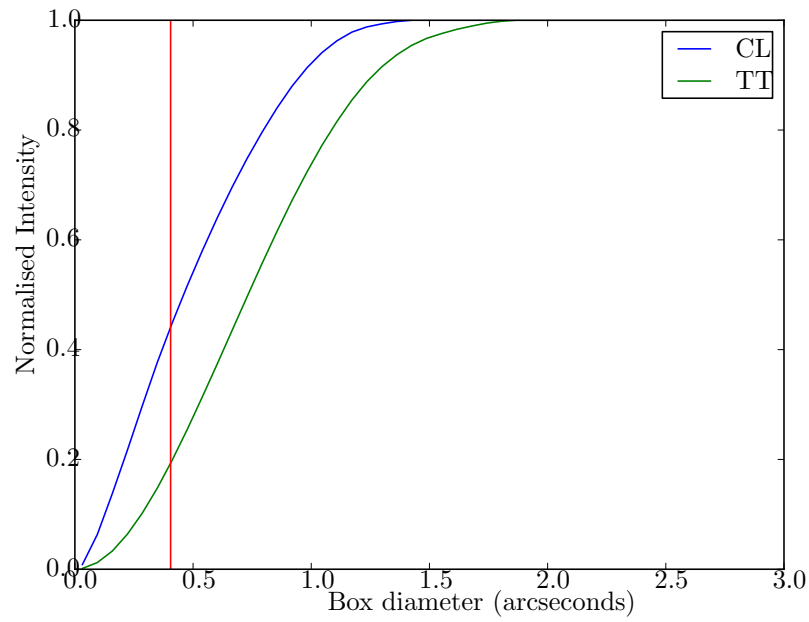
Figure 6.14: The ensquared energy for averaged images at the photonic-dicer input. Shown here for closed-loop (in blue) and tip-tilt (in green). The red vertical line indicates the angular size of our photonic-dicer.
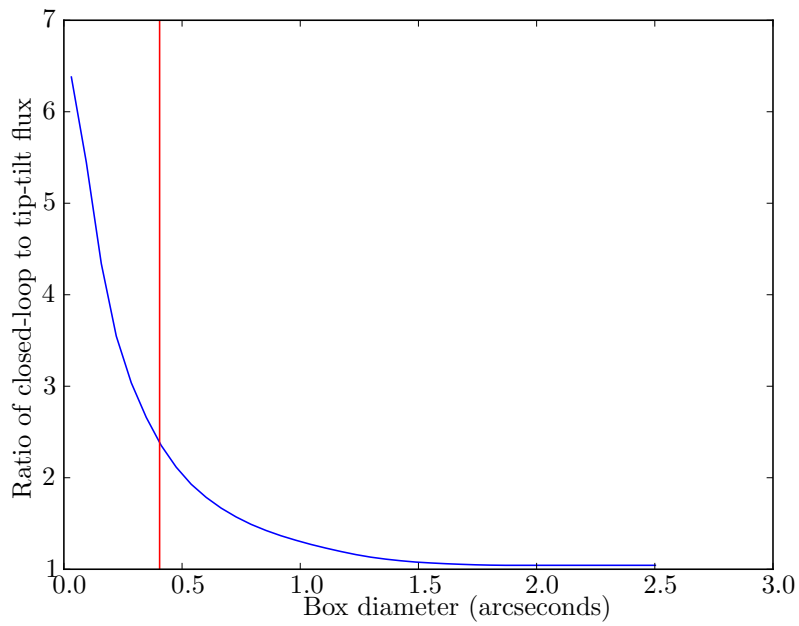
Figure 6.15: The ratio of ensquared energy for closed-loop and tip-tilt AO-modes. Here the advatange of using AO correction over small spatial sizes is shown. However as we increase the size of our ensquared energy box the advantage disappears.

this will almost certainly still result in a degradation of spectral resolution.

In order to analyse the uniformity of the slit along its length the centring was first analysed. This was done by taking the average of the on-sky data for the slit. A gaussian was fitted to each column of the slit, removing the far ends (see figure 6.16 (a) and (b) for an example). A straight line was fitted through the centre of the gaussians and the image rotated around this line to align the slit with the pixels. The gaussians were fitted again and the variation in the centre found, this is plotted in figure 6.17. This variation in centring is ~15% of the average fitted gaussian FWHM. This measurement was also repeated in the lab (by David G. MacLachlan) where measurements showed centring variations of 14%, 16%, 12%, 14% and 13% of the average fitted Gaussian FWHM. This would correspond to a ~15% reduction in spectral resolution if attached to a conventional spectrograph. No pattern could be found in the centring variation and further work would need to be done reducing manufacturing errors. This would be done by monitoring the system for drift during the writing process and better controlling variables such as lab temperature. With this straightening complete a final device could be produced.

Once the variation in centring for each column was identified it was then removed. This meant all the fitted gaussians for the averaged slit were centred around 0. This enabled analysis of an idealised straight slit with no manufacturing errors. The centres for each frame and column were plotted again and still showed a residual movement in the centring (see figure 6.18). To check if this was an effect of the camera, gaussians centred around 0 with the same noise as the camera were produced (see figure 6.19 (a)). These had centres fitted and the results of the model were found. These had a slightly narrower fit than the data, although were for an idealised case (see figure 6.19 (b)).

The width of each gaussian was then analysed for each column in each image.

(a)
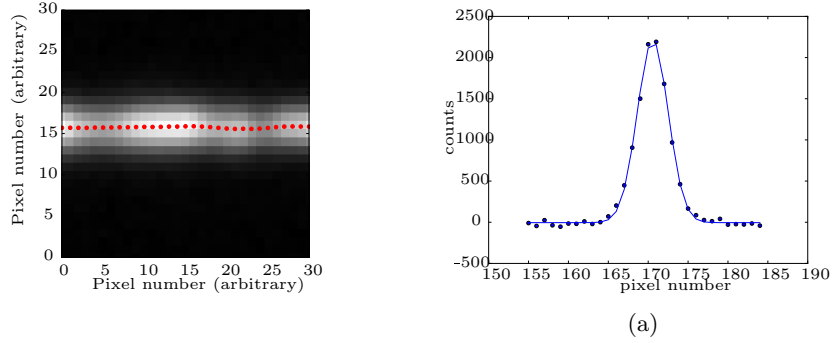
Figure 6.16: The centring of the slit. (a) The colour map plot shows
a section of the slit, with the fitted centres of the gaussian for each
column (vertical) shown in red. (b) An example of the data for a
single column of the slit with the fitted gaussian overlaid.

It was found to vary by a maximum of $\sim 20\%$ of the fitted gaussian FWHM (see

figure 6.20). Histograms were plotted for each frame (time) and each column

(position). The histograms showed very little variation in time and large varia-

tions in position. This indicates that the slit had different properties at different

points and differing mode field sizes possibly due to differing refractive indices.

These would need to be made equal in future devices. The same measurements

were also performed in the lab (by David G. MacLachlan) and showed width

variations of 16%, 14%, 18%, 20% and 18% of the average fitted Gaussian

FWHM, for 1320 nm, 1400 nm, 1500 nm, 1550 nm and 1580 nm respectively.

6.5   Conclusions

We have created a device which reformats the PSF from the telescope into

a long diffraction-limited slit. We call this device the photonic-dicer. It has

the potential to allow for a more stable spectrograph input for high resolution

spectroscopy, or provide a stable input for a photonic spectrograph. It was

designed to be matched to the FWHM of the CANARY AO system and was

Figure 6.17: Histogram of the fitted centres of the slit. This shows the fitted positions of the slit against pixel position. As shown by the graph the variation is sub pixel, though definitely noticeable. No pattern is found.
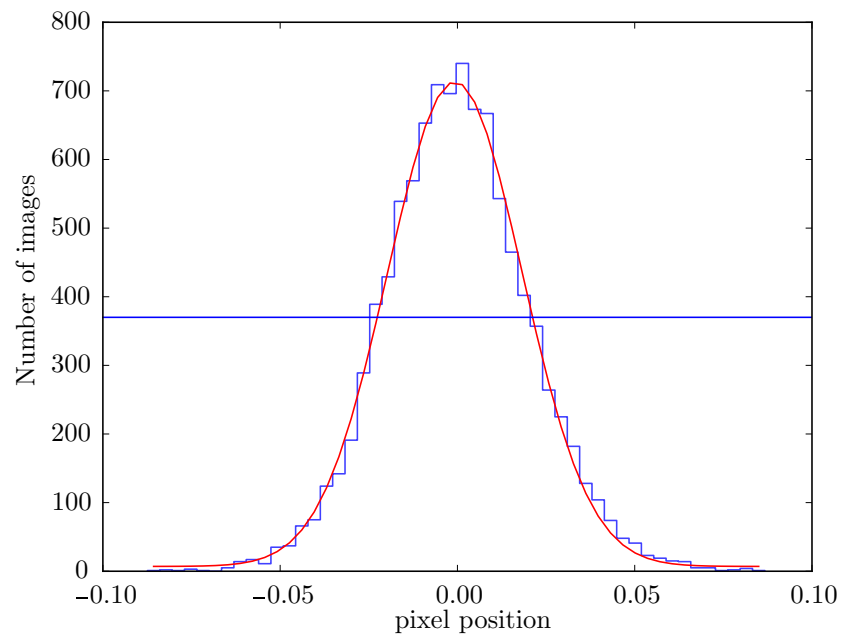
Figure 6.18: The slit centring after removal of manufacturing errors. A histogram of the data is shown in blue and a fitted gaussian shown in red. The horizontal blue line is the full width half maximum.

(a)   (b)

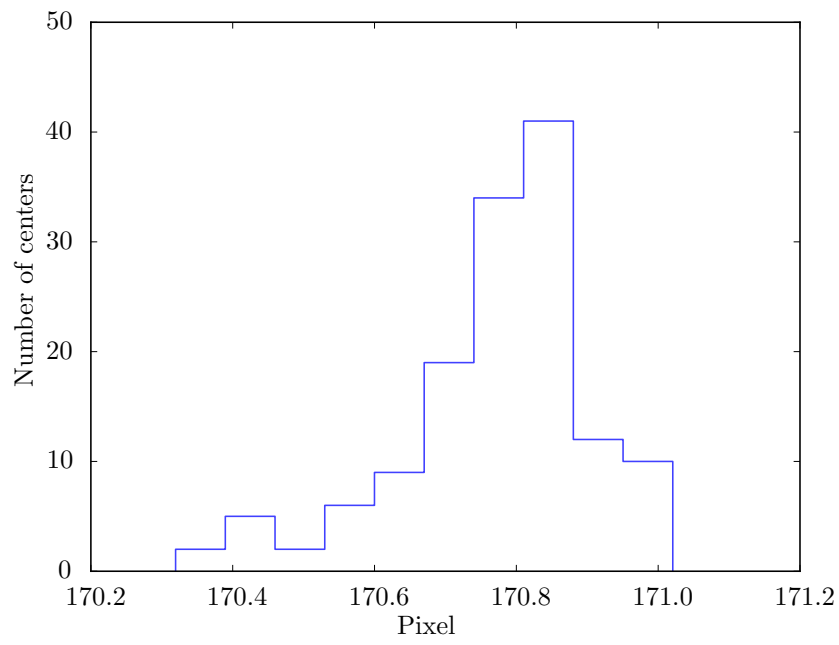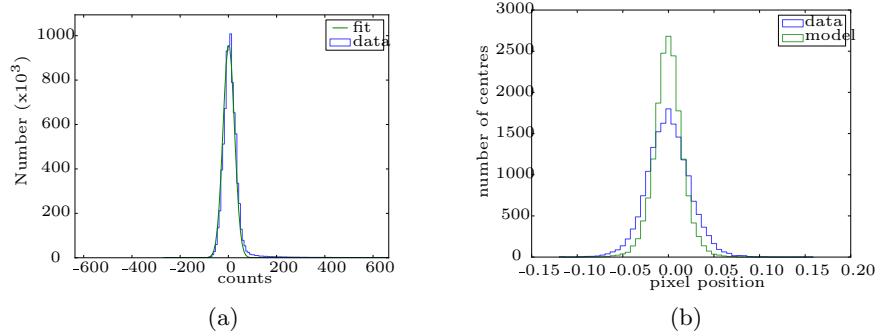Figure 6.19: The modelling of the idealised slit. (a) The calculated camera noise with the actual data shown in blue and the fit shown in green. (b) The resulting histogram for the centring of the slit and the modelling of the slit, note that this differs slightly from 6.18 due to differing bin sizes.

composed of 36 single mode waveguides arranged in a square configuration (6x6) at the input and a rectangular (1x36) output. We designed and built it in the Summer of 2013 and tested it on the WHT in September with the CANARY AO system.

The on-sky experimental setup for the photonic-dicer showed a throughput of 20 ± 2 % for closed loop, $9\% \pm 2\%$ for tip-tilt and $10.5\% \pm 2\%$ for open loop AO modes respectively. The lower values for the tip-tilt mode were due to the worse seeing conditions at the time, this increased the size of the PSF lowering the amount of light coupled into the photonic-dicer. This was a factor of 2-3 lower than the throughput measured in the laboratory of $66\% \pm 3\%$ and was due to differing methods used to measure the throughput.

In order to determine the losses at each part of the system the reference images were analysed. First the focussed reference image was analysed and the relative magnification between the two experimental arms was calculated. This was then used to work out the scaling of the reference images compared to the slit images. The ensquared energy corresponding to the size of the input to the
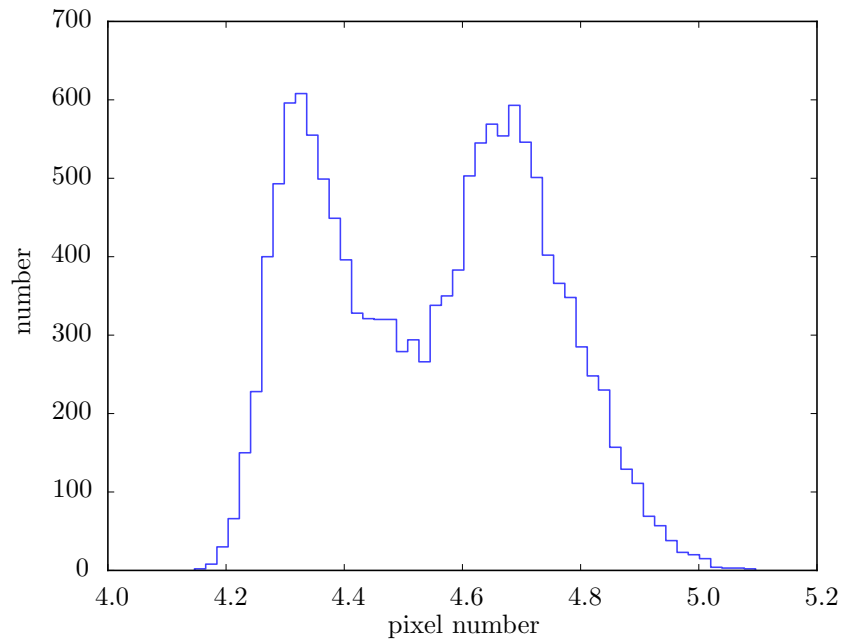
Figure 6.20: The slit width (FWHM) of the fitted gaussian in pixels. Note the bimodal nature of the slit widths.This indicates that the modes of the output slit tend to be two different sizes, with variations in between, this bimodality would need to be removed in a full device. Further analysis showed this as position dependent, not time dependent. This indicates the modes are not varying with time, which is very important for a stable spectrograph.

dicer was calculated and showed that the total throughput increased linearly with ensquared energy. This meant the throughput of the photonic-dicer could be calculated as $57\% \pm 4\%$, when coupling losses were taken into account. This closely matched the laboratory values for throughput.

The advantages of combining an AO system such as CANARY and a photonic-dicer were then analysed. Both systems are optimised to work on smaller spatial sizes, though this leads to losses as less light is coupled. Future instrumentation will need to weigh up the need for throughput against the required complexity (and hence cost) of an AO system or the number of modes in a photonic-dicer.

Finally the slit was analysed for uniformity along its length, both in terms of centring and width. The centring was found to vary by $\sim 15\%$ of the slit width along its length. This manufacturing error will need to be removed from any future devices. The width was found to vary by $\sim 20\%$ of the slit width. This variation was determined to be constant in time and varied with the position of the slit. This will need to be investigated in future devices.

Chapter 7

Conclusions

This thesis has investigated the potential of the IPS and its components within astronomical instrumentation. This was achieved through both modelling and experiment. Here we provide a synopsis of the chapters, discuss the place of the work within the field, and conclude with further possible areas of investigation.

7.1   Chapter Synopsis

In chapter 2 we introduced the basic theory of spectroscopy, detailing it for both conventional astronomical instrumentation and photonic instrumentation. We then described the devices and procedures required to connect the single mode photonic instrumentation to a multimode telescope. Finally we described the work that has already been done in the area of photonic spectroscopy. This chapter is mostly based upon the work of others, though contains some original work.

In chapter 3 we examined the application of Integrated Photonic Spectrographs in astronomy and showed that a PL or reformatter is equivalent in function to an image slicer. We showed that as the telescope diameter increases, the

145

size of an IPS must also increase (provided that the slit is not matched to the diffraction-limit) due to the increase in number of modes in the field (equivalent to the number of diffraction-limited slices). We also showed that the number of modes in a field is independent of how the field is initially sampled (the size of the sampling element (spaxel) has no effect on the total number of modes in the field).

We modelled IPS instruments to compare them with conventional instruments on large telescopes and found that they require 10^3-10^5 Arrayed Waveguide Gratings (AWGs) or 10^3-10^4 replica spectrographs if bulk optics are used for instruments on 8m and 30m telescopes. It should be noted that all of our instruments sampled many spaxels and only one had AO. We found that fully-photonic instruments were comparable in size to their conventional counterparts but only if the AWG was close to the diffraction limit. The semi-photonic instruments were found to be much larger, due to the redundancies of having multiple spectrographs. We have also found that unless the input image is sampled near the diffraction-limit, the number of component spectra in each spaxel is very high, requiring large numbers of pixels in the detector array. This is equivalent to oversampling the PSF and could also potentially increase detector noise in the instrument.

To combat the problem of size we considered the effect of adding extra inputs to the AWG to reduce the number of AWGs required. However the resulting instrument was of the same size or larger. It also means that the problem of oversampling in the linear case remains unsolved and potentially will be worse since the spectra will need to have gaps between them to distinguish them.

We also examined other options for reducing the number of detector pixels and/or AWGs and concluded that instruments of photonic construction may be viable depending on the extent to which performance (including throughput,

spectral resolution and spatial multiplex) can be traded against cost.

Even without these modifications or restrictions, we found there are some areas where IPSs may offer a significant advantage. This includes spectroscopy of objects near the diffraction-limit, e.g. single objects with high-order AO such as in exoplanet studies. Another is low-resolution multiplexed spectroscopy working in the few-mode limit.

In chapter 4 we used simplified models for both a conventional echelle model and an AWG model to simulate the size and number of detector pixels of GNIRS on Gemini. We then varied spectral resolution, telescope diameter, sample size and FOV. Our results were presented in terms of the scale length (cube root of the volume) of the instrument and the number of detector pixels the instrument will require. Our findings suggested that photonic spectroscopy would be most useful on small instruments with diffraction-limited seeing, or a small telescope. We also showed that if high resolution devices could be produced they could potentially be smaller than conventional instrumentation. We found that the IPS instrument will be on the same magnitude in terms of size as a conventional spectrograph, but will have more detector pixels if the input is not diffraction-limited.

From this we examined which science cases put forward by the ASTRONET [90] and ReSTAR reports [91] were near diffraction-limited, had a small FOV and were in the near IR. We found that there are multiple cases for the development of the IPS at both low and high spectral resolution. If an IPS could be shown to be cheaper and more stable than a conventional spectrograph then it could complement or replace certain types of instrumentation on existing telescopes.

In chapter 5 we examined various design concepts for the IPS. We looked at their relative strengths and weaknesses in terms of throughput, spectral resolu-

tion, FSR, number of detector pixels required, the number of AWGs or spectrographs required, the instrument size per spaxel and any briefly detailed potential difficulties with manufacture. All of the concepts described here tradeoff with the above metrics. As such the science case will determine which is most useful within astronomy.

Due to the simplicity of manufacture and number of pixels, we identified two preferred concepts. Our first preference was for the AWG with slit input as it uses existing technologies and could potentially provide low resolution integrated spectrographs, though with a limited FSR. This provides an integrated and robust spectrograph, that could potentially take advantage of current technologies.The second is the long slit with a conventional spectrograph behind. This would be a high resolution spectrograph and would take advantage of the stability offered by using single mode technologies. It reduces pixel numbers and is very similar to existing concepts. Both of these concepts require the demonstration of an efficient lantern/slit reformatter.

Finally, we noted that there are areas including removal of the OH lines from the IR spectrum [100] and astrocombs to increase stability [116] which we did not explore, where photonic components could provide additional advantages. These would also need to be considered in future science cases and instrument designs.

In chapter 6 we created a device which reformats the PSF from the telescope into a long diffraction-limited slit. We called this device the photonic-dicer. It has the potential to allow for a more stable spectrograph input for high resolution spectroscopy, or to provide a stable input for a photonic spectrograph. It was designed to be matched to the FWHM of the CANARY AO system and was composed of 36 single mode waveguides arranged in a square configuration (6x6 SM waveguide) at the input and a rectangular (1x36 SM waveguide) output.

We designed and built it in the Summer of 2013 and tested it on the WHT in September with the CANARY AO system.

The on-sky experimental setup for the photonic-dicer showed a throughput of 20 ± 2 % for closed loop, 9% ± 2% for tip-tilt and 10.5% ± 2% for open loop AO modes respectively. The lower values for the tip-tilt mode were due to the worse seeing conditions at the time. This was a factor of 2-3 lower than the throughput measured in the laboratory of 66% ± 3% and was due to differing methods used to measure the throughput.

In order to determine the losses at each part of the system the reference images were analysed. First the focussed reference image was analysed and the relative magnification between the two experimental arms was calculated. This was then used to work out the scaling of the reference images compared to the slit images. The ensquared energy corresponding to the size of the input to the dicer was calculated and showed that the total throughput increased linearly with ensquared energy. This shows that over the length of the exposures the photonic-dicer acts as a 'light bucket'. This meant the throughput of the photonic-dicer could be calculated as 57% ± 4% when coupling losses were taken into account. This closely matches the laboratory values for throughput.

The advantages of combining an AO system such as CANARY and a photonic-dicer were then analysed. Both systems are optimised to work on smaller spatial sizes, though this leads to coupling losses as on smaller spatial sizes not all the light is coupled. Future instrumentation will need to weigh up the need for throughput against the required complexity (and hence cost) of the AO system or the size of the photonic-dicer.

Finally the slit was analysed for uniformity along its length, both in terms of centring and width. The centring was found to vary by ∼11% along its length. This manufacturing error will need to be removed from any future devices. The

width was found to vary by ∼10%. This variation was determined to be constant in time and varied with the position of the slit.

7.2   This work within Astrophotonics

Since its inception the field of astrophotonics has rapidly expanded, The IPS is one of many developments in the field. Whilst the IPS initially conceived in part as a solution to the problems of spiralling costs and sizes faced by modern astronomy, other advantages of working in the single mode regime have been shown to exist. These include Fibre Bragg Grating (FBG) and the potential for improved stability. The first generation of instruments showed various principles worked (e.g. [117, 72, 3, 5, 8]), though with a lower performance than conventional instrumentation. They were also not optimised for any particular science cases.

As such astrophotonics is still trying to find its place within astronomy. Whilst there is growing interest in the field, the precise areas where it could be applied have until recently been relatively undefined. Small scale studies showing the validity of using photonic components have been done [57], though they were not considered in relation to conventional instrumentation. This thesis contains the first quantitate comparison of the IPS with conventional instrumentation, basing its methodology on that developed in [76]. Further studies such as this will be essential to understand which science cases astrophotonic instruments could be applied to.

Now that the first generation of devices have proved the principles of using photonic instrumentation within astronomy, the second generation needs to show it has the potential to compete with conventional instrumentation in chosen arenas (e.g. [6, 8, 19, 104]). In particular the IPS needs to be redesigned in order to compete both in terms of size and number of detector pixels (see

chapter 5). Various designs have been proposed (e.g. [6, 105, 88]) and our photonic-dicer (see chapter 6) sits in this generation of instrumentation. It is an enabling component that has the potential to increase the stability of conventional high resolution spectroscopy (other concepts include [88, 6]) or create a mass producible low resolution integrated spectrograph. In addition its integration with the CANARY AO system is the first demonstration of its type which is essential for any future IPS on a large telescope.

Future instrumentation will also require larger scale demonstrators or full instrumentation suites and some of these are being trialled (e.g. [118]). This will require larger investment. In particular if these technologies are to be used on large telescopes, further testing on smaller telescopes is essential to proving the viability in terms of costs and scalability.

7.3 Further Work

There are three main areas for future work from this thesis they are as follows:

Further comparative studies

The work detailed in chapter 3 and 4 could be expanded. In particular adding in new types of instruments operating in different regimes (e.g. types of AO correction, space based) the new designs of instruments and creating costs metrics for the instruments (such as those detailed in [57]).This could also be extended to other types of instrumentation, such as the work in [119].

Further studies of the current photonic-dicer

There are still opportunities for further analysis of the data taken from the on-sky run of the photonic-dicer. Areas include:

- Further analysis of the PSF data from CANARY. In particular theoretical calculations of how the PSF from CANARY couples to the modes of the photonic-dicer in each frame taken. This would help with further understanding of how the instrument works and help improve future designs.

- CANARY stores additional data on the atmospheric conditions during observations. This would be very useful for matching seeing in each frame to the throughput of the device. This will require reconstruction of the slopes data.

Future instrument design

The photonic-dicer detailed in chapter 6 showed promise as an image slicer, however there were also areas for improvement.

- A future photonic-dicer can be further optimised. The design could be improved through careful modelling of the transitions between the differing sections of the photonic-dicer. This would allow the shortest lengths for all transitions without suffering from bend-losses. This would make the photonic-dicer shorter and increase its throughput. There is also potential to increase mode coupling in the transitions by re-arranging the order of the waveguides within the photonic-dicer. For more information see [120]. The manufacturing process of the photonic-dicer could also be improved. This could be done by monitoring the uniformity along the length of the slit and the refractive index of the waveguides. There is also potential for other more transmissive glasses to be used.

- The coupling between the photonic-dicer and AO system could be optimised. This could either be done by changing the shape of the input to the photonic-dicer or by shaping the output of the AO system. Modelling both the outputs that an AO system could make and the supported modes

that differing photonic-dicer designs could support would potentially be very useful here.

- There is great scope for a full instrumentation suite to be developed. As stated in chapter 5 a photonic-dicer could feed either an AWG to produce a low resolution output or a high resolution conventional spectrograph. This would require design and development for both concepts. For the first instrument an AWG would need to be developed with a high resolution, such that it could be degraded by the input slit. The second instrument would need to be stable to take full advantage of the stability in the slit, this would require careful design work. The above would also test the spectral response of the photonic-dicer, which so far has only been measured in the laboratory.

- The photonic-dicer could also be used as a wavefront sensor by connecting it to a linear detector array. This would potentially allow a very fast readout time, increasing the precision of the wavefront measurement. This would require the investigation of the spectral response of the photonic-dicer and the matching between its input and output.

Bibliography

[1] D. Lee and J. R. Allington-Smith. An experimental investigation of immersed gratings. *Monthly Notices of the Royal Astronomical Society*, 312(1):57–69, February 2000.

[2] Sir Isaac Newton. *Opticks, or a treatise of the reflections, refractions, inflections and colours of light.* William Innys, 1730.

[3] N. Cvetojevic, J. S. Lawrence, S. C. Ellis, J. Bland-Hawthorn, R. Haynes, and A. Horton. Characterization and on-sky demonstration of an integrated photonic spectrograph for astronomy. *Optics Express*, 17:18643–18650, October 2009.

[4] Nick Cvetojevic, Nemanja Jovanovic, Joss Bland-hawthorn, Roger Haynes, and Jon Lawrence. Miniature Spectrographs : Characterization of Arrayed Waveguide Gratings for Astronomy. *Library*, 7739(May 2011):1–7, 2010.

[5] N. Cvetojevic, N. Jovanovic, J. Lawrence, M. Withford, and J. Bland-Hawthorn. Developing arrayed waveguide grating spectrographs for multi-object astronomical spectroscopy. *Optics Express*, 20:2062, January 2012.

[6] N Cvetojevic, HNJ Fernando, N Jovanovic, JS Lawrence, R Haynes, J Bland-Hawthorn, and MJ Withford. High-resolution integrated photonic micro-spectrographs for radial velocity exoplanet astronomy. In *Lasers and Electro-Optics Europe (CLEO EUROPE/IQEC), 2013 Conference on and International Quantum Electronics Conference*, pages 1–1. IEEE, 2013.

[7] Etienne Le Coarer, Sylvain Blaize, Pierre Benech, Ilan Stefanon, Alain Morand, Gilles Lérondel, Grégory Leblond, Pierre Kern, Jean Marc Fedeli, and Pascal Royer. Wavelength-scale stationary-wave integrated fourier-transform spectrometry. *Nature Photonics*, 1(8):473–478, 2007.

[8] J. Bland-Hawthorn, S.C. Ellis, S.G. Leon-Saval, R. Haynes, M.M. Roth, H.-G. Löhmannsröben, a.J. Horton, J.-G. Cuby, T.A. Birks, J.S. Lawrence, P. Gillingham, S.D. Ryder, and C. Trinh. A complex multinotch astronomical filter to suppress the bright infrared sky. *Nature Communications*, 2:581, December 2011.

[9] Christopher Q Trinh, Simon C Ellis, Joss Bland-Hawthorn, Jon S Lawrence, Anthony J Horton, Sergio G Leon-Saval, Keith Shortridge, Julia Bryant, Scott Case, Matthew Colless, et al. Gnosis: the first instrument to use fiber bragg gratings for oh suppression. *The Astronomical Journal*, 145(2):51, 2013.

[10] Joss Bland-Hawthorn and Pierre Kern. Astrophotonics: a new era for astronomical instruments. *Optics Express*, 17(3):1880–1884, 2009.

[11] R R Thomson, G Brown, A K Kar, and T A Birks. An Integrated Fan-Out Device for Astrophotonics. *Engineering*, 2:7–8, 2010.

[12] N Jovanovic, PG Tuthill, B Norris, S Gross, P Stewart, N Charles, S Lacour, M Ams, JS Lawrence, A Lehmann, et al. Starlight demonstration of the dragonfly instrument: an integrated photonic pupil-remapping interferometer for high-contrast imaging. *Monthly Notices of the Royal Astronomical Society*, 427(1):806–815, 2012.

[13] I. Spaleniak, N. Jovanovic, S. Gross, M. J. Ireland, J. S. Lawrence, and M. J. Withford. Integrated photonic building blocks for next-generation astronomical instrumentation II: the multimode to single mode transition. *Optics Express*, 21:27197, November 2013.

[14] F. G. Watson. Multifiber waveguide spectrograph for astronomy. In S. C. Barden, editor, *Fiber Optics in Astronomical Applications*, volume 2476 of *Society of Photo-Optical Instrumentation Engineers (SPIE) Conference Series*, pages 68–74, June 1995.

[15] J. Bland-Hawthorn and A.J. Horton. Instruments without optics: an integrated photonic spectrograph. *Proceedings of SPIE*, 6269:21–34, June 2006.

[16] R. J. Harris and J. R. Allington-Smith. Applications of Integrated Photonic Spectrographs in astronomy. *MNRAS*, 428:3139–3150, February 2013.

[17] R. J. Harris and J. R. Allington-Smith. Modelling the application of integrated photonic spectrographs to astronomy. In *Society of Photo-Optical Instrumentation Engineers (SPIE) Conference Series*, Society of Photo-Optical Instrumentation Engineers (SPIE) Conference Series, 2012.

[18] RJ Harris, JR Allington-Smith, David MacLachlan, and Robert R Thomson. A comparison of concepts for a photonic spectrograph. In *SPIE Astronomical Telescopes+ Instrumentation*, pages 91474C–91474C. International Society for Optics and Photonics, 2014.

[19] R. J. Harris, D. G. MacLachlan, D. Choudhury, T. J. Morris, E. Gendron, A. G. Basden, G. Brown, J. R. Allington-Smith, and R. R. Thomson. Photonic spatial reformatting of stellar light for diffraction-limited spectroscopy. *ArXiv e-prints*, February 2014.

[20] J. Allington-Smith. 3D Instrumentation. In M. Kissler-Patig, J. R. Walsh, and M. M. Roth, editors, *Science Perspectives for 3D Spectroscopy*, pages 3–540, 2007.

[21] E. Hecht. *Optics*. Addison-Wesley, 4th edition, 1998.

[22] R Foy and F.C Foy. *Optics in astrophysics*. Springer, 1st, edition, 2002.

[23] George R Harrison. The production of diffraction gratings i. development of the ruling art. *JOSA*, 39(6):413–426, 1949.

[24] Dainis Dravins. High-dispersion astronomical spectroscopy with holographic and ruled diffraction gratings. *Applied optics*, 17(3):404–414, 1978.

[25] Samuel C Barden, James A Arns, and Willis S Colburn. Volume-phase holographic gratings and their potential for astronomical applications. In *Astronomical Telescopes & Instrumentation*, pages 866–876. International Society for Optics and Photonics, 1998.

[26] Willard S Boyle and George E Smith. Charge coupled semiconductor devices. *Bell System Technical Journal*, 49(4):587–593, 1970.

[27] GF Amelio, MF Tompsett, and GE Smith. Experimental verification of the charge coupled device concept. *Bell System Technical Journal*, 49(4):593–600, 1970.

[28] KJ Bachmann and JL Shay. An ingaas detector for the 1.0–1.7-μm wavelength range. *Applied Physics Letters*, 32(7):446–448, 1978.

[29] S. Meeker, B. A. Mazin, K. O'Brien, S. McHugh, B. Bumble, E. Langman, and M. Navaroli. First Optical Observations with Microwave Kinetic Inductance Detectors. In *American Astronomical Society Meeting Abstracts 219*, volume 219 of *American Astronomical Society Meeting Abstracts*, page 413.06, January 2012.

[30] A. Peacock, P. Verhoeve, N. Rando, A. van Dordrecht, B. G. Taylor, C. Erd, M. A. C. Perryman, R. Venn, J. Howlett, D. J. Goldie, J. Lumley, and M. Wallis. Single optical photon detection with a superconducting tunnel junction. *Nature*, 381:135–137, May 1996.

[31] R. W. Romani, A. J. Miller, B. Cabrera, E. Figueroa-Feliciano, and S. W. Nam. First Astronomical Application of a Cryogenic Transition Edge Sensor Spectrophotometer. *Astrophysical Journal Letters*, 521:L153–L156, August 1999.

[32] Benjamin A Mazin, Kieran O'Brien, Sean McHugh, Bruce Bumble, David Moore, Sunil Golwala, and Jonas Zmuidzinas. Archons: a highly multiplexed superconducting optical to near-ir camera. In *SPIE Astronomical Telescopes+ Instrumentation*, pages 773518–773518. International Society for Optics and Photonics, 2010.

[33] Richard S Ellis and Ian R Parry. Multiple object spectroscopy. In *Instrumentation for Ground-Based Optical Astronomy*, pages 192–208. Springer, 1988.

[34] J Allington-Smith. Basic principles of integral field spectroscopy. *New Astronomy Reviews*, 50(4-5):244–251, June 2006.

[35] G. J. Murray and J. R. Allington-Smith. Strategies for spectroscopy on Extremely Large Telescopes. II - Diverse field spectroscopy. *MNRAS*, August 2009.

[36] G Comte and C Surace. Slitless spectroscopy with photographic and ccd detectors across large fields. In *Astronomy from Wide-Field Imaging*, pages 709–714. Springer, 1994.

[37] Chris G. Tinney. IRIS2: a working infrared multi-object spectrograph and camera. *Proceedings of SPIE*, 5492(May 2011):998–1009, 2004.

[38] Oliver LeFevre, Michel Saïsse, Dario Mancini, Sylvie Brau-Nogué, Oreste Caputi, Louis Castinel, Sandro d'Odorico, Bianca Garilli, Markus Kissler-Patig, Christian Lucuix, et al. Commissioning and performances of the vlt-vimos. In *Astronomical Telescopes and Instrumentation*, pages 1670–1681. International Society for Optics and Photonics, 2003.

[39] Robert Sharp, Will Saunders, Greg Smith, Vladimir Churilov, David Correll, John Dawson, Tony Farrel, Gabriella Frost, Roger Haynes, Ron Heald, et al. Performance of aaomega: the aat multi-purpose fiber-fed spectrograph. In *Astronomical Telescopes and Instrumentation*, pages 62690G–62690G. International Society for Optics and Photonics, 2006.

[40] Masahiko Kimura, Toshinori Maihara, Kouji Ohta, Fumihide Iwamuro, Sigeru Eto, Masafumi Lino, Daisaku Mochida, Takanori Shima, Hiroshi Karoji, Junichi Noumaru, et al. Fibre-multi-object spectrograph (fmos) for subaru telescope. In *Astronomical Telescopes and Instrumentation*, pages 974–984. International Society for Optics and Photonics, 2003.

[41] Pierre Bely. *The design and construction of large optical telescopes.* Springer, 2003.

[42] S. A. Smee, J. E. Gunn, A. Uomoto, N. Roe, D. Schlegel, C. M. Rockosi, M. A. Carr, F. Leger, K. S. Dawson, M. D. Olmstead, J. Brinkmann, R. Owen, R. H. Barkhouser, K. Honscheid, P. Harding, D. Long, R. H. Lupton, C. Loomis, L. Anderson, J. Annis, M. Bernardi, V. Bhardwaj, D. Bizyaev, A. S. Bolton, H. Brewington, J. W. Briggs, S. Burles, J. G. Burns, F. J. Castander, A. Connolly, J. R. A. Davenport, G. Ebelke, H. Epps, P. D. Feldman, S. D. Friedman, J. Frieman, T. Heckman, C. L. Hull, G. R. Knapp, D. M. Lawrence, J. Loveday, E. J. Mannery, E. Malanushenko, V. Malanushenko, A. J. Merrelli, D. Muna, P. R. Newman, R. C. Nichol, D. Oravetz, K. Pan, A. C. Pope, P. G. Ricketts,

A. Shelden, D. Sandford, W. Siegmund, A. Simmons, D. S. Smith, S. Snedden, D. P. Schneider, M. SubbaRao, C. Tremonti, P. Waddell, and D. G. York. The Multi-object, Fiber-fed Spectrographs for the Sloan Digital Sky Survey and the Baryon Oscillation Spectroscopic Survey. *The Astronomical Journal*, 146:32, August 2013.

[43] C Marc Dubbeldam, Jeremy R Allington-Smith, Serge Pokrovski, and David J Robertson. Integral field unit for the gemini near-infrared spectrograph. In *Astronomical Telescopes and Instrumentation*, pages 1181–1192. International Society for Optics and Photonics, 2000.

[44] Peter J McGregor, John Hart, Peter G Conroy, Murray L Pfitzner, Gabe J Bloxham, Damien J Jones, Mark D Downing, Murray Dawson, Peter Young, Mark Jarnyk, et al. Gemini near-infrared integral field spectrograph (nifs). In *Astronomical Telescopes and Instrumentation*, pages 1581–1591. International Society for Optics and Photonics, 2003.

[45] Roger Bacon, Yannick Copin, G Monnet, Bryan W Miller, JR Allington-Smith, M Bureau, C Marcella Carollo, Roger L Davies, Eric Emsellem, Harald Kuntschner, et al. The sauron project–i. the panoramic integral-field spectrograph. *Monthly Notices of the Royal Astronomical Society*, 326(1):23–35, 2001.

[46] Jeremy Allington-Smith, Graham Murray, George Dodsworth, Roger Davies, Bryan W Miller, Inger Jorgensen, Isobel Hook, David Crampton, and Richard Murowinski. Integral field spectroscopy with the gemini multiobject spectrograph. i. design, construction, and testing. *Publications of the Astronomical Society of the Pacific*, 114(798):892–912, 2002.

[47] Simon Blake, Colin Dunlop, David Nandi, Ray Sharples, Gordon Talbot, Tom Shanks, Danny Donoghue, Nikolaos Galiatsatos, and Peter Luke. New microslice technology for hyperspectral imaging. *Remote Sensing*, 5(3):1204–1219, 2013.

[48] R. M. Sharples, R. Bender, M. D. Lehnert, S. K. Ramsay Howat, M. N. Bremer, R. L. Davies, R. Genzel, R. Hofmann, R. J. Ivison, R. Saglia, and N. A. Thatte. KMOS: an infrared multiple-object integral field spectrograph for the ESO VLT. In A. F. M. Moorwood and M. Iye, editors, *Ground-based Instrumentation for Astronomy*, volume 5492 of *Society of Photo-Optical Instrumentation Engineers (SPIE) Conference Series*, pages 1179–1186, September 2004.

[49] JE Larkin, AM Moore, EJ Barton, and Brian Bauman. The infrared imaging spectrograph (IRIS) for TMT: instrument overview. *Arxiv preprint arXiv:*, 2010.

[50] Anthony Horton, CG Tinney, Scott Case, Tony Farrell, Luke Gers, Damien Jones, Jon Lawrence, Stan Miziarski, Nick Staszak, David Orr, et al. Cyclops2: the fibre image slicer upgrade for the ucles high resolution

spectrograph. In *SPIE Astronomical Telescopes+ Instrumentation*, pages 84463A–84463A. International Society for Optics and Photonics, 2012.

[51] Gerardo Avila, Carlos Guirao, and Thomas Baader. High efficiency inexpensive 2-slices image slicers. In *SPIE Astronomical Telescopes+ Instrumentation*, pages 84469M–84469M. International Society for Optics and Photonics, 2012.

[52] G. J. Hill, P. J. MacQueen, C. Tejada, F. J. Cobos, P. Palunas, K. Gebhardt, and N. Drory. VIRUS: a massively replicated IFU spectrograph for HET. In A. F. M. Moorwood and M. Iye, editors, *Ground-based Instrumentation for Astronomy*, volume 5492 of *Society of Photo-Optical Instrumentation Engineers (SPIE) Conference Series*, pages 251–261, September 2004.

[53] Katsunari Okamoto. *Fundamentals of Optical Waveguides*. Elsevier, 30 Corporate Drive, Suite 400, Burlington, MA 01803, USA, 2006.

[54] Giovanni Barbarossa and Chellappan Narayanan. Optical device having modified transmission characteristics by localized thermal treatment, August 27 2002. US Patent 6,442,311.

[55] Dr. Schorsch. Arrayed waveguide grating, April 2006.

[56] G. O. Reynolds, J. B. Develis, G. B. Parrent, and B. J. Thompson. *The New Physical Optics Notebook: Tutorials in Fourier Optics*. SPIE, Bellingham, WA, 1989.

[57] Jeremy Allington-Smith and Joss Bland-Hawthorn. Astrophotonic spectroscopy: defining the potential advantage. *Monthly Notices of the Royal Astronomical Society*, 404(1):232 – 238, October 2010.

[58] P Muñoz, D Pastor, J Capmany, and a Martínez. Geometrical optimization of the transmission and dispersion properties of arrayed waveguide gratings using two stigmatic point mountings. *Optics express*, 11(19):2425–32, September 2003.

[59] J.W. Goodman. *Introduction to Fourier Optics*. MaGraw-Hill, 2nd edition, 1996.

[60] Jason Corbett and Jeremy Allington-Smith. Coupling starlight into single-mode photonic crystal fiber using a field lens. *Optics express*, 13(17):6527–6540, 2005.

[61] Peter. K. Cheo. *Fiber optics and Optoelectronics*. Prentice-Hall, Englewood Cliffs, New Jersey, 1990.

[62] A.W. Snyder and J.D. Love. *Optical Waveguide Theory*. Chapman and Hall, 1991.

[63] Jon Lawrence, Joss Bland-Hawthorn, Nick Cvetojevic, Roger Haynes, and Nemanja Jovanovic. Miniature astronomical spectrographs using arrayed-waveguide gratings: capabilities and limitations. *Library*, 7739:77394I–77394I–8, 2010.

[64] S G Leon-Saval, T A Birks, J Bland-Hawthorn, and M Englund. Multimode fiber devices with single-mode performance. *Optics letters*, 30(19):2545–7, October 2005.

[65] S. G. Leon-Saval, A. Argyros, and J. Bland-Hawthorn. Photonic lanterns: a study of light propagation in multimode to single-mode converters. *Optics Express*, 18:8430, April 2010.

[66] R.R. Thomson, G Brown, A.K. Kar, T.A. Birks, and J. Bland-Hawthorn. An integrated fan-out device for astrophotonics. In *Frontiers in Optics*, volume 2, pages 7–8. Optical Society of America, 2010.

[67] R R Thomson, T A Birks, S G Leon-Saval, A K Kar, and J Bland-Hawthorn. Ultrafast laser inscription of an integrated photonic lantern. *Optics express*, 19(6):5698–705, March 2011.

[68] F. G. Watson. Waveguide spectrographs for astronomy? In A. L. Ardeberg, editor, *Optical Telescopes of Today and Tomorrow*, volume 2871 of *Society of Photo-Optical Instrumentation Engineers (SPIE) Conference Series*, pages 1373–1378, March 1997.

[69] J. Lawrence, J. Bland-Hawthorn, N. Cvetojevic, R. Haynes, and N. Jovanovic. Miniature astronomical spectrographs using arrayed-waveguide gratings: capabilities and limitations. In *Society of Photo-Optical Instrumentation Engineers (SPIE) Conference Series*, volume 7739 of *Society of Photo-Optical Instrumentation Engineers (SPIE) Conference Series*, July 2010.

[70] N. Cvetojevic, N. Jovanovic, C. Betters, J. S. Lawrence, S. C. Ellis, G. Robertson, and J. Bland-Hawthorn. First starlight spectrum captured using an integrated photonic micro-spectrograph. *aap*, 544:L1, August 2012.

[71] Greg Smith. Mechanical design of the IRIS2 infrared imaging camera and spectrograph. *Proceedings of SPIE*, 4841(May 2011):1337–1344, 2003.

[72] J. Bland-Hawthorn, J. Lawrence, G. Robertson, S. Campbell, B. Pope, C. Betters, S. Leon-Saval, T. Birks, R. Haynes, N. Cvetojevic, and N. Jovanovic. PIMMS: photonic integrated multimode microspectrograph. In *Society of Photo-Optical Instrumentation Engineers (SPIE) Conference Series*, volume 7735 of *Society of Photo-Optical Instrumentation Engineers (SPIE) Conference Series*, July 2010.

[73] S. G. Leon-Saval, C. H. Betters, and J. Bland-Hawthorn. The Photonic TIGER: a multicore fiber-fed spectrograph. In *Society of Photo-Optical Instrumentation Engineers (SPIE) Conference Series*, volume 8450 of *Society of Photo-Optical Instrumentation Engineers (SPIE) Conference Series*, September 2012.

[74] T. A. Birks, B. J. Mangan, A. Díez, J. L. Cruz, and D. F. Murphy. "Photonic lantern" spectral filters in multi-core Fiber. *Optics Express*, 20:13996, June 2012.

[75] J Corbett and J Allington-Smith. Towards single mode integral field spectroscopy. *New Astronomy Reviews*, 50(4-5):313–315, June 2006.

[76] J. R. Allington-Smith. Strategies for spectroscopy on Extremely Large Telescopes - I. Image slicing. *Monthly Notices of the Royal Astronomical Society*, 376:1099–1108, April 2007.

[77] L Grave de Peralta, A A Bernussi, S Frisbie, R Gale, and H Temkin. Reflective Arrayed Waveguide Grating Multiplexer. *IEEE*, 15(10):1398–1400, 2003.

[78] L. Grave de Peralta, A. A. Bernussi, V. Gorbounov, J M. Berg, and H. Temkin. Control of center wavelength in reflective-arrayed waveguide-grating multiplexers. *IEEE Journal of Quantum Electronics*, 40(12):1725–1731, December 2004.

[79] K. Takada, M. Abe, T. Shibata, and K. Okamoto. 10-GHz-spaced 1010-channel tandem AWG filter consisting of one primary and ten secondary AWGs. *IEEE Photonics Technology Letters*, 13(6):577–578, June 2001.

[80] Jeremy. R. Allington-Smith. Private Communication.

[81] L. Simard, D. Crampton, B. Ellerbroek, and C. Boyer. The TMT instrumentation program. In *Society of Photo-Optical Instrumentation Engineers (SPIE) Conference Series*, volume 7735 of *Society of Photo-Optical Instrumentation Engineers (SPIE) Conference Series*, July 2010.

[82] H et al. Kaeufl. CRIRES: a High Resolution Infrared Spectrograph for ESO's VLT. *Observatory*, 2004.

[83] P McGregor, John Hart, and Peter Conroy. Gemini near-infrared integral field spectrograph(NIFS). *Proceedings of*, 4841:1581–1591, 2003.

[84] F. Eisenhauer, R. Abuter, K. Bickert, and et al. Biancat-Marchet. SINFONI - Integral field spectroscopy at 50 milli-arcsecond resolution with the ESO VLT. In M. Iye and A. F. M. Moorwood, editors, *Society of Photo-Optical Instrumentation Engineers (SPIE) Conference Series*, volume 4841 of *Society of Photo-Optical Instrumentation Engineers (SPIE) Conference Series*, pages 1548–1561, March 2003.

[85] Stephen Eikenberry, David Andersen, Rafael Guzman, John Bally, Salvador Cuevas, Murray Fletcher, Rusty Gardhouse, Don Gavel, Nicolas Gruel, Fred Hamann, Sam Hamner, Roger Julian, Jeff Julian, David Koo, Carlos Roman, Ata Sarajedini, Jonathan Tan, Kim Venn, Jean-pierre Veran, and John Ziegert. IRMOS : The near-InfraRed Multi-Object Spectrograph for the TMT. *Proc. of SPIE Vol 6269*, 6269(May 2012), 2006.

[86] S Lu, W H Wong, Y Yan, D Wang, D Yi, G Jin, Chee Avenue, and Hong Kong. Design of flat-field arrayed waveguide grating with three stigmatic points. *Optical and Quantum Electronics*, pages 783–790, 2003.

[87] Nibir K Dhar, Ravi Dat, and Ashok K Sood. Advances in infrared detector array technology. 2013.

[88] Christopher H Betters, Sergio G Leon-Saval, J Gordon Robertson, and Joss Bland-Hawthorn. Beating the classical limit: A diffraction-limited spectrograph for an arbitrary input beam. *Optics express*, 21(22):26103–26112, 2013.

[89] J. R. Allington-Smith, R. Content, C. M. Dubbeldam, D. J. Robertson, and W. Preuss. New techniques for integral field spectroscopy - I. Design, construction and testing of the GNIRS IFU. *MNRAS*, 371:380–394, September 2006.

[90] J Drew, J Bergeron, J Bouvier, et al. Report by the european telescope strategic review committee on europes 2-4m telescopes over the decade to 2020, 2010.

[91] D. Silva. ReSTAR Report: Table of Contents and Executive Summary. In *astro2010: The Astronomy and Astrophysics Decadal Survey*, volume 2010 of *Astronomy*, page 55P, 2009.

[92] R. Rebolo, M. R. Zapatero Osorio, and E. L. Martín. Discovery of a brown dwarf in the Pleiades star cluster. *Nature*, 377:129–131, September 1995.

[93] J. E. Gizis, I. N. Reid, and D. G. Monet. A 2MASS Survey for Brown Dwarfs toward the Hyades. *The Astrophysical Journal*, 118:997–1004, August 1999.

[94] M. Mayor, F. Pepe, D. Queloz, F. Bouchy, G. Rupprecht, G. Lo Curto, G. Avila, W. Benz, J.-L. Bertaux, X. Bonfils, T. Dall, H. Dekker, B. Delabre, W. Eckert, M. Fleury, A. Gilliotte, D. Gojak, J. C. Guzman, D. Kohler, J.-L. Lizon, A. Longinotti, C. Lovis, D. Megevand, L. Pasquini, J. Reyes, J.-P. Sivan, D. Sosnowska, R. Soto, S. Udry, A. van Kesteren, L. Weber, and U. Weilenmann. Setting New Standards with HARPS. *The Messenger*, 114:20–24, December 2003.

[95] M. Mayor and D. Queloz. A Jupiter-mass companion to a solar-type star. *Nature*, 378:355–359, November 1995.

[96] R. R. Thomson, R. J. Harris, T. A. Birks, G. Brown, J. Allington-Smith, and J. Bland-Hawthorn. Ultrafast laser inscription of a 121-waveguide fan-out for astrophotonics. *Optics Letters*, 37:2331, June 2012.

[97] B. A. Capron, M. W. Beranek, R. W. Huggins, and D. G. Koshinz. Design and performance of a multiple element slab waveguide spectrograph for multimode fiber-optic WDM systems. *Journal of Lightwave Technology*, 11:2009, 1993.

[98] TK Chan, Jason Karp, Rui Jiang, and Nikola Alic. 1092 channel 2-D array demultiplexer for ultralarge data bandwidth. *Journal of lightwave*, 25(3):719–725, 2007.

[99] Alex Ryer. *Light Measurement Handbook*. International Light, 1998.

[100] S. C. Ellis and J. Bland-Hawthorn. The case for OH suppression at near-infrared wavelengths. *Monthly Notices of the Royal Astronomical Society*, 386(1):47–64, May 2008.

[101] M. Cropper, M. Barlow, M. A. C. Perryman, K. Horne, R. Bingham, M. Page, P. Guttridge, A. Smith, A. Peacock, D. Walker, and P. Charles. A concept for a superconducting tunnelling junction based spectrograph. *MNRAS*, 344:33–44, September 2003.

[102] R. M. Myers, Z. Hubert, T. J. Morris, E. Gendron, N. A. Dipper, A. Kellerer, S. J. Goodsell, G. Rousset, E. Younger, M. Marteaud, A. G. Basden, F. Chemla, C. D. Guzman, T. Fusco, D. Geng, B. Le Roux, M. A. Harrison, A. J. Longmore, L. K. Young, F. Vidal, and A. H. Greenaway. CANARY: the on-sky NGS/LGS MOAO demonstrator for EAGLE. In *Society of Photo-Optical Instrumentation Engineers (SPIE) Conference Series*, volume 7015 of *Society of Photo-Optical Instrumentation Engineers (SPIE) Conference Series*, July 2008.

[103] RR Thomson, Timothy A Birks, SG Leon-Saval, AK Kar, and Joss Bland-Hawthorn. Ultrafast laser inscription of an integrated multimode-to-single-modes waveguide transition for astrophotonics. In *Lasers and Electro-Optics Europe (CLEO EUROPE/EQEC), 2011 Conference on and 12th European Quantum Electronics Conference*, pages 1–1. IEEE, 2011.

[104] Nemanja Jovanovic, Izabela Spaleniak, Simon Gross, Michael Ireland, Jon S Lawrence, Christopher Miese, Alexander Fuerbach, and Michael J Withford. Integrated photonic building blocks for next-generation astronomical instrumentation i: the multimode waveguide. *Optics Express*, 20(15):17029–17043, 2012.

[105] Izabela Spaleniak, Nemanja Jovanovic, Simon Gross, Michael J Ireland, Jon S Lawrence, and Michael J Withford. Integrated photonic building blocks for next-generation astronomical instrumentation ii: the multimode to single mode transition. *Optics express*, 21(22):27197–27208, 2013.

[106] E. Gendron, F. Vidal, M. Brangier, T. Morris, Z. Hubert, A. Basden, G. Rousset, R. Myers, F. Chemla, A. Longmore, T. Butterley, N. Dipper, C. Dunlop, D. Geng, D. Gratadour, D. Henry, P. Laporte, N. Looker, D. Perret, A. Sevin, G. Talbot, and E. Younger. MOAO first on-sky demonstration with CANARY. *Astronomy and Astrophysics*, 529:L2, May 2011.

[107] K Miura Davis, K Miura, Naoki Sugimoto, and Kazuyuki Hirao. Writing waveguides in glass with a femtosecond laser. *Optics letters*, 21(21):1729–1731, 1996.

[108] Rafael R Gattass and Eric Mazur. Femtosecond laser micromachining in transparent materials. *Nature photonics*, 2(4):219–225, 2008.

[109] Luís A Fernandes, Jason R Grenier, Peter R Herman, J Stewart Aitchison, and Paulo VS Marques. Femtosecond laser writing of waveguide retarders in fused silica for polarization control in optical circuits. *Optics express*, 19(19):18294–18301, 2011.

[110] Robert R. Thomson, Ajoy K. Kar, and Jeremy Allington-Smith. Ultrafast laser inscription: an enabling technology for astrophotonics. *Optics express*, August 2009.

[111] Y. Nasu, M. Kohtoku, and Y. Hibino. Low-loss waveguides written with a femtosecond laser for flexible interconnection in a planar light-wave circuit. *Optics Letters*, 30:723–725, April 2005.

[112] John E Greivenkamp. *Field guide to geometrical optics*, volume 1. 2004.

[113] S. Kirkpatrick, C. D. Gelatt, and M. P. Vecchi. Optimization by Simulated Annealing. *Science*, 220:671–680, May 1983.

[114] E. Høg, C. Fabricius, V. V. Makarov, S. Urban, T. Corbin, G. Wycoff, U. Bastian, P. Schwekendiek, and A. Wicenec. The Tycho-2 catalogue of the 2.5 million brightest stars. *Astronomy and Astrophysics*, 355:L27–L30, March 2000.

[115] N O'Mahony. Robodimm-the ing's new seeing monitor. *The Newsletter of the Isaac Newton Group of Telescopes*, 7:22–24, 2003.

[116] Chih-Hao Li, Andrew J Benedick, Peter Fendel, Alexander G Glenday, Franz X Kärtner, David F Phillips, Dimitar Sasselov, Andrew Szentgyorgyi, and Ronald L Walsworth. A laser frequency comb that enables radial velocity measurements with a precision of 1 cm s-1. *Nature*, 452(7187):610–612, 2008.

[117] Etienne Le Coarer, Sylvain Blaize, Pierre Benech, Ilan Stefanon, Alain Morand, Gilles Lérondel, Grégory Leblond, Pierre Kern, Jean Marc Fedeli, and Pascal Royer. Wavelength-scale stationary-wave integrated Fourier-transform spectrometry. *Optics Express*, 17(3):1976–1987, August 2007.

[118] Anthony Horton, Simon Ellis, Jon Lawrence, and Joss Bland-Hawthorn. Praxis: a low background nir spectrograph for fibre bragg grating oh suppression. In *SPIE Astronomical Telescopes+ Instrumentation*, pages 84501V–84501V. International Society for Optics and Photonics, 2012.

[119] N Blind, E Le Coarer, P Kern, and J Bland-Hawthorn. Astrophotonic micro-spectrographs in the era of elts. In *SPIE Astronomical Telescopes+ Instrumentation*, pages 914729–914729. International Society for Optics and Photonics, 2014.

[120] Nicolas K Fontaine, Roland Ryf, Joss Bland-Hawthorn, Sergio G Leon-Saval, et al. Geometric requirements for photonic lanterns in space division multiplexing. *Optics express*, 20(24):27123–27132, 2012.

Chapter 8

Appendicies

8.1 Spectral resolving power of the Thickened AWG with slit input

Start with the equation for central wavelength in AWG

$$\Delta L = \frac{\lambda m}{n} \tag{8.1}$$

Where ΔL is the path difference between adjacent orders, λ is the wavelength, m is the order and n is the refractive index. Setting ΔL to put λ_0 in the center (for the initial mode), the central wavelength in order m_0 change due to a different refractive index in a multimode AWG will be

$$
\begin{aligned}
\Delta\lambda_{mode} &= \lambda_1 - \lambda_0 \tag{8.2} \\
&= \frac{\Delta L_0 n_1}{m_0} - \frac{\Delta L_0 n_0}{m_0} \tag{8.3} \\
&= \frac{\Delta L_0}{m_0}\left(n_1 - n_0\right) \tag{8.4}
\end{aligned}
$$

The equation for diffraction limited spectrograph is $\Delta\lambda_{diff} = \lambda/(Nm)$. Combining this with the equation for resolution $R = \lambda/\Delta\lambda$ yields the degraded resolution of the instrument

$$R = \frac{\lambda}{\Delta\lambda_{mode} + \Delta\lambda_{diff}}. \tag{8.5}$$

take equation for $\Delta\lambda_{mode}$ and sub back in for ΔL yields

$$\Delta\lambda_{mode} \quad = \quad \frac{\Delta L}{m_0}(n_1 - n_0) \tag{8.6}$$

$$= \quad \frac{\lambda_0 m_0}{n_0 m_0}(n_1 - n_0) \tag{8.7}$$

$$= \quad \lambda_0\left(\frac{n_1}{n_0} - 1\right) \tag{8.8}$$

So R now becomes

$$R \quad = \quad \frac{\lambda_0}{\frac{\lambda_0}{mN} + \lambda_0\left(\frac{n_1}{n_0} - 1\right)} \tag{8.9}$$

$$= \quad \frac{1}{\frac{1}{mN} + \frac{n_1}{n_0} - 1} \tag{8.10}$$

so as m gets large the asymptotic R is

$$R_{asym} = \frac{1}{\frac{n_1}{n_0} - 1} = \frac{n_0}{n_1 - n_0} \tag{8.11}$$

Note, normally as as m tends to infinity R tends to infinity, but here the limit is the different effective indices of core modes.